EXTRACTION OF CHITIN NANOFIBERS AND UTILIZATION FOR SUSTAINABLE COMPOSITES AND FOAMS

A Thesis
Presented to
The Academic Faculty

by

Jie Wu

In Partial Fulfillment
of the Requirements for the Degree
Doctor of Philosophy in the
School of Materials Science and Engineering

Georgia Institute of Technology
August 2014

EXTRACTION OF CHITIN NANOFIBERS AND UTILIZATION FOR SUSTAINABLE COMPOSITES AND FOAMS

Approved by:

Dr. J. Carson Meredith, Advisor
School of Chemical and Biomolecular Engineering
Georgia Institute of Technology

Dr. Meisha Shofner
School of Materials Science and Engineering
Georgia Institute of Technology

Dr. Sven Behrens
School of Chemical and Biomolecular Engineering
Georgia Institute of Technology

Dr. Yonathan Thio
School of Chemical and Biomolecular Engineering
Georgia Institute of Technology

Dr. Yulin Deng
School of Chemical and Biomolecular Engineering
Georgia Institute of Technology

Date Approved: June 3, 2014

To *my beloved family for their unconditional love and support*

ACKNOWLEDGEMENTS

My Ph.D. thesis would not be accomplished without the advice, support, help, love and care from many individuals.

First and foremost, I would like to sincerely thank my advisor and mentor, Dr. Carson Meredith, for all his guidance, constant encouragement, support, patience and inspiration throughout my journey as a graduate student at Georgia Tech. I deeply appreciate him for creating such a great atmosphere of freedom in our group and encouraging me to initiate and implement my own ideas. Even though sometimes my scientific ideas were not rational and practical, he can always find a way to encourage me. This training greatly improved my independent research ability and problem-solving ability, which will be very beneficial for my future career development. He set a great example for me to become a person who has great personality, strong integrity and high work ethic. What I learned from him will benefit the rest of my life.

I am very thankful to my committee members, Dr. Sven Behrens, Dr. Yulin Deng, Dr. Meisha Shofner, and Dr. Yonathan Thio for providing me with their insightful advices and comments throughout my graduate study, and generously allowing me to use the equipment from their groups. I would like to acknowledge the organizations that provided financial support for my research: Institute of Paper Science and Technology at Georgia Tech, U.S. Air Force Office for Scientific Research, and the New Page Company.

I am much indebted to the former and current members of the Dr. Meredith's research group, Dr. Jung-Hyun Lee, Dr. Ismael Gomez, Dr. Sangil Han, Dr. Shanhong

Xu, Kaitlin Cook, Katelyn Roberts, Dr. Haisheng Lin, Timi Fadiran, Natalie Girouard, Yi Zhang, Donglee Shin and Zihao Qu, and Nur Ashikin Lockman for their help, discussion or great friendship.

I want to give my sincere thanks to my friends, not already mentioned, during my time at Georgia Tech who have provided their generous help on my research and study: Dr. Kuang Zhang, Dr. Yaodong Liu, Dr. Justin Vaughn, Dr. Hongzhi Wang, Dr. Kyung Hee Oh, Dr. Ziyin Lin, Dr. Ji Hoon Lee, Dr. Chen Zhang, Ben Deglee, An-ting Chien, Xin Dong, Tom Wyatt, Wentian Gu, Yifeng Hong, Xudong Fang, Fuyue (Stephanie) Li, and Prateek Verma.

I would like to express my gratitude to Dr. Meifang Zhu and Dr. Yonggen Lv for providing me with the opportunities to perform scientific research and solve challenging academic problems as an undergraduate student. The research intrigued my interest in pursuing a Ph.D. degree and helped me build a strong foundation for my Ph.D. study.

Last but not least, I would like to thank my family, my parents and sister for their long-standing unconditional love, support and encouragement throughout my life. I am very grateful for the support, love, care and sacrifice of my wife, Judy Zhu. I would never have come this far without her. I greatly thank my son, Bryson, for the joyful and memorable moments he gave to me since he was born.

TABLE OF CONTENTS

ACKNOWLEDGEMENTS IV

LIST OF TABLES X

LIST OF FIGURES XI

LIST OF SYMBOLS AND ABBREVIATIONS XVI

SUMMARY XVII

Chapter 1 Introduction and Background 1

1.1 Renewable Materials 1

1.2 Structure and Properties of Chitin 2

1.3 Fabrication of Nanofibrous Materials 5

1.4 Polymer Nanocomposites 8

1.5 Particle-stabilized Foams 9

1.6 Thesis Overview 14

1.7 References 15

Chapter 2 Isolation of Chitin Nanofibers from Crab Shells and Characterization of Their Properties 23

2.1 Overview 23

2.2 Introduction 24

2.3 Experimental Methods 25

2.3.1 Materials 25

2.3.2 Extraction of CNF from Crab Shells 26

2.3.3 Materials Characterization 26

2.4 Results and Discussion 31

2.4.1 Chitin Purification and Fibrillation from Crab Shells 31

2.4.2 Crystal Structure of Chitin Powders and CNF Film 39

2.4.3 Dynamic Rheology of CNF Dispersion 40
2.4.4 Thermal Properties of Chitin Powders and CNF Film 42
2.4.5 Barrier Properties of CNF Film 45
2.5 Conclusions 46
2.6 References 47
Chapter 3 Assembly of Chitin Nanofibers into Porous Nanofibrous Structures 51
3.1 Overview 51
3.2 Introduction 52
3.3 Experimental Methods 56
3.3.1 Materials 56
3.3.2 Chitin Purification and Fibrillation 56
3.3.3 Formation of Porous Chitin Materials 57
3.3.4 Materials Characterization 57
3.4 Results and Discussion 57
3.4.1 The Morphology of Room-temperature Dried CNF 57
3.4.2 The Morphologies of Freeze-dried Chitin Using Aluminum Substrate 59
3.4.3 Porous Structure Formation Mechanism of Freeze-dried Materials 63
3.4.4 The Morphologies of Freeze-dried Chitin Using Steel Substrate 66
3.5 Conclusions 67
3.6 References 68
Chapter 4 Chitin Nanofibers Reinforced Polymer Composites 73
4.1 Overview 73
4.2 Introduction 73
4.3 Experimental Methods 75
4.3.1 Materials 75

4.3.2 Chitin Purification and Fibrillation 75

4.3.3 Preparation of CNF/PEO Nanocomposite Films 76

4.3.4 Fabrication of CNF/PS Composites and Polymer Film Preparation 76

4.3.5 Materials Characterization 77

4.4 Results and Discussion 80

4.4.1 CNF Dispersion in PEO Matrix 80

4.4.2 Investigation of CNF Interaction with PEO Matrix Using ATR 84

4.4.3 Investigation of CNF Interaction with PEO Matrix Using an AFM Colloidal Probe Method 85

4.4.4 Thermal Properties of CNF/PEO Nanocomposites 91

4.4.5 Mechanical Properties of CNF/PEO Nanocomposites 93

4.5 Conclusions 94

4.6 References 95

Chapter 5 Engineering Patricle Stablized Aqueous Foams from Rewnewable Resources 99

5.1 Overview 99

5.2 Introduction 100

5.3 Experimental Method 101

5.3.1 Materials 101

5.3.2 Chitin Purification and Fibrillation 102

5.3.3 Aqueous Foam Preparation and Characterization 102

5.3.4 Quartz Crystal Microbalance (QCM) Measurement 104

5.4 Results and Discussion 105

5.4.1 Foaming Ability of CNF Dispersion 105

5.4.2 Foaming Ability and Foam Stability of CNF/Valeric Acid Dispersion 107

5.4.3 Investigation of the Role of Valeric Acid in CNF Dispersion 115

5.4.4 Foaming Ability of CNF Dispersion with Addition of Other Carboxylic Acids 117

5.5 Conclusions 119

5.6 References 120

Chapter 6 Conclusions and Recommendations 125

6.1 Summary and Conclusions 125

6.1.1 Produce the CNFs without forming strong network structures from crab α-chitin using a physical-mechanical method 125

6.1.2 Develop a route to create porous nanofibrous materials utilizing CNFs 125

6.1.3 Investigate the reinforcing effect of CNFs in polymer matrices 126

6.1.4 Study the interfacial properties of CNFs and create particle-stabilized aqueous foams from renewable high-aspect-ratio CNFs 127

6.2 Recommendations for Future Work 127

6.2.1 Investigate the thermal degradation mechanism of chitin-based materials 127

6.2.2 Verify the proposed porous structure formation mechanism 128

6.2.3 Investigate the reinforcing effect of CNFs in other polymer matrices 129

6.3 References 129

LIST OF TABLES

Table 1.1 Proposed crystallographic parameters of α and β chitins [10, 15, 16]..... 3

Table 1.2 Density and mechanical properties of reinforcing agents [9, 28]. 8

Table 2.1 Adsorption bands of the purified chitin and CNF film, and their corresponding assignments [23]. 37

Table 2.2 Thermal properties of the purified chitin and CNF film..... 43

Table 2.3 Gas permeability of CNF film. 46

Table 3.1 Porosity of freeze-dried chitin. 59

Table 4.1 Surface roughness of the various polymer surfaces..... 86

Table 4.2 Contact angles (˚) of polymer surfaces with three testing liquids. 86

Table 4.3 Surface tension components (mJ/m^2) of various polymer surfaces. 86

Table 4.4 Melting temperature and crystallinities of neat PEO and PEO/CNF composite films. 91

Table 5.1 Surface tensions of valeric acid, CNF and CNF/valeric acid aqueous dispersions..... 116

Table 5.2 Chemical structures and pKa values of carboxylic acids [35]..... 117

LIST OF FIGURES

Figure 1.1 Processes of petroleum and biomass to chemicals and liquid fuels [1]. 1

Figure 1.2 Chemical structures of chitin and chitosan [10-12]..... 2

Figure 1.3 Proposed molecular structure and inter and/or intra hydrogen bonding in (A) α-chitin, and (B) β-chitin [11, 12]..... 3

Figure 1.4 Hierarchical structure of the exoskeleton material of H. americanus (American lobster) (I) Chitin molecule; (II) Anti-parallel packing of α-chitin; (III) Chitin-protein nanofibrils; (IV) Chitin-protein nanofibers; (V) Mineralized chitin-protein planes; (VI) Twisted plywood structure, and (VII) Multilayer cuticle of lobster [17, 18]. 4

Figure 1.5 (A) Schematic of self-assembly of peptide-amphiphiles molecules into a cylindrical micelle [43]; (B) An electrospinning experimental setup [49]. 6

Figure 1.6 (A) For particle-oil-water mixtures, “Pickering emulsion” drops of oil-in-water or water-in-oil are stabilized by hydrophilic or hydrophobic particles respectively. For particle-air-water mixtures, “Pickering foams” air-in-water or “Liquid marbles” water-in-air are stabilized by hydrophilic or hydrophobic particles, respectively [72]; (B) The colloidal particle is absorbed at the air-water interface and its contact angle θ is determined by the balance of three interfacial tensions [87]; (C) Attachment energy of colloidal particles at an air-water interface as a function of the contact angle for different sized particles [87]; (D) The appearance of aqueous foams stabilized by (D1) sodium dodecylsulfate (SDS) and (D2) SU-8 microrods with diameters of less than 1 μm and lengths of a few tens μm. (D1) and (D2) were taken 10-15 mins after the foams were formed. (D4) and (D5) showed the appearance of (D1) and (D2) after their 2 days of storage, respectively. (D3) Optical micrograph of the SU-8 microrods (scale bar: 50 μm) and (D6) Microrod-stabilized air bubble (scale bar: 50 μm) [90]. 11

Figure 2.1 Schematic of a constant volume permeation system [22]. 29

Figure 2.2 Schematic of a permeation cell for gas permeability measurement of CNF film [22]..... 29

Figure 2.3 ^{13}C CP-MAS solid state NMR of purified chitin from crab shells..... 31

Figure 2.4 (A) Appearance of cationized chitin dispersion (purified chitin was dispersed under acid conditions for -NH_2 group cationization); (B) and (C) are the digital photos of the homogenized chitin in water with pH ~ 4.1, which was produced by a high pressure homogenization process of the cationized chitin/water; (D) Light transmittance spectra of the cationized chitin/water and homogenized chitin/water in the range of 400 to 800 nm wavelengths..... 32

Figure 2.5 (A), (C) and (E) are the SEM images of the purified chitin, cationized chitin and homogenized chitin, respectively; (B), (D) and (F) are enlarged SEM images of above three chitin-based materials, respectively. 33

Figure 2.6 (A) Appearance of optically transparent CNF film; (B) AFM image of CNF film obtained from the tapping mode in air at room temperature; (C) Light transmittance spectra of CNF film in the range of 400 to 800 nm wavelengths. 36

Figure 2.7 ATR spectra of purified chitin powder and CNF film. 37

Figure 2.8 (A) 2-D XRD pattern of purified chitin powder; (B) Integrated 1-D XRD curves of purified chitin powder and CNF film. 39

Figure 2.9 Shear viscosity as a function of shear rate for CNF dispersion with pH of ~ 4.1 40

Figure 2.10 The storage modulus (G') and loss modulus (G'') as a function of frequency for CNF dispersion with pH of ~ 4.1. 40

Figure 2.11 TGA curves of purified chitin powder and CNF film. 42

Figure 2.12 DTGA curves of purified chitin powder and CNF film. 42

Figure 2.13 SEM images of pyrolyzed chitin powder and CNF film. These chitin materials were heated up to 600 ˚C under nitrogen atmosphere. The heating protocol is as follows: 1. heated from room temperature to 120 ˚C at a ramp rate of 10 ˚C/min; 2. held at 120 ˚C for 30 min; 3. heated from 120 ˚C to 600 ˚C at a ramp rate of 10 ˚C /min; 4. Cooled down to room temperature. 44

Figure 2.14 XRD patterns of 600 ˚C pyrolyzed chitin powder and CNF film. 45

Figure 3.1 (A) Cyphochilus "White beetle"; (B) SEM image of white scales covering of Cyphochilus head, legs and body; (C) SEM image of interiors of white beetle covering [15]. 52

Figure 3.2 (A) Particles, molecules or mixture of them dispersed or dissolved in water (left); Ice crystals grew towards freezing direction and pushed the particles or molecules into the interstitials between them (right) [31]; (B) Crystal structure of ice and the anisotropy of crystal growth kinetics [35]. 54

Figure 3.3 The morphologies of freeze-dried materials (A) Honeycomb; (B) Aligned sheet; (C) Double network; (D) and (E): Brick and mortar; (F) Fibrous structures [31-36]. 55

Figure 3.4 (A) SEM image of CNF fabricated via fibrillation of purified chitin by high pressure homogenization; (B) SEM image and (C) Photo of CNF film produced by drying CNF/water dispersion at room temperature. 58

Figure 3.5 (A) Photo; (B) Top; (C) Bottom; (D) Cross section; (E) Enlarged top SEM images of freeze-dried chitin produced under -20 ˚C freezing (aluminum dish). 60

Figure 3.6 SEM images of freeze-dried chitin: (A) Top and B) Cross section of sample produced at -80 ˚C freezing; (C) Top and (D) Cross section of sample produced under liquid nitrogen freezing. 61

Figure 3.7 Schematic of particle-advancing ice front interactions. A liquid film with a thickness of d separates a particle with a radius of r from the advancing ice fronts [44]. 62

Figure 3.8 Schematic representation of assembly of CNFs under -20 ˚C freezing using aluminum dish: (A) CNF/water dispersion; (B) CNF/water dispersion with advent of ice nuclei; (C) CNF bundles encapsulated in ice. 64

Figure 3.9 SEM images of chitin freeze-dried using indented stainless-steel mold: (A) Bottom; (B) Cross section in touch with stainless steel wall of freeze-dried chitin under -20 ˚C freezing (stainless-steel mold). 66

Figure 4.1 Schematic of adhesion measurements using an AFM colloidal probe method. 78

Figure 4.2 (A) and (C) are the fractured cross section and top SEM images of 10% CNF/PEO composites, respectively; (B) and (D) are the fractured cross section and top SEM images of 20% CNF/PEO composites, respectively; (E) and (F) are the top SEM images of dried solvent-washed 10% and 20% CNF/PEO composites, respectively..... 81

Figure 4.3 (A), (C) and (E) are the digital photos of neat PEO, 5% CNF/PEO and 20% CNF/PEO films that were immersed in water, respectively. The photos were taken ~30 s after placing these films in water; (B) is the digital photo of neat PEO film after ~3 hours of water immersion; (D) and (F) are the digital photos of 5% CNF/PEO and 20% CNF/PEO films that were immersed in ethanol, respectively. The films were firstly immersed in water for 10 days and then immersed in ethanol for 3 days. 82

Figure 4.4 ATR spectra of neat PEO, CNF and PEO/CNF composite films..... 84

Figure 4.5 Enlarged ATR spectra of neat PEO, CNF and PEO/CNF composite films. ... 84

Figure 4.6 (A) SEM image of CNF-coated PS particles; (B) Enlarged SEM image of CNF-coated PS particle..... 85

Figure 4.7 (A) Force-distance curves for CNF-coated PS particle on various polymer surfaces; (B) Total adhesion forces for CNF-coated or bare PS particle on various polymer surfaces. PS@Chitin represents the CNF-coated PS particle. 88

Figure 4.8 Fitting of a planar model of equation 4.4 to adhesion force data. 89

Figure 4.9 DSC curve of neat PEO film. 91

Figure 4.10 (A) Elastic modulus; (B) Tensile strength of neat PEO and PEO/CNF composite films. 93

Figure 5.1 SEM images of (A) fibrillated CNFs from the purified chitin and (B) CNF dense film. 105

Figure 5.2 (A) and (C) photos represent 1% CNF at pH 4.1 before and after frothing by a rotor-stator homogenizer, respectively; (B) and (D) photos represent 1% CNF at pH 5.8 before and after frothing respectively. (C) and (D) photos were immediately taken after frothing. 106

Figure 5.3 Schematic of the formation of CNF stabilized foams. 107

Figure 5.4 (A), (B) and (C) are digital photos of the 50 mmol/l valeric acid in water before, during and after frothing by a rotor-stator homogenizer, respectively; (D), (E) and (F) are digital photos of the frothed 1 mmol/l, 5 mmol/l and 25 mmol/l valeric acid in 0.1% CNF/water dispersion, respectively (photos were taken 2 mins after frothing); (G) and (H) photos represent 30 mins and 24 hours after the aeration of 5 mmol/l valeric acid/0.1% CNF/water dispersion, respectively; (I) photo was taken 24 hours after the aeration of 25 mmol/l valeric acid/0.1% CNF/water dispersion. 108

Figure 5.5 Optical microscope image of 5 mmol/l valeric acid/0.1% CNF in water dispersion. 109

Figure 5.6 SEM images of 0.1% CNF/5 mmol/l valeric acid foams. (A) Top of the bubble cluster; (B) Top of the single dispersed bubble; (C) and (D) are enlarged top SEM images of the bubble edge and bubble center respectively. 110

Figure 5.7 (A), (B) and (C) are digital photos of the frothed 1 mmol/l, 5 mmol/l and 25 mmol/l valeric acid in 1% CNF/water dispersion, respectively (photos were taken 2 mins after frothing); (D), (E) and (F) photos represent 1, 3 and 24 hours after the aeration of 5 mmol/l valeric acid/1% CNF/water dispersion, respectively. 111

Figure 5.8 Optical microscope image of 5mmol/l valeric acid/1% CNF in water dispersion. 112

Figure 5.9 SEM images of 1% CNF/5 mmol/l valeric acid foams. (A) Top of bubble cluster; (B) Top of single dispersed bubble; (C) Cross section of bubble cluster; (D), (E) and (F) are the enlarged top SEM images of intersections of three bubbles, bubble edge and bubble center, respectively. 113

Figure 5.10 (A) and (B) represent the 1% CNF/water dispersion with top-down and upside-down placement, respectively. 114

Figure 5.11 Representative curves of fifth overtone QCM shifts in frequency (Hz) as a function of time for valeric acid adsorption on the CNF surface. 115

Figure 5.12 (A), (B) and (C) represent the frothed 1% CNF dispersions with addition of propionic acids (25 mmol/l), enanthic acids (0.5 mmol/l) and caprylic acids (0.5 mmol/l), respectively. 118

LIST OF SYMBOLS AND ABBREVIATIONS

AFM	Atomic Force Microscopy
ATR	Attenuated Total Reflectance
CNF	Chitin Nanofibers
CP/MAS	Cross Polarization/Magnetic Angle Spinning
CTAB	Cetyltrimethylammonium Bromide
DA	Degree of Acetylation
DMA	Dynamic Mechanical Analysis
DSC	Differential Scanning Calorimetry
HTMECH	High-throughput Mechanical Characterization
NMR	Nuclear Magnetic Resonance
PE	Poly(ethylene)
PEO	Poly(ethylene oxide)
PS	Polystyrene
PTFE	Poly(tetrafluroethylene)
PVA	Poly(vinyl alcohol)
PVAc	Poly(vinyl acetate)
PVDF	Poly(vinylidene fluoride)
SEM	Scanning Electron Microscopy
SDS	Sodium Dodecylsulfate
TGA	Thermogravimetic Analysis
Tg	Glass Transition Temperature
Tm	Melting Temperature
UV-Vis	Ultraviolet-Visible Lights
XRD	X-ray Diffraction

SUMMARY

Developing renewable materials to reduce the dependence on fossil fuel as a feedstock for a wide range of applications is becoming increasingly acknowledged as important in society. Chitin, the second most abundant biopolymer in nature, is an ideal candidate for diverse applications because of its remarkable properties, such as abundance, renewability, biodegradability, biocompatibility, antibacterial activity, chemical functionality, and high stiffness and strength. Despite these inherent advantages, chitin is currently still underutilized mainly due to its strong molecular interactions, which make it insoluble in common solvents. Currently, its major applications are limited to biomedical engineering, such as tissue engineering, wound dressing and sutures.

This thesis aims to explore and enable the potential utilization of chitin in other fields where it may serve as a renewable functional advanced material. Here, a number of novel chitin-based materials were developed successfully without employing chitin dissolution. These include chitin nanofibers (CNFs), porous chitin with tunable structures, chitin-reinforced polymer composites and chitin-stabilized aqueous foams. Moreover, the properties of these materials including interfacial, optical, thermal, and mechanical characteristics were determined, and their potential utilizations were demonstrated.

Briefly, in chapter 2, CNFs with diameters of ~20 nm were successfully extracted from crab α-chitin by a high pressure homogenization process. The produced CNFs were dispersed well in water without forming strong network structures due to their electrostatic repulsions. The obtained CNF film has a high residue amount (40%) when heated up to 1000 ˚C. Meanwhile, it exhibited high optical transparency as well as great

gas barrier properties. In chapter 3, on the basis of the obtained CNFs in chapter 2, versatile porous structures including oriented sheets and three-dimensional aperiodic nanofiber networks were achieved by using a freeze drying technique. Since the formation of nanofibrous structures cannot be predicted by the widely-used particle encapsulation model, a modified structure formation mechanism was proposed. In chapter 4, the structure-property relationships of the CNF/poly(ethylene oxide)(PEO) nanocomposites were established. We demonstrated that the CNFs formed network structures in PEO matrix and had hydrogen bonding interaction with PEO. The CNFs can greatly enhance the mechanical properties of PEO, such as elastic modulus and tensile strength. In chapter 5, the aqueous foams stabilized by high-aspect-ratio CNFs were developed. The created foams exhibited strong hindrance on film drainage, coalescence and disproportionation. The fibrillated CNFs alone were not able to stabilize air bubbles, but the addition of small amounts of valeric acids in CNF dispersion can make chitin foamable. The results clearly showed that valeric acid modified CNFs reduced the surface tension of aqueous dispersion and were attached at the air-water interface.

Overall, this research has provided many new insights for the fabrication, characterization, and utilization of chitin, and has built a solid foundation for further exploiting chitin for diverse applications.

CHAPTER 1

INTRODUCTION AND BACKGROUND

1.1 Renewable Materials

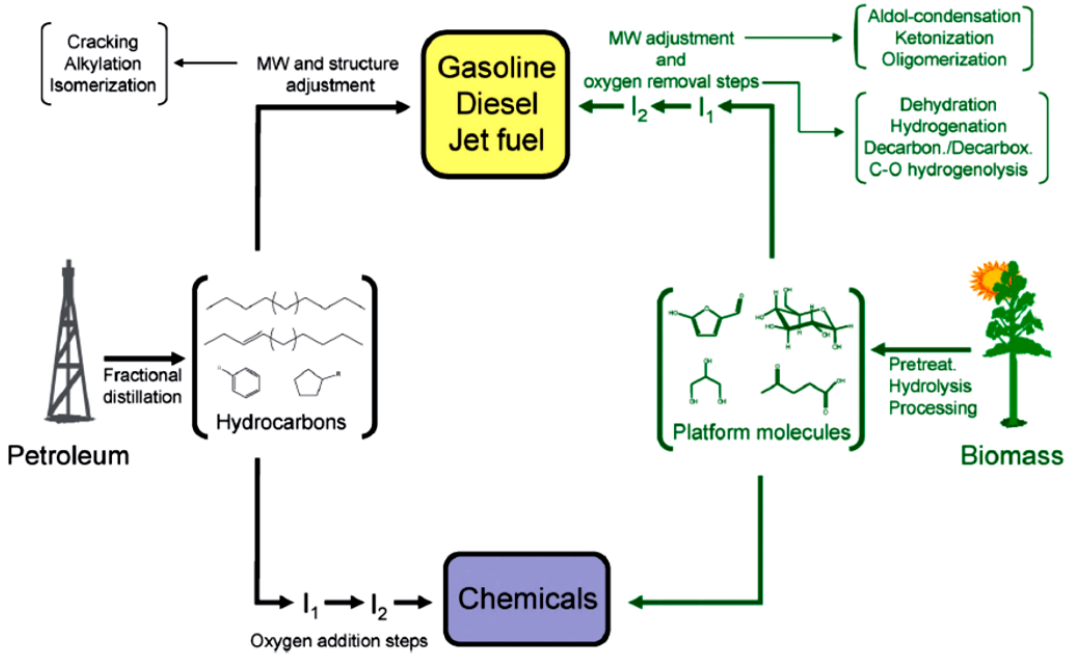

Figure 1.1 Processes of petroleum and biomass to chemicals and liquid fuels [1].

Over the past two decades, tremendous efforts from both academic and industrial societies have been devoted to developing advanced materials from renewable resources in order to replace conventional fossil fuel-based products. Various bio-based resources, including sugarcanes, soybeans, algae and trees have been studied and significant progress has been achieved in the production of sustainable alternatives to many synthetic materials, such as biochemicals, bioplastics and biofuels (Figure 1.1) [1-3]. In addition to focusing on replacing the existing non-renewable materials, producing sustainably-sourced materials with novel superior properties have become of importance and drawn extensive attention from researchers [3-9]. Sustainability is guiding the development of

next generation materials due to fossil reserve depletion and environmental issues (global warming and pollution etc.) [1-5, 9].

1.2 Structure and Properties of Chitin

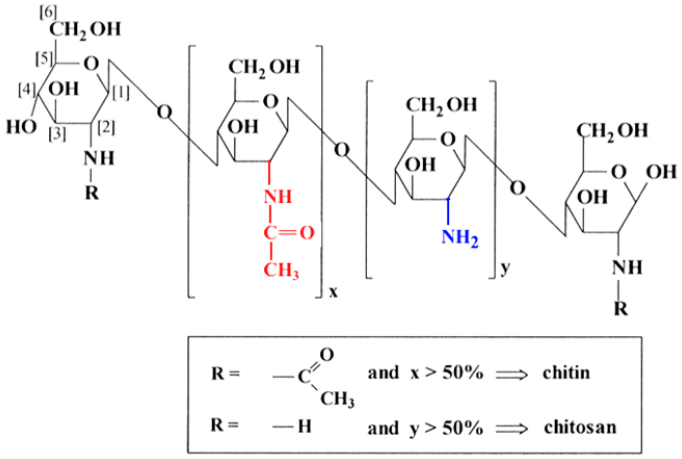

Figure 1.2 Chemical structures of chitin and chitosan [10-12].

Chitin, poly (β-(1→4)-N-acetyl-D-glucosamine), has amino, amide and hydroxyl functional groups in its polymer chain as seen in Figure 1.2, and is the second most abundant naturally occurring polymer right after cellulose. It is synthesized by a mass of living organisms, such as arthropods, fungi, and yeast with an annual production of 10^{10} to 10^{11} tons in the world [10-13]. Chitin has three polymorphic forms: α, β and γ, depending on its source. α-Chitin is the most abundant form, existing in crab, shrimp shells, fungal and yeast walls, and has a highly ordered crystalline structure with an anti-parallel configuration (Figure 1.3 A and Table 1.1). In contrast, β-chitin is present in squid pen, tubeworm and diatom spines, and has a parallel packing and different crystallographic parameters from α-chitin (Figure 1.3 B and Table 1.1). Both of α and β chitin have strong hydrogen bonding. γ-Chitin is a mixture of α and β forms. Chitin combines with chitosan to occur as a copolymer in nature, and the name of chitin and

chitosan depends on the degree of acetylation (DA), as shown in Figure 1.2. DA, i.e. the ratio of 2-acetamido-2-deoxy-D-glucopyranose to -2-amino-2-deoxy-D-glucopyranose units has a significant impact on the properties of the resultant chitin, such as solubility, solution properties and bioactivity. For example, chitosan is soluble in dilute acidic solution but chitin is insoluble to all common solvents and aqueous acids [10-14].

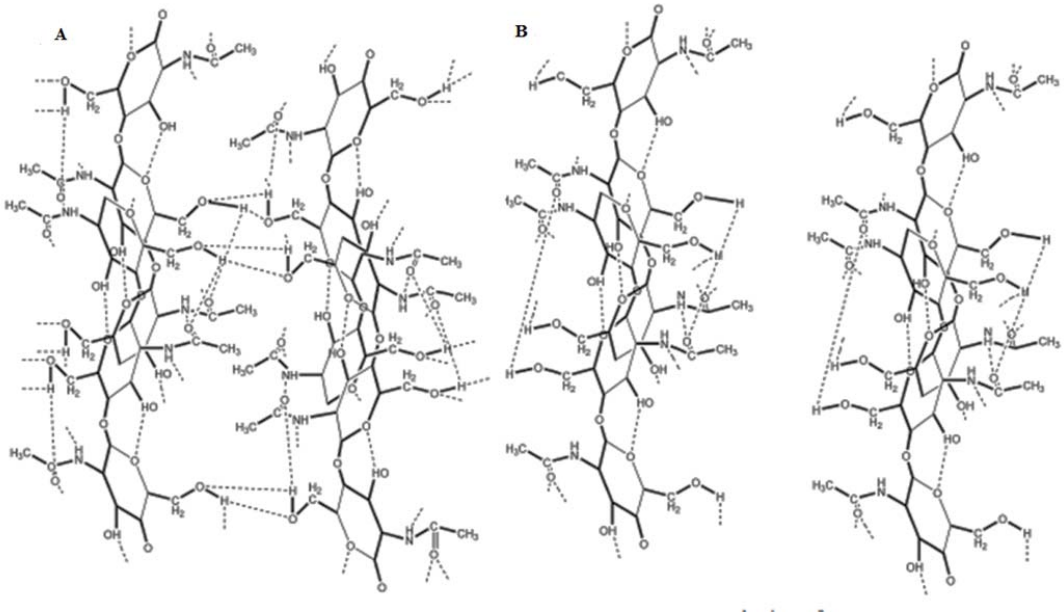

Figure 1.3 Proposed molecular structure and inter and/or intra hydrogen bonding in (A) α-chitin, and (B) β-chitin [11, 12].

Table 1.1 Proposed crystallographic parameters of α and β chitins [10, 15, 16].

Material	a (nm)	b (nm)	c (nm)	γ (^{o})	Space group
α-chitin	0.474	1.886	1.032	90	$P2_12_12_1$
β-chitin	0.485	0.926	1.038	97.5	$P2_1$

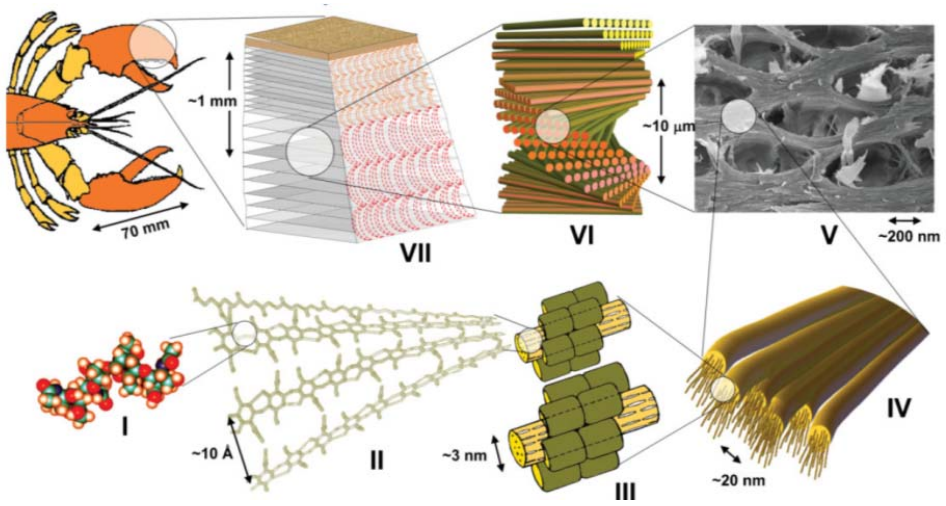

Figure 1.4 Hierarchical structure of the exoskeleton material of H. americanus (American lobster) (I) Chitin molecule; (II) Anti-parallel packing of α-chitin; (III) Chitin-protein nanofibrils; (IV) Chitin-protein nanofibers; (V) Mineralized chitin-protein planes; (VI) Twisted plywood structure, and (VII) Multilayer cuticle of lobster [17, 18].

Chitin is an important structural component of many intricately hierarchical structures in natural creatures [17-19]. An example is the complex structure in arthropods constructed primarily by chitin. The crustacean exoskeleton mainly consists of chitin, protein and minerals. This biocomposite material has a strict hierarchical organization composed of a variety of structural levels as shown in Figure 1.4. At the molecular level is the chitin itself. Around 20 of chitin molecules are arranged in an anti-parallel configuration to form long crystalline α-chitin nanofibrils with diameters of 2 to 5 nm. These nanofibrils are wrapped with proteins and are further gathered with other nanofibrils to form large fibers of about 50-300 nm diameter. The next hierarchy level is the formation of a planar woven and branched network created from the chitin-protein fibers, which are embedded in a variety of proteins and minerals. Subsequently, these woven and network planes form a twisted ‘plywood’ structure via their helicoid stack and

this microstructure becomes an element of the exoskeleton [17, 18]. Purified chitin can be produced from crustaceans and many other organisms by a series of chemical treatments, such as acid treatment to remove minerals and base process to deplete proteins [10, 11, 20, 21].

Due to its strong molecular interactions and insolubility in common solvents, the production and application of chitin-based materials have been restricted for a long time. However, in terms of the extraordinary properties of chitin, such as renewability, biodegradability, biocompatibility, antibacterial activity and high stiffness, many researchers have been highly motivated to overcome the processing difficulties of chitin and have made much progress on its utilization over the last few decades [10, 11]. For example, few solvents were found to be able to dissolve chitin, such as dimethylacetamide (DMAc)/LiCl, hexafluoro-2-propanol (HFIP), and NaOH/urea [10, 11, 22, 23]. Since it can be dissolved, different types of chitin was subsequently produced, such as films, fibers, gels, and porous scaffolds, and the resulting chitin-based materials have been used for many areas, including tissue engineering, wound dressing, and absorbents [10-12, 14, 22-27]. In addition to the dissolution route to utilize chitin, it can also be employed by downsizing it into nanosized materials (rigid nanocrystals) using acid hydrolysis. These nanocrystals have been widely applied to polymer composite field owing to their excellent mechanical properties [28-35].

1.3 Fabrication of Nanofibrous Materials

Recently, owing to their excellent properties, such as unique dimensional (high surface to volume ratio), optical, mechanical, electrical and other characteristics, nanofibrous materials have attracted much attention as an important component of

various advanced materials for a wide range of applications, such as biomedical engineering, electronic devices, sensors, and structural materials [3-8, 36-42]. Currently, nanofibrous materials can be produced by a number of techniques, including self-assembly, phase separation, and electrospinning, which are briefly introduced below [43-54].

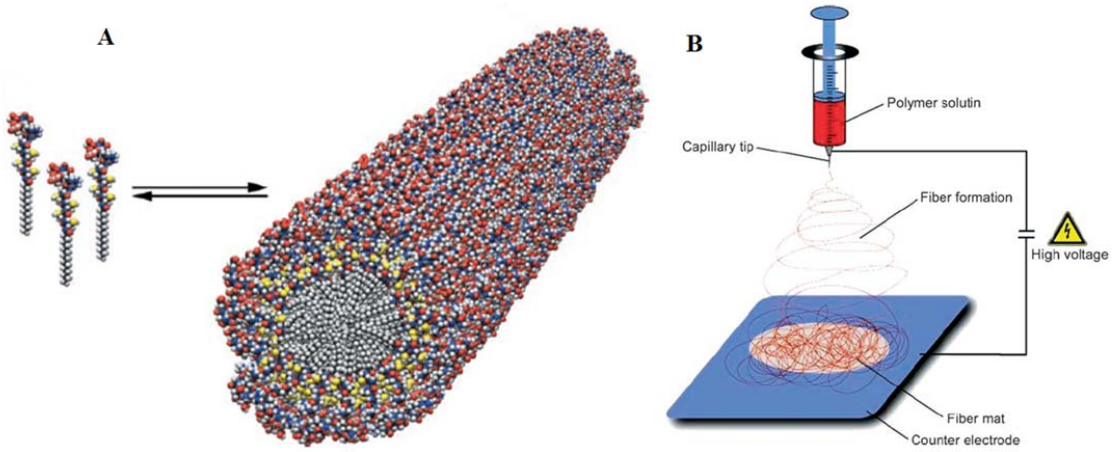

Figure 1.5 (A) Schematic of self-assembly of peptide-amphiphiles molecules into a cylindrical micelle [43]; (B) An electrospinning experimental setup [49].

Self-assembly refers to the build-up of molecular or nanoscale units into larger structures and materials via the synergistic interactions of the individual building blocks. A variety of self-assemble methods have been reported to be able to generate nanofibrous materials so far [43-47]. For example, Hartgerink et al. showed that nanofibers were successfully created from self-assembly of peptide-amphiphiles, which have precisely tailored chemical structures: a long alkyl tail for conferring hydrophobicity and a linker region of three glycine residues for providing flexible conformation (Figure 1.5 A), and a stable cross-linked fibrous network structure was formed by tuning medium pH [43]. Tsukruk et al. reported the assembly of supramolecular nanofibers using the amphiphilic dendritic molecules with hydrophilic inner core-hydrophobic shell architecture. The

multiple intermolecular interactions between flexible cores stabilized these nanofibers and made them robust and flexible [47].

Phase separation is a thermodynamic separation of a polymer solution into a polymer-rich domain and a polymer-poor/solvent rich domain, which can be induced by thermally treatment or the addition of non-solvents to the polymer solution [49, 50, 52]. Many different sourced nanofibrous materials have been generated by this technique. For example, Zhang et al. formed nanofibrous porous materials using thermally induced spinodal liquid-liquid phase separation process, which mainly consisted of five steps: polymer dissolution, phase separation and gelation, solvent extraction, freezing and freeze drying. The produced fibrous network had fiber diameters of 50 to 500 nm and a porosity of over 98% [48-50]. Zhong et al. produced ultrafine nanofibers (10 nm in diameter) from the precipitation of chitin /LiCl/N,-N-dimethylacetamide solution upon addition of water [51].

Compared with self-assembly and phase separation methods, electrospinning is a more powerful and facile technique to fabricate nanofibrous materials, which can greatly tune the dimensions of nanofibers and allow the fabrication of nanofibers from a wide range of materials [52-54]. In a typical electrospinning setup, as shown in Figure 1.5 B, a polymer solution or melt is firstly prepared, and then is pumped through a thin nozzle that serves as an electrode, where high voltage would be applied. The liquid droplet is elongated and the formed nanofibers are subsequently collected at a counter electrode substrate [53]. Electrospinning has been extensively studied and thousands of relevant articles have been published in the past decade [53, 54].

1.4 Polymer Nanocomposites

Table 1.2 Density and mechanical properties of reinforcing agents [9, 28].

Material	ρ/g cm^{-3}	σ_f(GPa)	E_A (GPa)	E_T(GPa)
Kevlar-49 fiber	1.4	3.5	124-130	2.5
Carbon fiber	1.8	1.5-5.5	150-500	---
Steel wire	7.8	4.1	210	---
Clay nanoplatelets	---	---	170	---
Carbon nanotubes	---	11-63	270-950	---
Boron nanowhisker	---	2-8	250-360	---
Cellulose nanocrystal	1.6	7.5-7.7	110-220	10-50
Chitin nanocrystal	---	---	150	15

Note: ρ = density, σ_f = tensile strength, E_A= elastic modulus in axial direction, E_T=elastic modulus in transverse direction.

Polymer nanocomposites are polymer-matrix composites containing materials that have at least one dimension below about 100 nm [55]. Due to the excellent mechanical performance and large surface area/volume ratio of nanofillers, nanocomposites can exhibit higher mechanical properties compared with neat polymer and conventional composites reinforced with micron-sized particles and fibers [55-59]. One key milestone in the development of nanocomposites is the production of nanoclay-polyamide systems from Toyota in 1980s [60]. After that, a large number of polymer nanocomposites have been developed, where the utilized fillers mainly include layered silicates, multi-walled/single-walled carbon nanotubes, nanocellulose and chitin nanocrystals because of their superior properties (Table 1.1) [9, 28, 55-59, 61-68]. The ultimate mechanical

properties of nanocomposites depend on many factors such as mechanical performance of polymer matrices and fillers, filler dispersion, filler size and aspect ratio, adhesion between fillers and matrices. To date, tremendous efforts over the past two decades have been devoted to improving the fillers' adhesion with polymers and their dispersion in matrices since these two factors significantly influence stress transfer in nanocomposites, and various methods have been developed to solve filler dispersion and adhesion issues, such as physical-mechanical treatment of filler/polymer mixtures, and chemical functionalization of filler and matrices [55-59]. However, it is still challenging to enhance these two properties simultaneously. For example, chemically functionalized fillers showed strong adhesion with matrices but were easy to form large agglomerates that adversely affect the mechanical properties of composites. In the future, polymer nanocomposites will continue to draw attention from researchers due to their excellent properties and numerous promising applications, such as light-weight car production for improving fuel efficiency, and the filler dispersion and adhesion will be still key issues to solve in this field [55-59, 61, 62].

1.5 Particle-stabilized Foams

Aqueous foams are dispersions of gas in the continuous phase of a liquid, which are of importance to a wide range of fields, including food, cosmetics, oil recovery, mineral flotation and biomedical engineering [69-78]. In addition to above applications as end products, they can also be used as appropriate intermediates to produce solid porous materials with tailored structures for insulation, packaging, transportation and tissue engineering [7, 14, 81-83]. Liquid foams are thermodynamically unstable due to the high overall free energy associated with their large gas-liquid interface area and would

collapse in a short time. The main foam destabilization mechanisms are drainage, coalescence and disproportionation (Ostwald ripening or coarsening). Drainage is the separation between the liquid phase and gas phase of foams driven by gravity and results in the formation of thin films and plateau borders among gas bubbles. Coalescence occurs when the thin films between these bubbles rupture, leading to the merging of neighboring bubbles. The driving force of disproportionation is the Laplace pressure difference between different sized bubbles ($\Delta P=2\gamma/r$, where γ is surface tension and r is the bubble radius), resulting in gas diffusion from smaller bubbles into large bubbles [84-87]. To improve the aqueous foam stability, surfactants and biomolecules such as proteins and lipids are often employed to reduce large gas-liquid free energy. However, surfactants such as sodium dodecylsulfate (SDS) and cetyltrimethylammonium bromide (CTAB) are only able to stabilize gas bubbles very shortly due to their low desorption energy at gas-liquid interface (few kTs, k is the Boltzmann's constant and T is the temperature) [85, 88, 89].

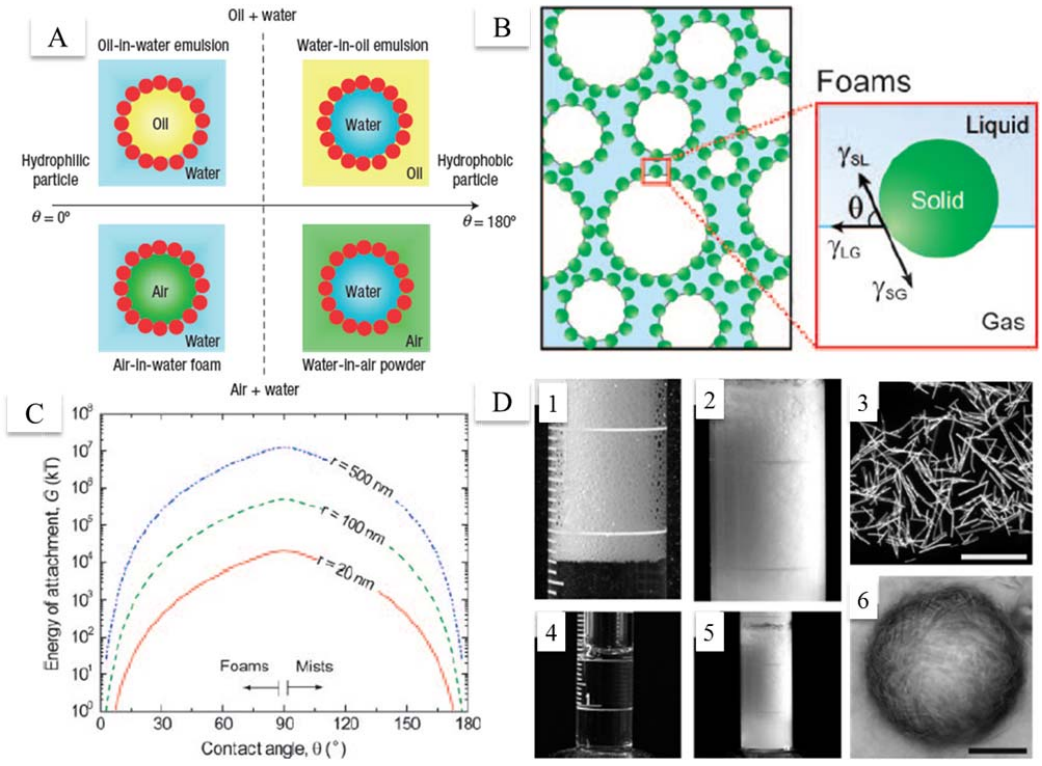

Figure 1.6 (A) For particle-oil-water mixtures, "Pickering emulsion" drops of oil-in-water or water-in-oil are stabilized by hydrophilic or hydrophobic particles respectively. For particle-air-water mixtures, "Pickering foams" air-in-water or "Liquid marbles" water-in-air are stabilized by hydrophilic or hydrophobic particles, respectively [72]; (B) The colloidal particle is absorbed at the air-water interface and its contact angle θ is determined by the balance of three interfacial tensions [87]; (C) Attachment energy of colloidal particles at an air-water interface as a function of the contact angle for different sized particles [87]; (D) The appearance of aqueous foams stabilized by (D1) sodium dodecylsulfate (SDS) and (D2) SU-8 microrods with diameters of less than 1 μm and lengths of a few tens μm. (D1) and (D2) were taken 10-15 mins after the foams were formed. (D4) and (D5) showed the appearance of (D1) and (D2) after their 2 days of storage, respectively. (D3) Optical micrograph of the SU-8 microrods (scale bar: 50 μm) and (D6) Microrod-stabilized air bubble (scale bar: 50 μm) [90].

In addition to conventional interface stabilizers-surfactants and biomolecules, colloidal particles have been used to stabilize oil droplets for more than a century and the resulting Pickering emulsions (oil in water or water in oil in Figure 1.6 A) exhibit remarkable stability [72, 85]. Recently, various materials have demonstrated their effectiveness as stabilizers of air-water interface, including metallic, ceramic and polymeric particles, with sizes ranging from nanometer to micrometers [78, 83, 87, 89-93]. These foams stabilized by particles with appropriate wettability at air-water interface can survive for weeks or years and many of them are even able to withstand more harsh conditions, such as drying and vacuum treatment. The excellent foam stability is attributed to the formation of a solid layer at the high energy interface (interfacial armor) that can act as a mechanical barrier to prevent bubbles from coalescence or disproportionation [90-97]. The adsorption of particles at an air-water interface significantly depends on their hydrophobicity, which can be accessed by the contact angle, θ. The position of the particles at the interface lies on a balance between air-water, air-solid and water-solid interfacial tensions, as shown in Figure 1.6 B [87]. The energy required for their detachment from air-water interface can be calculated by the equation: $\Delta G=\pi R^2 \gamma_{\alpha\beta} (1- \left| \cos\theta \right|)^2$, where θ is the contact angle of particle at the interface, $\gamma_{\alpha\beta}$ is the interfacial tension and R is the particle radius. The value of ΔG can be several orders of magnitude greater than the thermal energy (kT) (Figure 1.6 C) as opposed to low interfacial desorption energy of surfactants. Therefore, the particles are considered to be irreversibly trapped at the interface [87].

Particle-stabilized foams have been extensively investigated for the last decade due to their exceptional stability and tremendous potential applications for many areas.

In 2004, Alargova et al. showed that anisotropic particles-microrods with higher aspect ratio than spherical particles were able to stabilize the aqueous foams in the absence of any additives for many days and the lifetime of the resultant foams was extremely longer than that of surfactant-assisted foams, as shown in Figure 1.6 D [90]. One of reasons for foam superstabilization arised from high mechanical rigidity of intertwined rod net (Figure 1.6 D6). In 2005, Binks et al. demonstrated that the wetting properties of particles greatly influenced the liquid foamability and aqueous foams can be stabilized by solely silica nanoparticles with partially hydrophobicity and the resulting foams were able to hinder coalescence and disproportionation [91]. Many particles do not possess the appropriate hydrophobicity for foam stabilization but their wetting properties can be easily tuned by a number of methods, including physical adsorption of surfactants and chemically grafting hydrophobic chains on particle surface. In 2006, Gonzenbach et al. reported a facile and versatile approach to fabricate ultrastable particle-stabilized foams. These starting colloidal particles (alumina and silica) were quite hydrophilic but their hydrophobicity can be improved to be suitable for foaming with in-situ absorption of short chain amphiphilic molecules on these particle surfaces. The produced foams did not show any drainage and the ultrastabiliy of foams resulted from strong particle attachment at the air-water interface and the formation of an attractive particle network at the interface and throughout the foam lamella [92]. Besides above three representing papers in the field of particle-stabilized foams, there are many other great examples of particles as useful air-water interface stabilizers, such as polymer latex, calcium carbonate rods, and gold nanoparticles [78, 98-101].

1.6 Thesis Overview

There is a growing interest in exploring renewable materials for a wide range of applications owing to their abundance, sustainability, and unique inherent properties. Chitin, the second most abundant biopolymer in nature, is an ideal candidate for various fields because of its excellent properties, such as renewability, biodegradability, antibacterial ability, chemical functionality and high stiffness. Despite these inherent benefits, the utilization of chitin has been hindered for a long time due to its strong molecular interactions and insolubility [10-14]. The discovery of many solvents to dissolve chitin has accelerated its development, but chitin is currently still underutilized and its major applications are limited to biomedical engineering, such as tissue engineering, drug delivery, wound dressing and sutures [10-14, 22, 27]. The existing solvents to dissolve chitin are often highly toxic, corrosive, volatile, or difficult to remove, and the produced chitin solution is usually very viscous. As a result, chitin dissolution causes many issues, including environmental pollution, health concern, and high production cost, and detracts from sustainable nature of chitin [10-14, 20-23]. Therefore, it is highly beneficial to develop chitin-based materials without employing chitin dissolution.

The main objective of this thesis is to produce chitin nanofibers (CNFs) without employing chitin dissolution and to utilize them for composites and foams. The specific aims are listed as follows:

1) Produce the CNFs without forming strong network structures from crab α-chitin using a physical-mechanical method

2) Develop a route to create porous nanofibrous materials utilizing CNFs

3) Investigate the reinforcing effect of CNFs in polymer matrices

4) Study the interfacial properties of CNFs and create aqueous foams from renewable high-aspect-ratio CNFs

Chapter 2 describes a method for preparing CNFs from crab α-chitin and elucidates CNFs' properties, such as morphological, optical, thermal, and rheological characteristics. Chapter 3 focuses on developing CNF-based porous materials using a freeze drying technique and discussing the corresponding structure formation mechanism. Chapter 4 presents the characterization of morphological, interfacial, thermal, mechanical properties of polymer nanocomposites and investigates the role of chitin in composite. In chapter 5, a method to produce the CNF-stabilized aqueous foam is demonstrated and the interfacial properties of CNFs are elaborated. Concluding remarks and future research are provided in chapter 6.

1.7 References

[1]. Serrano-Ruiz, J. C.; Luque, R.; Sepúlveda-Escribano, A. Transformations of Biomass-Derived Platform Molecules: from High Added-Value Chemicals to Fuels via Aqueous-Phase Processing. *Chemical Society Reviews* **2011**, 40, 5266-5281.

[2]. Sheldon, R. A. Green and Sustainable Manufacture of Chemicals from Biomass: State of the Art. *Green Chemistry* **2014**, 16, 950-963.

[3]. Irimia-Vladu, M. "Green" Electronics: Biodegradable and Biocompatible Materials and Devices for Sustainable Future. *Chemical Society Reviews* **2014**, 43, 588-610.

[4]. Schnepp, Z. Biopolymers as a Flexible Resource for Nanochemistry. *Angewandte Chemie International Edition* **2013**, 52, 1096-1108.

[5]. Zhu. H.; Fang, Z.; Preston, C.; Li, Y.; Hu, L. Transparent Paper: Fabrications, Properties, and Device Applications. *Energy and Environmental Science* **2014**, 7, 269-287.

[6]. Korhonen, J. T.; Hiekkataipale, P.; Malm, J.; Karppinen, M.; Ikkala, O.; Ras, R. H. A. Inorganic Hollow Nanotube Aerogels by Atomic Layer Deposition onto Native Nanocellulose Templates. *ACS Nano* **2011**, 5, 1967-1974.

[7]. Ng, R.; Zang, R.; Yang, K. K.; Liu, N.; Yang, S. T. Three-dimensional Fibrous Scaffolds with Microstructures and Nanotextures for Tissue Engineering. *RSC Advances* **2012**, 2, 10110-10124.

[8]. Capadona, J. R.; Van Den Berg, O.; Capadona, L. A.; Schroeter, M.; Rowan, S. J.; Tyler, D. J.; Weder, C. A Versatile Approach for the Processing of Polymer Nanocomposites with Self-assembled Nanofibre Templates. *Nature Nanotechnology* **2007**, 2, 765-769.

[9]. Moon, R. J.; Martini, A.; Nairn, J.; Simonsen, J.; Youngblood, J. Cellulose Nanomaterials Review: Structure, Properties and Nanocomposites. *Chemical Society Reviews* **2011**, 40, 3941-3994.

[10]. Rinaudo, M. Chitin and Chitosan: Properties and Applications. *Progress in Polymer Science* **2006**, 31, 603-632.

[11]. Pillai, C. K. S.; Paul, W.; Sharma, C. P. Chitin and Chitosan Polymers: Chemistry, Solubility and Fiber Formation. *Progress in Polymer Science* **2009**, 34, 641-678.

[12]. Khor, E. Chitin: Fulfilling a Biomaterials Promise. Elsevier **2001**.

[13]. Nair, K. G.; Dufresne, A. Crab Shell Chitin Whisker Reinforced Natural Rubber Nanocomposites. 1. Processing and Swelling Behavior. *Biomacromolecules* **2003**, 4, 657-665.

[14]. Rinaudo, M. Main Properties and Current Applications of Some Polysaccharides as Biomaterials. *Polymer International* **2008**, 57, 397-430.

[15]. Gardner, K. H; Blackwell, J. Refinement of the Structure of β-chitin. *Biopolymers* **1975**, 14, 1581-1595.

[16]. Minke, R.; Blackwell, J. The Structure of α-chitin. *Journal of Molecular Biology* **1978**, 120, 167-181.

[17]. Raabe, D.; Sachs, C.; Romano, P. The Crustacean Exoskeleton as an Example of a Structurally and Mechanically Graded Biological Nanocomposite Material. *Acta Materials* **2005**, 53, 4281-4292.

[18]. Nikolov, S.; Petrov, M.; Lymperakis, L.; Friák, M.; Sachs, C.; Fabritius, H.; Raabe, D.; Neugebauer, J. Revealing the Design Principles of High-Performance Biological Composites Using Ab initio and Multiscale Simulations: The Example of Lobster Cuticle. *Advanced Materials* **2010**, 22, 519-526.

[19]. Vukusic, P.; Hallam, B.; Noyes, J. Brilliant Whiteness in Ultrathin Beetle Scales. *Science* **2007**, 315, 348.

[20]. Fan, Y.; Saito, T.; Isogai, A. Preparation of Chitin Nanofibers from Squid Pen β-Chitin by Simple Mechanical Treatment under Acid Conditions. *Biomacromolecules*

2008, 9, 1919–1923.

[21]. Ifuku, S.; Nogi, M.; Abe, K.; Yoshioka, M.; Morimoto, M.; Saimoto, H.; Yano, H. Preparation of Chitin Nanofibers with a Uniform Width as α-Chitin from Crab Shells. *Biomacromolecules* **2009**, 10, 1584-1588.

[22]. Min, B. M.; Lee, S. W.; Lim, J. N.; You, Y.; Lee, T. S.; Kang, P. H.; Park, W. H. Chitin and Chitosan Nanofibers: Electrospinning of Chitin and Deacetylation of Chitin Nanofibers. *Polymer* **2004**, 45, 7137-7142.

[23]. Duan, B.; Chang, C.; Ding, B.; Cai, J.; Xu, M.; Feng, S.; Ren, J.; Shi, X.; Du, Y.; Zhang, L. High Strength Films with Gas-Barrier Fabricated from Chitin Solution Dissolved at Low Temperature. *Journal of Materials Chemistry A* **2013**, 1, 1867-1874.

[24]. Kumar, M. N. V. Chitin and Chitosan Fibres: a Review. *Bulletin Materials Science* **1999**, 22, 905-915.

[25]. Xie, H.; Zhang, S.; Li, S. Chitin and Chitosan Dissolved in Ionic Liquids as Reversible Sorbents of CO2. *Green Chemistry* **2006**, 8, 630-633.

[26]. Bhatnagar, A.; Sillanpää, M. Applications of Chitin- and Chitosan-Derivatives for the Detoxification of Water and Wastewater -A Short Review. *Advances in Colloid and Interface Science* **2009**, 152, 26-38.

[27]. Jayakumar, R.; Menon, D.; Manzoor, K.; Nair, S. V.; Tamura, H. Biomedical Applications of Chitin and Chitosan Based Nanomaterials-A Short Review. *Carbohydrate Polymers* **2010**, 82, 227-232.

[28]. Zeng, J.; He, Y.; Li, S.; Wang, Y. Chitin Whiskers: an Overview. *Biomacromolecules* **2012**, 13, 1-11.

[29]. Paillet, M.; Dufresne, A. Chitin Whisker Reinforced Thermoplastic Nanocomposites. *Macromolecules* **2001**, 34, 6527-6530.

[30] Morin, A.; Dufresne, A. Nanocomposites of Chitin Whiskers from Riftia Tubes and Poly(caprolactone). *Macromolecules* **2002**, 35, 2190-2199.

[31]. Nair, K. G.; Dufresne, A. Crab Shell Chitin Whisker Reinforced Natural Rubber Nanocomposites. 1. Processing and Swelling Behavior. *Biomacromolecules* **2003**, 4, 657-665.

[32]. Sriupayo, J.; Supaphol, P.; Blackwell, J.; Rujiravanit, R. Preparation and Characterization of α-chitin Whisker-reinforced Poly(vinyl alcohol) Nanocomposite Films with or without Heat Treatment. *Polymer* **2005**, 46, 5637-5644.

[33]. Junkasem, J.; Rujiravanit, R.; Supaphol, P. Fabrication of α-chitin Whisker-Reinforced Poly(vinyl alcohol) Nanocomposite Nanofibres by Electrospinning. *Nanotechnology* **2006**, 17, 4519-4528.

[34]. Hariraksapitak, P.; Supaphol, P. Preparation and Properties of α-Chitin-Whisker-Reinforced Hyaluronan–Gelatin Nanocomposite Scaffolds. *Journal of Applied Polymer Science* **2010**, 117, 3406-3418.

[35]. Zeng, M.; Gao, H.; Wu, Y.; Fan, L.; Li, A. Preparation and Characterization of Nanocomposite Films from Chitin Whisker and Waterborne Poly(ester-urethane) With or Without Ultra-Sonification Treatment. *Journal of Macromolecular Science, Part A: Pure and Applied Chemistry* **2010**, 47, 867-876.

[36]. Miller, K. S.; Krochta, J. M. Oxygen and Aroma Barrier Properties of Edible Films: a Review. *Trends in Food Science and Technology* **1997**, 8, 228-237.

[37]. Lavoine, N.; Desloges, I.; Dufresne, A.; Bras, J. Microfibrillated Cellulose – Its Barrier Properties And Applications In Cellulosic Materials: A Review. *Carbohydrate Polymers* **2012**, 90, 735–764.

[38]. La Torre, A.; Gimenez-Lopez, M. d. C.; Fay, M. W.; Rance, G. A.; Solomonsz, W. A.; Chamberlain, T. W.; Brown, P. D.; Khlobystov, A. N. Assembly, Growth, and Catalytic Activity of Gold Nanoparticles in Hollow Carbon Nanofibers. *ACS Nano* **2012**, 6, 2000-2007.

[39]. Chen, L. F.; Zhang, X. D.; Liang, H. W.; Kong, M.; Guan, Q. F.; Chen, P.; Wu, Z. Y.; Yu, S. H. Synthesis of Nitrogen-Doped Porous Carbon Nanofibers as an Efficient Electrode Material for Supercapacitors. *ACS Nano* **2012**, 6, 7092-7102.

[40]. Qie, L.; Chen, W. M.; Wang, Z. H.; Shao, Q. G.; Li, X.; Yuan, L. X.; Hu, X. L.; Zhang, W. X.; Huang, Y. H. Nitrogen-Doped Porous Carbon Nanofiber Webs as Anodes for Lithium Ion Batteries with a Superhigh Capacity and Rate Capability. *Advanced Materials* **2012**, 24, 2047-2050.

[41]. Suginta, W.; Khunkaewla, P.; Schulte, A. Electrochemical Biosensor Applications of Polysaccharides Chitin and Chitosan. *Chemical Reviews* **2013**, 113, 5458-5479.

[42]. Tran, H. D.; Wang, Y.; D'Arcy, J. M.; Kaner, R. B. Toward an Understanding of the Formation of Conducting Polymer Nanofibers. *ACS Nano* **2008**, 2, 1841-1848.

[43]. Hartgerink, J. D.; Beniash, E.; Stupp, S. I. Self-assembly and Mineralization of Peptide-Amphiphile Nanofibers. *Science* **2001**, 294, 1684-1688.

[44]. Aida, T.; Meijer, E. W.; Stupp, S. I. Functional Supramolecular Polymers. *Science* **2012**, 335, 813-817.

[45]. Hamada, D.; Yanagihara, I.; Tsumoto, K. Engineering Amyloidogenicity towards the Development of Nanofibrillar Materials. *Trends in Biotechnology* **2004**, 22, 93-97.

[46]. Lutolf, M. P.; Hubbell, J. A. Synthetic Biomaterials as Instructive Extracellular Microenvironments for Morphogenesis in Tissue Engineering. *Nature Biotechnology* **2005**, 23, 47-55.

[47]. Ornatska, M.; Peleshanko, S.; Genson, K. L.; Rybak, B.; Bergman, K. N.; Tsukruk, V. V. Assembling of Amphiphilic Highly Branched Molecules in Supramolecular Nanofibers. *Journal of American Chemical Society* **2004**, 126, 9675-9684.

[48]. Ma, P. X.; Zhang, R. Synthetic Nano-scale Fibrous Extracellular Matrix. *Journal of Biomedical Materials Research* **1999**, 46, 60-72.

[49]. Smith, L. A.; Ma, P. X. Nano-fibrous Scaffolds for Tissue Engineering. *Colloids and Surfaces B: Biointerfaces* **2004**, 39, 125-131.

[50]. Ma, Z.; Kotaki, M.; Inai, R.; Ramakrishna, S. Potential of Nanofiber Matrix as Tissue-Engineering Scaffolds. *Tissue Engineering* **2005**, 11, 101-109.

[51]. Zhong, C.; Cooper, A.; Kapetanovic, A.; Fang, Z.; Zhang, M.; Rolandi, M. A Facile Bottom-Up Route to Self-Assembled Biogenic Chitin Nanofibers. *Soft Matter*, **2010**, 6, 5298-5301.

[52]. Barnes, C. P.; Sell, S. A.; Boland, E. D.; Simpson, D. G.; Bowlin, G. L. Nanofiber Technology: Designing the Next Generation of Tissue Engineering Scaffolds. *Advanced Drug Delivery Reviews* **2007**, 59, 1413-1433.

[53]. Greiner, A.; Wendorff, J. H. Electrospinning: A Fascinating Method for the Preparation of Ultrathin Fibers. *Angewandte Chemie International Edition* **2007**, 46, 5670-5703.

[54]. Persano, L.; Camposeo, A.; Tekmen, C.; Pisignano, D. Industrial Upscaling of Electrospinning and Applications of Polymer Nanofibers: A Review. Macromolecular *Materials and Engineering* **2013**, 298, 504-520.

[55] Gupta, R. K.; Kennel, E.; Kim, K. Polymer Nanocomposites Handbook. CRC Press **2010**.

[56]. Goettle, L. A.; Lee, K. Y.; Thakkar, H. Layered Silicate Reinforced Polymer Nanocomposites: Development and Applications. *Polymer Reviews* **2007**, 47, 291-317.

[57]. Fu, S.; Feng, X.; Lauke, B.; Mai, Y. Effects of Particle Size, Particle/Matrix Interface Adhesion and Particle Loading on Mechanical Properties of Particulate–Polymer Composites. *Composites: Part B* **2008**, 39, 933-961.

[58]. Miao, C.; Hamad, W. Y. Cellulose Reinforced Polymer Composites and Nanocomposites: A Critical Review. *Cellulose* **2013**, 20, 2221-2262.

[59]. Bredeau, S.; Peeterbroeck, S.; Bonduel, D.; Alexandre, M. Mini-review from Carbon Nanotube Coatings to High-Performance Polymer Nanocomposites. *Polymer International* **2008**, 57, 547-553.

[60] Okada, A.; Fukushima, Y.; Kawasumi, M.; Inagaki, S.; Usuki, A.; Sugiyama, S.; Kurauchi, T.; Kamigaito, O. Polyamide Polymeric Matric Bonded to Silicate. U.S. Patent

4,739,007 **1988.**

[61]. Chen, B.; Evans, J. R. G.; Greenwell, H. C.; Boulet, P.; Coveney, P. V.; Bowden, A. A.; Whiting, A. A Critical Appraisal of Polymer- Clay Nanocomposites. *Chemical Society Reviews* **2008**, 37, 568-594.

[62]. Klemm, D.; Kramer, F.; Moritz, S.; Lindström, T.; Ankerfors, M.; Gray, D.; Dorris, A. Nanocelluloses: A New Family of Nature-Based Materials. *Angewandte Chemie International Edition* **2011**, 50, 5438-5466.

[63]. Brown, E. E.; Laborie, M. G. Bioengineering Bacterial Cellulose/Poly(ethylene oxide) Nanocomposites. *Biomacromolecules* **2007**, 8, 3074-3081.

[64]. Chatterjee, T.; Mitchell, C. A.; Hadjiev, V. G.; Krishnamoorti, R. Hierarchical Polymer–Nanotube Composites. *Advanced Materials* **2007**, 19, 3850-3853.

[65]. Kim, I. T.; Lee, J. H.; Shofner, M. L.; Jacob, S. K.; Tannenbaum, R. Crystallization Kinetics and Anisotropic Properties of Polyethylene Oxide/Magnetic Carbon Nanotubes Composite Films. *Polymer* **2012**, 53, 2402-2411.

[66]. Abdul Khalil, H. P. S.; Bhat, A. H.; Ireana Yusra, A. F. Green Composites from Sustainable Cellulose Nanofibrils: a Review. *Carbohydrate Polymers* **2012**, 87, 963-979.

[67]. Lee, J.; Shofner, M. L. Dispersion of Polymer-Decorated Hydroxyapatite Nanoparticles in Poly(ethylene oxide) at Low Grafting Densities. *Polymer* **2012**, 53, 5146-5154.

[68]. Yang, J.; Han, C.; Duan, J.; Xu, F.; Sun, R. Mechanical and Viscoelastic Properties of Cellulose Nanocrystals Reinforced Poly(ethylene glycol) Nanocomposite Hydrogels. *ACS Applied Materials and Interfaces* **2013**, 5, 3199-3207.

[69]. Murray, B. S.; Ettelaie, R. Foam Stability: Proteins and Nanoparticles. *Current Opinion in Colloid and Interface Science* **2004**, 9, 314-320.

[70]. Dickinson, E. Food Emulsions and Foams: Stabilization by Particles. *Current Opinion in Colloid and Interface Science* **2010**, 15, 40-49.

[71]. Pei, Z. J; Schmidt, K. A. Ice Cream: Foam Formation and Stabilization-A Review. *Food Reviews International* **2010**, 26, 122-137.

[72]. Binks, B. P.; Murakami, R. Phase Inversion of Particle-stabilized Materials from Foams to Dry Water. *Nature Materials* **2006**, 5, 865-869.

[73]. Farajzadeh, R.; Andrianov, A.; Krastev, R.; Hirasaki, G. J.; Rossen, W. R. Foam–oil Interaction in Porous Media: Implications for Foam assisted Enhanced Oil Recovery. *Advanced in Colloid and Interface Science* **2012**, 183, 1-13.

[74]. Lee, J.; Nikolov, A.; Wasan, D. Stability of Aqueous Foams in the Presence of Oil:

On the Importance of Dispersed vs Solubilized Oil. *Industrial and Engineering Chemistry Research* **2013**, 52, 66-72.

[75]. Shibata, J.; Fuerstenau, D. W. Flocculation and Flotation Characteristics of Fine Hematite with Sodium Oleate. *International Journal of Mineral Processing* **2003**, 72, 25-32.

[76]. Dinsmore. A. D.; Hsu, M. F.; Nikolaides, M. G.; Marquez, M.; Bausch. A. R.; Weitz, D. A. Colloidosomes: Selectively Permeable Capsules Composed of Colloidal Particles. *Science* **2002**, 298, 1006-1009.

[77]. Lindner, J. R. Microbubbles in Medical Imaging: Current Applications and Future Directions. *Nature* **2004**, 3, 527-532.

[78]. Mohamedi, G.; Azmin, M.; Pastoriza-Santos, I.; Huang, V.; Pérez-Juste, J.; Liz-Marzán, L.; Edirisinghe, M.; Stride, E. Effects of Gold Nanoparticles on the Stability of Microbubbles. *Langmuir* **2012**, 28, 13808-13815.

[81]. Clyne, T. W.; Golosnoy, I. O.; Tan, J. C.; Markaki, A. E. Porous Materials for Thermal Management under Extreme Conditions. *Philosophical Transactions of the Royal Society A* **2006**, 364, 125-146.

[82]. Banhart, J. Metal Foams: Production and Stability. *Advanced Engineering Materials* **2006**, 8, 781-794.

[83]. Studart, A.; Nelson, A.; Iwanovsky, B.; Kotyrba, M.; Kündig, A. A.; Dalla Torre, F. H.; Gonzenbach, U. T.; Gauckler, L. J.; Löffler, J. F. Metallic Foams from Nanoparticle-stabilized Wet Foams and Emulsions. *Journal of Materials Chemistry* **2012**, 22, 820-823.

[84]. Pugh, R. J. Foaming, Foam Films, Antifoaming and Defoaming. *Advances in Colloid and Interface Science* **1996**, 64, 67-142.

[85]. Binks, B. P. Particles as Surfactants-Similarities and Differences. *Current Opinion in Colloid and Interface Science* **2002**, 7, 21-41.

[86]. Kaptay, G. Interfacial Criteria for Stabilization of Liquid Foams by Solid Particles. *Colloids and Surfaces A: Physicochemical and Engineering Aspects* **2004**, 230, 67-80.

[87]. Studart, A. R.; Gonzenbach, U. T.; Tervoort, E.; Gauckler, L. J. Processing Routes to Macroporous Ceramics: A Review. *Journal of American Ceramic Society* **2006**, 89, 1771-1789.

[88]. Fameau, A; Saint-Jalmes, A.; Cousin, F.; Houssou, B. H.; Novales, B.; Navailles, L.; Nallet, F.; Gaillard, C.; Boué, F.; Douliez, J. Smart Foams: Switching Reversibly between Ultrastable and Unstable Foams. *Angewandte Chemie International Edition* **2011**, 123, 8414-8419.

[89]. Carl, A.; Klitzing, R. Smart Foams: New Perspectives towards Responsive

Composite Materials. *Angewandte Chemie International Edition* **2011**, 50, 11290-11292.

[90]. Alargova, R. G.; Warhadpande, D. S.; Paunov, V. N.; Velev, O. D. Foam Superstabilization by Polymer Microrods. *Langmuir* **2004**, 20, 10371-10374.

[91]. Binks, B. P.; Horozov, T. S. Aqueous Foams Stabilized Solely by Silica Nanoparticles. *Angewandte Chemie International Edition* **2005**, 44, 3722-3725.

[92]. Gonzenbach, U. T.; Studart, A. R.; Tervoort, E.; Gauckler, L. J. Ultrastable Particle-Stabilized Foams. *Angewandte Chemie International Edition* **2006**, 45, 3526-3530.

[93]. Gonzenbach, U. T.; Studart, A. R.; Tervoort, E.; Gauckler, L. J. Stabilization of Foams with Inorganic Colloidal Particles. *Langmuir* **2006**, *22,* 10983-10988.

[94]. Subramaniam, A. B.; Abkarian, M.; Mahadevan, L.; Stone, H. A. Mechanics of Interfacial Composite Materials. *Langmuir* **2006**, 22, 10204-10208.

[95]. Abkarian, M.; Subramaniam, A. B.; Kim, S.; Larsen, R. J.; Yang, S; Stone, H. A. Dissolution Arrest and Stability of Particle-Covered Bubbles. *Physical Review Letters* **2007**, 99, 188301.

[96]. Hunter, T. N.; Pugh, R. J.; Franks, G. V.; Jameson, G. J. The Role of Particles in Stabilising Foams and Emulsions. *Advances in Colloid and Interface Science* **2008**, 137, 57-81.

[97]. Horozov, T. S. Foams and Foam Films Stabilised by Solid Particles. *Current Opinion in Colloid and Interface Science* **2008**, 13, 134-140.

[98]. Zhou, W.; Cao, J.; Liu, W.; Stoyanov, S. How Rigid Rods Self-assemble at Curved Surfaces. *Angewandte Chemie International Edition* **2009**, 48, 378-381.

[99]. Fujii, S.; Mochizuki, M.; Aono, K.; Hamasaki, S.; Murakami, R.; Nakamura, Y. pH-Responsive Aqueous Foams Stabilized by Hairy Latex Particles. *Langmuir* **2011**, 27, 12902-12909.

[100]. Jin, H.; Zhou, W.; Cao, J.; Stoyanov, S. D.; Blijdenstein, T. B. J.; Groot, P. W. N.; Arnaudov, L. N.; Pelan, E. G. Super Stable Foams Stabilized by Colloidal Ethyl Cellulose Particles. *Soft Matter* **2012**, 8, 2194-2205.

[101]. Guevara, J. S.; Mejia, A. F.; Shuai, M.; Chang, Y.; Mannan, M. S.; Cheng, Z. Stabilization of Pickering Foams by High-aspect-ratio Nano-sheets. *Soft Matter* **2013**, 9, 1327-1336.

CHAPTER 2

ISOLATION OF CHITIN NANOFIBERS FROM CRAB SHELLS AND CHARACTERIZATION OF THEIR PROPERTIES

2.1 Overview

Significant attention has been recently devoted to developing advanced materials from renewable resources. The production of sustainable nanofiber-based materials is one emerging area of interest. Chitin, the second most abundant biopolymer in nature, is a great candidate for various applications because of its remarkable properties, such as abundance, renewability, biodegradability, biocompatibility, antibacterial activity and high stiffness. However, chitin is currently still not well explored due to its strong molecular interactions, which makes processing difficult. Here, we report a novel route to produce renewable and biodegradable nanofibers starting with purified crab α-chitin. The method involves a physical high pressure homogenization process under acid conditions and does not involve organic solvents. The produced nanofibers have diameters of ~20 nm and are dispersed well in mildly acidic aqueous solution stabilized via electrostatic repulsion, without forming strong network structures. The resulting nanofiber film exhibits high optical transparency and shows great gas barrier properties, suggesting potential applications in food, beverage and medicine packaging. Owing to their highly crystalline structure and great dispersion in solution, chitin-based nanofibers are promising reinforcing materials for polymer composites. In addition, these renewable and biodegradable nanofibrous materials may be also useful for many other areas, such as

catalysis, sensors, electronics (energy storage, transistors etc.), and biomedical engineering.

2.2 Introduction

Developing renewable materials to reduce the dependence on fossil fuel as a feedstock for a wide range of applications is becoming an increasingly important to society. Recently, significant progress has been achieved in the production of sustainable alternatives to many synthetic materials, such as bioplastics, biofuels and green electronics [1-3]. The fabrication of nanofiber-based materials from renewable resources is one emerging area of significance due to their utility in various fields, such as electronic devices, sensors, bioengineering, and structural materials [4-8].

Chitin, poly (β-(1-4)-N-acetyl-D-glucosamine, is the second most abundant biopolymer with an annual production of 10^{10} to 10^{11} tons in nature and it mainly exists in exoskeleton of arthropods or the cell wall of fungi and yeast. Recently, chitin has attracted much attention from researchers because of its extraordinary properties, such as abundance, renewability, biodegradability, biocompatibility, antibacterial activity, functionality and high stiffness and strength. However, even though it has many inherent benefits, the fabrication and application of chitin-based materials is still quite challenging mainly due to its strong molecular interactions [8-12]. Previously, chitin-based nanofibers have been fabricated using electrospinning and phase separation techniques [13, 14], but these processes required highly toxic and volatile organic solvent consumption, which detracts from the sustainable nature of chitin, and also disrupts its intrinsically high crystallinity.

Besides the bottom-up processes (e.g., electrospinning and phase separation), top-down methods have been recently reported to fabricate chitin nanofibers (CNFs) [15-17]. For example, CNFs were successful produced from crab shells and squid pen using mechanical grinding and high-power ultrasonication, respectively. The resulting CNFs were entangled together to form a highly viscous gel [15-17]. In addition, ultrasonication was not able to disintegrate CNFs from crab α-chitin, which possibly resulted from the higher crystallinity index, anti-parallel configuration and greater intermolecular interactions of α-chitin compared with β-chitin [15]. Nanofibers that form strong network structures can adversely affect dispersion in polymer composites or hinder their mobility during solvent-based assembly, and cause other processing difficulties [7, 18]. The objective of this study was to produce CNFs from crab shell α-chitin without forming strong network structures using a physical-mechanical method. Here, a high pressure homogenization process was used to extract CNFs from α-chitin purified from crab shells. The morphology, structure, and properties of the obtained nanofibers were characterized using nuclear magnetic resonance (NMR), scanning electron microscopy (SEM), atomic force microscopy (AFM), ultraviolet-visible light (UV-Vis), attenuated total reflectance (ATR), X-ray diffraction (XRD), rheometer, thermogravimetric analysis (TGA), and gas permeation system.

2.3 Experimental Methods

2.3.1 Materials

Dried crab shell flakes were purchased from TCI America. Deionized water (18.2 MΩ cm) was prepared in a Barnstead Easypure RoDi purification system. Hydrochloric acid, sodium hydroxide, acetone and ethanol were purchased from EMD Chemical Inc.

2.3.2 Extraction of CNF from Crab Shells

Dried crab shell flakes were processed to obtain purified chitin [11, 16]. Ground crab shells were refluxed in 5 wt % sodium hydroxide in DI water for 6 h to remove protein. The suspension was filtered and rinsed with DI water until the pH was 7. Next, the filtered solids were treated with 7% hydrochloric acid for 6 h at room temperature to remove minerals. After filtration and washing with DI water, the treated sample was refluxed in a 5% NaOH solution for 2 days to remove residual proteins and the other residues were eliminated by acetone and ethanol extraction. The purified chitin was dispersed in DI water under an acidic condition by magnetic stirring, and then this mixture was passed through a high-pressure homogenizer (Bee International Inc., MA USA) to generate CNFs (aqueous medium pH is ~ 4.1).

2.3.3 Materials Characterization

The degree of acetylation (DA) of the purified chitin was characterized using ^{13}C cross-polarization under magic-angle spinning (CP-MAS) NMR, which was performed on a Bruker 400 spectrometer with a spinning rate of 5 kHz, contact times of 1 ms and pulse intervals of 5 s [19]. The DA of chitin was determined using the ratio of the integral of methyl carbon atom of the N-acetyl group to the summation integrals of the six carbon atoms of the D-glucopyranosyl ring (C_1-C_6 atoms: δ 50 to 105 ppm) (Equation 2.1) [20].

$$\boldsymbol{DA = 100 \times I_{N-CH_3} / [1/6(I_{C_1} + I_{C_2} + I_{C_3} + I_{C_4} + I_{C_5} + I_{C_6})]}$$

$$= 100 \times \left(I_{N-CH_3}\right) / (1/6 \sum I_{main\ chain\ carbons}) \qquad \text{Equation 2.1}$$

The light transmittances (wavelengths: 400 to 800 nm) of chitin dispersion or CNF solid film were measurement using a UV-vis spectrometer (JASCO V-630). A cuvette filled with DI water was used as a reference for chitin dispersion measurement.

The morphologies of chitin-based materials were obtained using Field-Emission Scanning Electron Microscopy (Zeiss Ultra 60). Before imaging, these samples were coated with a thin layer of gold/palladium (Hummer IV Sputtering System) to promote conductivity. The surface features of CNF film were characterized using atomic force microscopy (AFM, Veeco Dimension 3100). The flat film was firstly attached onto a smooth silicon wafer, and then the images were collected under a tapping mode. The cantilever has a etched super-sharp (<5nm) silicon tip with a nominal spring constant of 37 N/m and a nominal frequency of 300 kHz (Applied NanoStructures, Inc., Santa Clara, CA). The surface charges of CNFs at different pH in water were measured by a Malvern Zetasizer Nano ZS 90.

The attenuated total reflectance (ATR) spectra of chitin powders and CNF film were recorded using Bruker platinum ATR (Bruker Optics, Inc., Billerica, MA). Measurements were collected from 4000 to 400 cm^{-1} with a resolution of 4 cm^{-1}, and were averaged over 64 scans. Wide angle x-ray diffraction (WAXD) patterns of chitin powder and CNF film were collected on a Rigaku Micro Max 002 (Cu Kα radiation, λ=0.154 nm) operating at 45 kV and 0.65 mA using a R-axis IVCC detection system. The diffraction patterns were analyzed using Areamax V. 3.00 and MDI Jade software. The exposure time lengths were 30 min for both samples.

Dynamic rheology of CNF dispersion (0.5% chitin) was carried out by a MCR 300 rheometer (Anton Paar, Graz, Austria) using a plate and plate geometry at 23˚C. Before the dynamic viscoelastic measurements, the linear viscoelastic region was accessed by strain sweep experiment in the range of 0.01 to 10% at a frequency of 1 Hz. The frequency sweep was conducted from 0.1 to 10 rad/s with a controlled stain of 0.005,

which was within the linear viscoelastic region. Shear viscosity was measured by increasing the shear rate from 0.1 to 1001/s at 23˚C.

Thermal stability of chitin powder and CNF film were accessed using thermogravimetric analysis (TGA) (TA Q50, TA Instruments, USA). Approximately 5-10 mg of sample was loaded into ceramic pan. The sample was heated from room temperature to 120 ˚C at a rate of 10 ˚C/min under a flowing nitrogen atmosphere (N_2 purity > 99.999%), gas flow rate: 50 ml/min), and then held at 120 ˚C for 30 min. The amount of absorbed water of chitin was estimated from the first two steps. The sample was subsequently heated up to 1000 ˚C at a rate of 10 ˚C/min with a nitrogen flow of 50 ml/min.

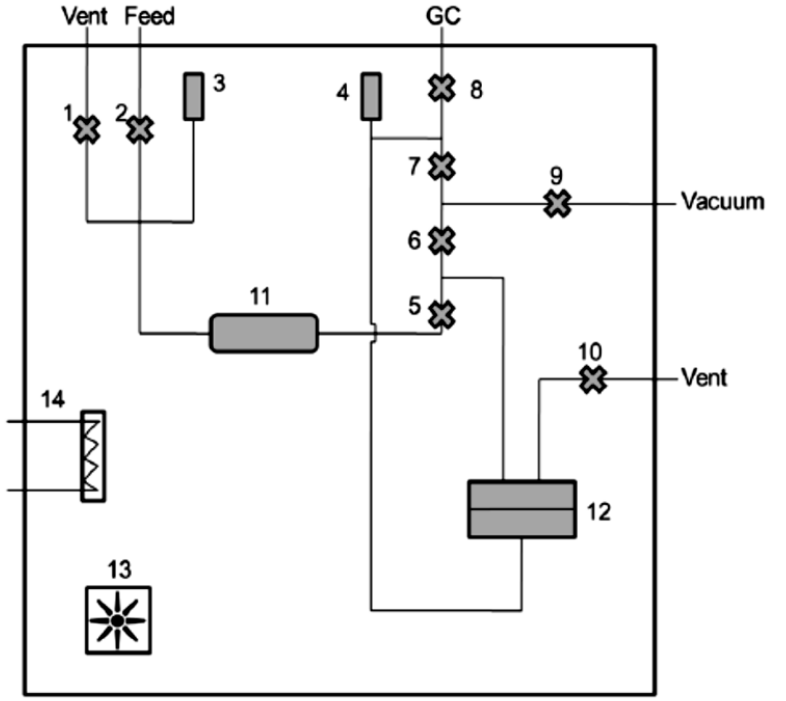

1. Vent valve 1
2. Feed valve
3. Upstream pressure transducer
4. Downstream pressure transducer
5. Upstream valve
6. Connector valve
7. Downstream valve
8. GC valve
9. Vacuum pump valve
10. Vent valve 2
11. Upstream volume
12. Permeation cell
13. Fan
14. Thermostat-controlled heater

Figure 2.1 Schematic of a constant volume permeation system [22].

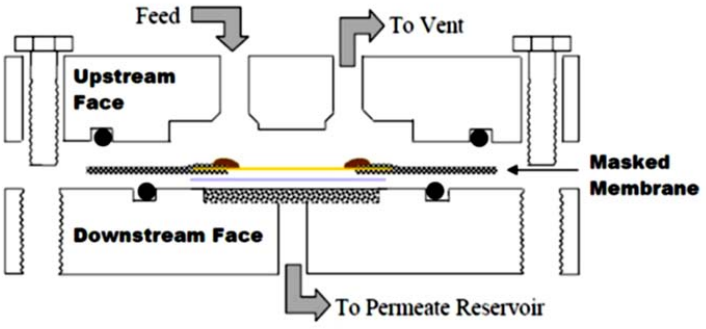

Figure 2.2 Schematic of a permeation cell for gas permeability measurement of CNF film [22].

Gas permeability of CNF film was conducted using a constant volume permeation system (Figure 2.1) at room temperature and 0% relative humidity. Detailed experiment setup has been discussed in reference 19. Briefly, CNF film was firstly sandwiched between two concentric pieces of impermeable aluminum tape and then was assembled into a permeation cell (Figure 2.2). The cell was subsequently loaded in the permeation system. The entire permeation system was degassed for over 24 hours. After a leak test, the upstream was pressurized with feed gas (O_2, N_2, H_2, CO_2 or CH_4), while the downstream was kept at vacuum. The pressure change in a constant downstream volume was recorded over time using LabView (National Instruments, Austin, TX). The permeability of CNF film was calculated based on equation 2.2 [22].

$$P = \frac{(2.94 \times 10^4)(V)(l)(dp/dt)}{(T)(A)(\Delta p)} \qquad \text{Equation 2.2}$$

Where, V is the downstream volume, L is the thickness of measured film, dp/dt is the steady state rate of pressure rise, T is the absolute temperature, A is the measured film area, and Δp is the pressure difference between the upstream and downstream [22].

2.4 Results and Discussion

2.4.1 Chitin Purification and Fibrillation from Crab Shells

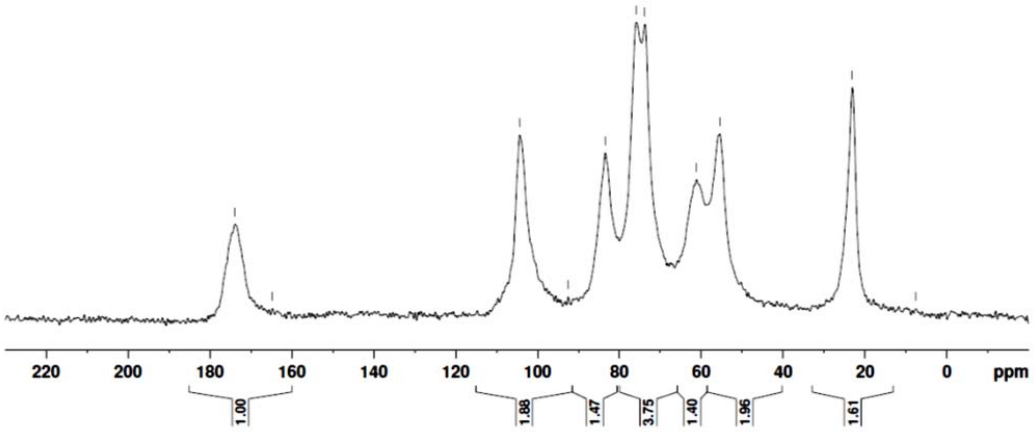

Figure 2.3 ^{13}C CP-MAS solid state NMR of purified chitin from crab shells

Crab shells mainly consist of proteins, minerals and chitin [8, 9, 12]. To achieve the purified chitin, a series of chemical treatments were performed on crab shells, such as acid treatment to remove minerals and base process to deplete proteins. The degree of acetylation (DA) is an important parameter of chitin and has been used to differentiate chitin from chitosan. While all natural chitin contains some substitution with chitosan along the chain, the polymer is called chitin when DA is greater than 50% [8, 9]. Various methods have been used to quantitatively measure the DA of chitin, including FTIR, NMR (solid and liquid state), titration, elemental analysis [20]. Here, a non-destructive method- ^{13}C CP-MAS solid state NMR was used to determine the DA of the purified chitin from crab shells. The positions of C_1, C_2, C_3, C_4, C_5, C_6 and N-CH_3 (C_7) in ^{13}C NMR spectra are 104.36, 55.54, 73.81, 83.51, 75.91, 61.20, and 23.17 ppm, as illustrated in Figure 2.3. According to equation 2.1, the DA of purified chitin is 92.4%.

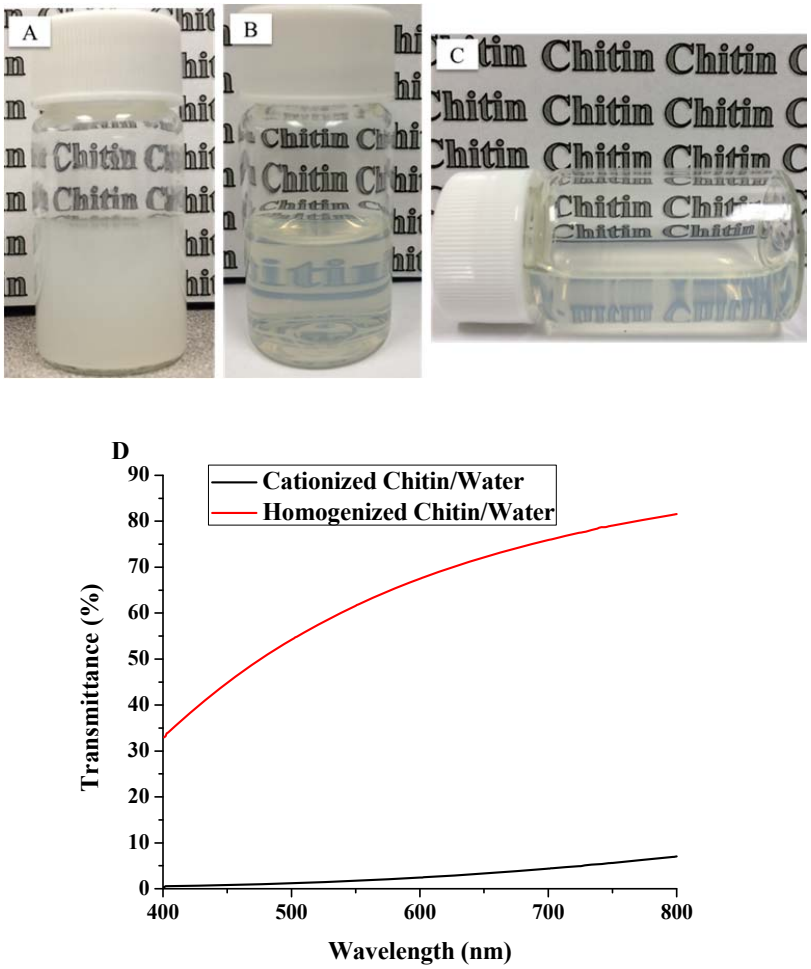

Figure 2.4 (A) Appearance of cationized chitin dispersion (purified chitin was dispersed under acid conditions for -NH_2 group cationization); (B) and (C) are the digital photos of the homogenized chitin in water with pH ~ 4.1, which was produced by a high pressure homogenization process of the cationized chitin/water; (D) Light transmittance spectra of the cationized chitin/water and homogenized chitin/water in the range of 400 to 800 nm wavelengths.

The obtained purified chitin was dispersed in acidic water resulting in cationization due to the protonation of –NH_2. The cationized chitin (chitin content: 0.5%) dispersion is hazy and has a transmittance of 7% at 800 nm (Figure 2.4 A and D). In contrast, the homogenized chitin dispersion with a pH of ~ 4.1(chitin content: 0.5%) exhibits high transparency and has a transmittance of 81% at 800 nm, as illustrated in

Figure 2.4 B and D. Meanwhile, it can flow easily under gravity (Figure 2.4 C). The zeta potentials of diluted homogenized chitin in water at pH 4-7 were measured. The homogenized chitin has a zeta potential of more than +50 mv in water at pH 4 and these values decreased when increasing the medium pH. The decrease of zeta potential upon pH increase is attributed to a decreasing protonation of $-NH_2$ group as the pKa is approached between 6 and 7 [8, 9].

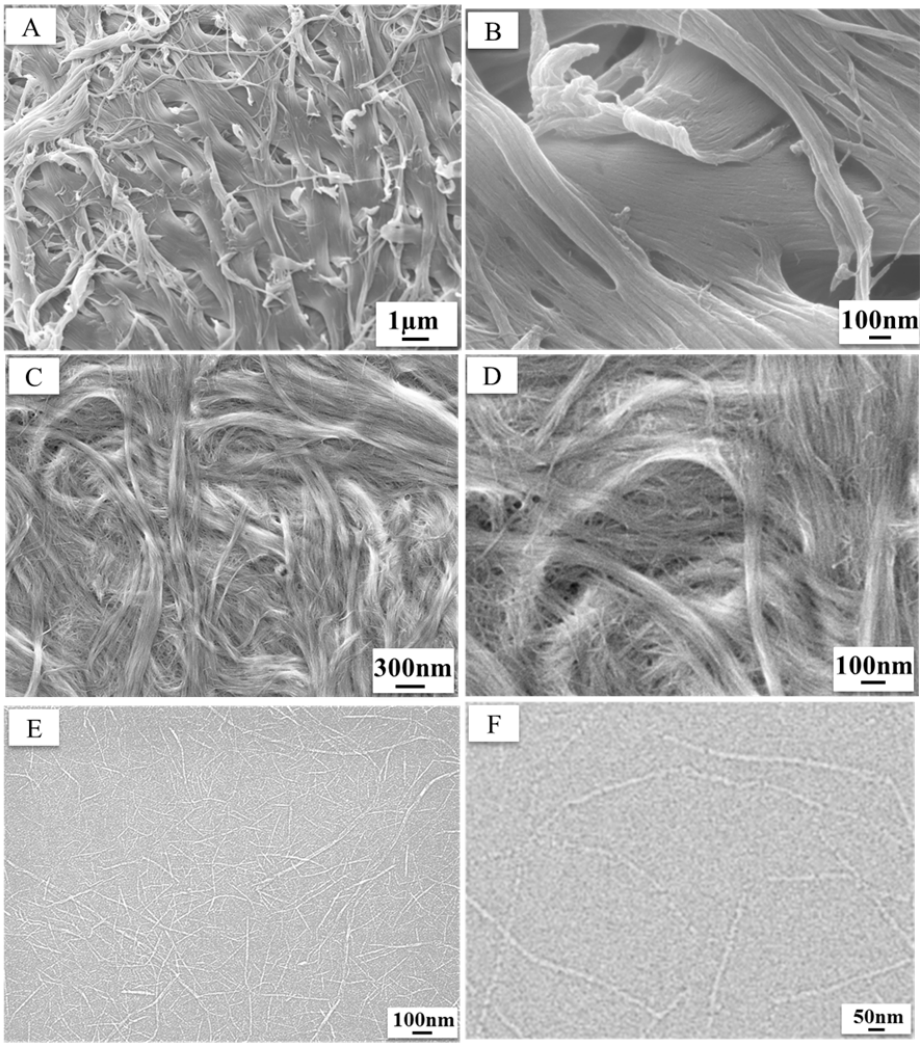

Figure 2.5 (A), (C) and (E) are the SEM images of the purified chitin, cationized chitin and homogenized chitin, respectively; (B), (D) and (F) are enlarged SEM images of above three chitin-based materials, respectively.

Crab shell has intricate hierarchical structures that are mainly produced by the assembly of chitin and proteins, and CNFs are its key elements [12]. The purified chitin was obtained as micron-sized particles, and it consisted of fibers with diameters ranging from a few tens of nanometers to hundreds of nanometers (Figure 2.5 A and B). After acid treatment, cationized chitin was still present as micron-sized particles, but the fraction of nanofibers with diameters of less than 50 nm increased (Figure 2.5 C and D), which resulted from the fibrillation of fibers with larger diameters. The disintegration of large fibers occurred as a result of mechanical shearing during magnetic stirring and electrostatic repulsion between fibers due to $–NH_2$ protonation on the chitin surface. As shown in Figure 2.5 E and F, well-dispersed CNFs were produced after high pressure homogenization of the cationized chitin dispersion. These nanofibers have an average diameter (d_{avg}) of 20 nm, mainly ranging from 5 to 50 nm and lengths that vary between hundreds of nanometers to several micrometers. Chitin has very strong intra- and inter-hydrogen bonding [8, 9]. This not only leads to its insolubility in common solvents, but also hinders the defibrillation of large chitin fibers. Previously, Fan et al. successfully prepared individualized CNFs from squid pen using an high-power ultrasonication technique, but they were not able to produce CNFs from crab α-chitin by this method even though α-chitin was treated under acid condition (pH ~4) for chitin cationization. They argued that non-fibrillation of α-chitin may result from its higher crystallinity index, anti-parallel configuration and greater intermolecular forces in comparison to β-chitin [15]. The formation of CNFs with great dispersion by the high pressure homogenization of crab α-chitin indicates that the strong molecular interactions between chitin can be effectively broken with the combination of the high mechanical shearing induced by the

homogenizer and electrostatic repulsion between chitin nanofibers. As shown before, cationized chitin shows poor transparency while homogenized chitin is very transparent. We argue that the different appearances are related to the size of particles in dispersion, since it is expected that the large chitin particles in the cationized dispersion would lead to strong light scattering. It is noteworthy to mention that CNF dispersion in Figure 2.4 B and C flows easily under gravity, and shows high transparency and excellent stability without apparent agglomeration over one year. This stability indicates that although the percentage of amino groups in chitin was very low (DA: 92.4%), these positively charged $-NH_3^+$ on CNFs at pH ~ 4.1 were still quite effective in preventing CNFs from agglomeration.

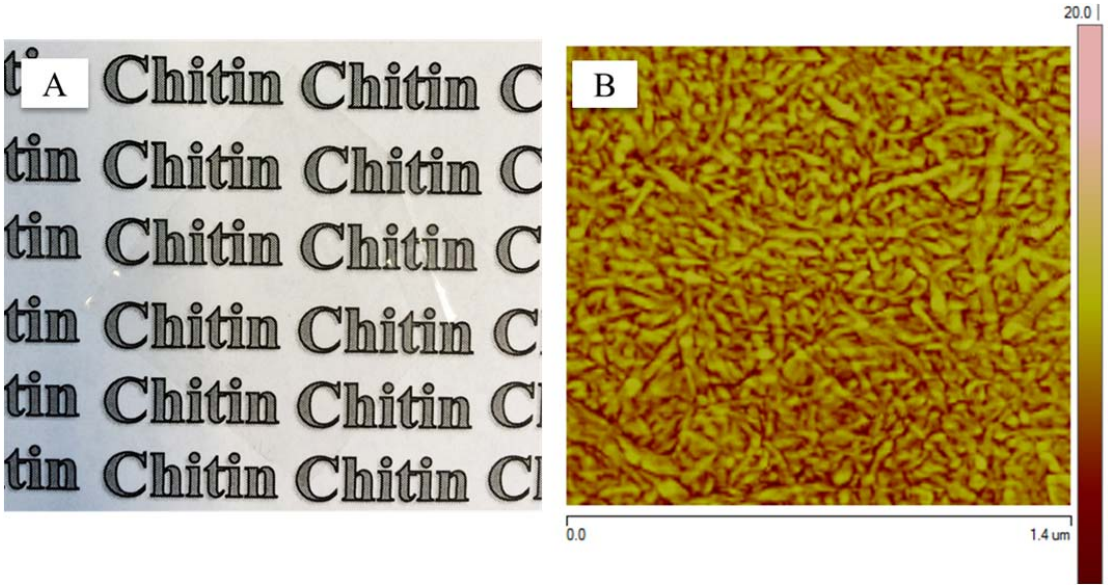

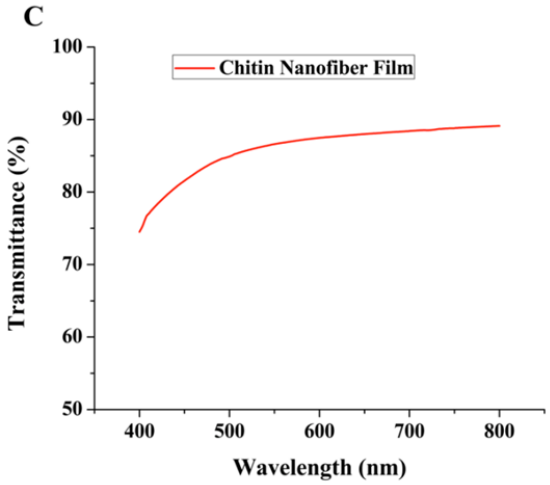

Figure 2.6 (A) Appearance of optically transparent CNF film; (B) AFM image of CNF film obtained from the tapping mode in air at room temperature; (C) Light transmittance spectra of CNF film in the range of 400 to 800 nm wavelengths.

When allowed to dry at room temperature, the CNF dispersion formed an optically transparent film that is composed of relatively densely packed nanofibers (Figure 2.6 A and B).The mean (Ra) and root-mean-square (rms) surface roughness of the CNF film were 3.0 ± 0.7 nm and 2.3 ± 0.5 nm, respectively, obtained from topography scans of ten random 200 nm × 200 nm areas on the film. The film has a transmittance of 89% at 800 nm (Figure 2.6 C) and the high transparency is attributed to low light scattering and adsorption of nanosized CNFs.

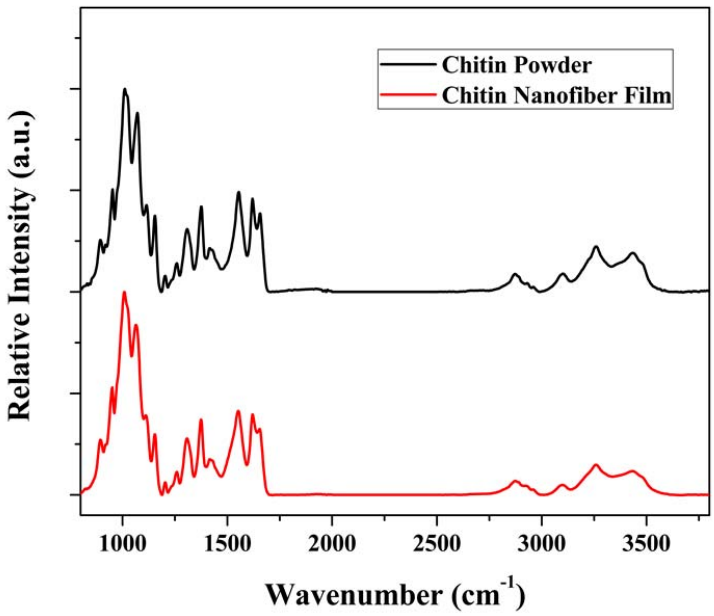

Figure 2.7 ATR spectra of purified chitin powder and CNF film.

Table 2.1 Adsorption bands of the purified chitin and CNF film, and their corresponding assignments [23].

Adsorption band (cm^{-1}) (chitin powder)	Adsorption band (cm^{-1}) (CNF film)	Assignment
3478	3478	O(6)-H···O(3) stretch (intramolecular hydrogen bonding)
3434	3434	O(3)-H···O(5) stretch (intramolecular hydrogen bonding)
3260	3260	N-H stretch (asymmetric) and O(6)-H···O(6) stretch (intermolecular hydrogen bonding)
3098	3098	N-H stretch (symmetric)
2960	2960	CH_3 stretch (asymmetric)
2932	2932	CH_2 stretch (symmetric)

2873, 2888	2873, 2888	C-H stretch
1654,1620	1654, 1620	C=O stretch (Amide I, N-H···O(7')=C and O(6)-H···O(7')=C bifurcate intermolecular hydrogen bonding)
1554	1554	C(2)-N stretch and N-H deformation in the CONH plane (Amide II)
1417	1417	C-H deformation (asymmetric)
1375	1375	C-H bending and CH_3 deformation (symmetric)
1307	1307	C(2)-N stretch and N-H deformation (Amide III), CH2 wagging
1259	1259	N-H deformation (Amide IV)
1203	1203	O-H in-plane bending and C-O stretch (symmetric)
1156	1156	C(1)-O-C(4) stretch (bridge oxygen of glycosidic linkage, asymmetric)
1113	1113	C(1)-O-C(5) stretch (in-plane glucose ring, asymmetric)
1065	1065	C(3)-OH stretch
1013	1013	C(6)-OH stretch
951	951	CH_3 wagging
895	895	C(1)-H out-of-plane bending (Glucose ring, β bond)
748	748	CH_2 rocking
700	700	N-H out of plane bending (Amide V)

Figure 2.7 shows the normalized ATR spectra of the purified chitin powders and CNF film dried from CNF dispersion at room temperature. The characteristic peaks of chitin such as amide band I at 1654 and 1620 cm^{-1}, amide band II at 1554 cm^{-1}, OH

stretching band at 3478 cm^{-1} and NH stretching at 3260 and 3098 cm^{-1} are observed from both of these spectra. In addition, these two spectra are quite similar and do not show any differences in the number of peaks and peak positions (Table 2.1). This indicates that original chemical structures of chitin were well maintained after the high pressure homogenization.

2.4.2 Crystal Structure of Chitin Powders and CNF Film

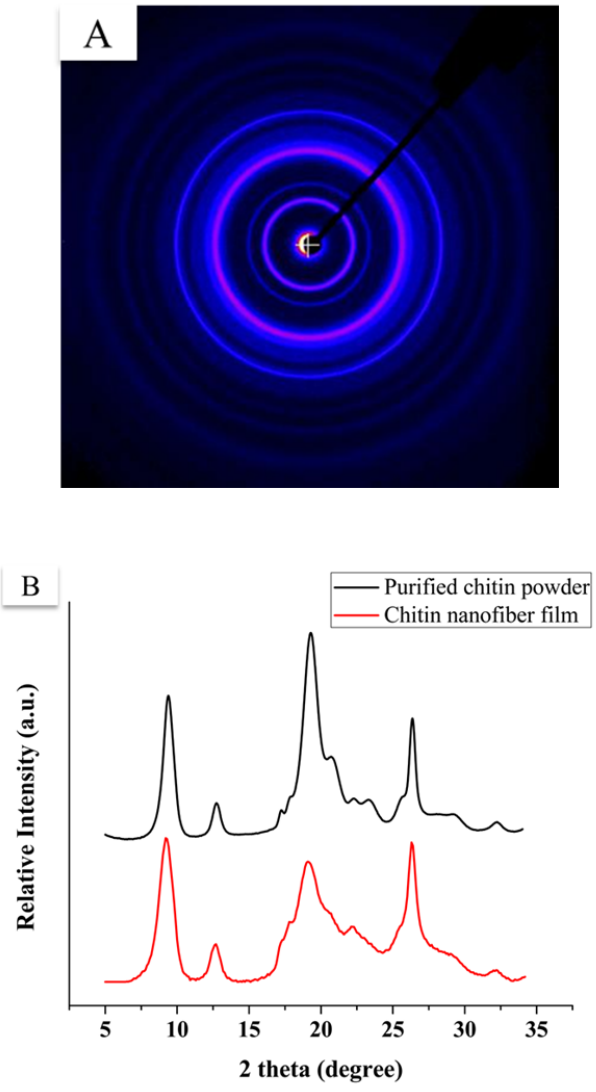

Figure 2.8 (A) 2-D XRD pattern of purified chitin powder; (B) Integrated 1-D XRD curves of purified chitin powder and CNF film.

XRD analysis of the purified chitin and CNFs was carried out to investigate the effect of the high pressure homogenization on the crystalline structure. As shown in Figure 2.8, both chitin-based materials have diffraction peaks at 9.3˚ 12.7˚, 19.3˚, 20.7˚, and 26.2˚, corresponding to the planes of (020), (101), (110), (120) and (013) [8, 9, 21].

2.4.3 Dynamic Rheology of CNF Dispersion

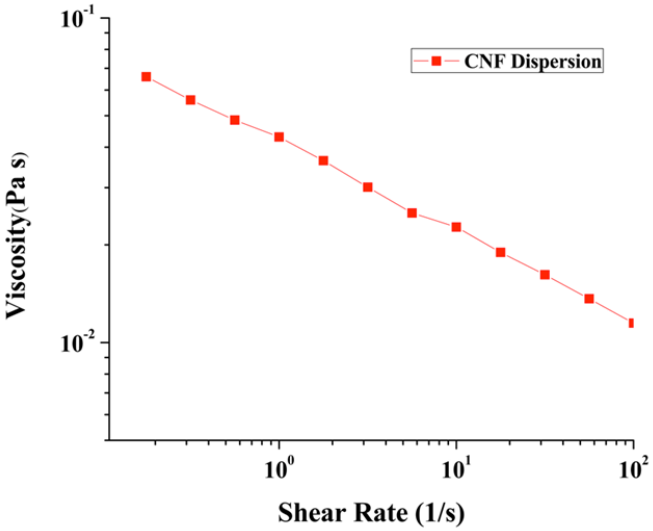

Figure 2.9 Shear viscosity as a function of shear rate for CNF dispersion with pH of ~ 4.1.

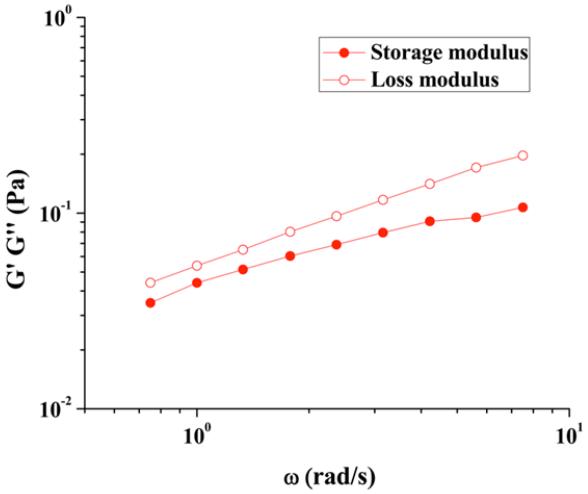

Figure 2.10 The storage modulus (G') and loss modulus (G'') as a function of frequency for CNF dispersion with pH of ~ 4.1.

The shear viscosities of CNF dispersions were studied as a function of shear rate. As shown in Figure 2.9, the dispersion in water of pH ~ 4.1 shows shear thinning behavior, that is, a decrease of viscosity with increasing shear rate. In addition to CNF dispersion, the shear thinning of chitin nanocrystals, cellulose nanocrystals and cellulose nanofibers have also been reported previously [24-29]. The viscosity of the CNF dispersion at a shear rate of 1 1/s is ~0.04 Pa·s, while cellulose nanofiber gel (0.5%) has a viscosity of ~1 Pa·s at the same shear rate, which is ~25 times greater than that of the CNF dispersion. When G'>> G'', the solution shows a strong gel-like behavior. However, G' and G'' of the CNF dispersion are quite close, such as 0.044 Pa for storage modulus and 0.054 Pa for loss modulus at 1 rad/s (Figure 2.10). In contrast, cellulose nanofiber dispersion has a storage modulus of ~10 Pa and a loss modulus of ~ 1 Pa at the same frequency [29]. Thus, the CNFs did not form strong network structures in water on the basis of its dynamic rheology data.

2.4.4 Thermal Properties of Chitin Powders and CNF Film

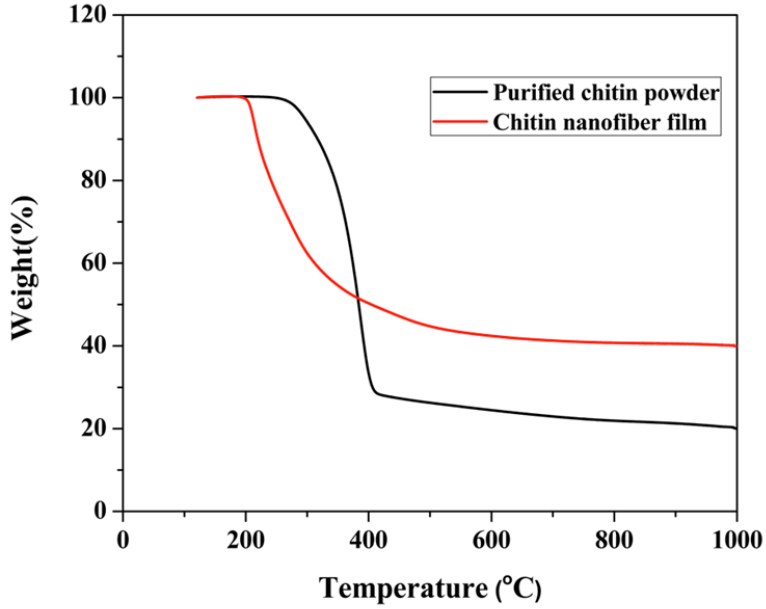

Figure 2.11 TGA curves of purified chitin powder and CNF film.

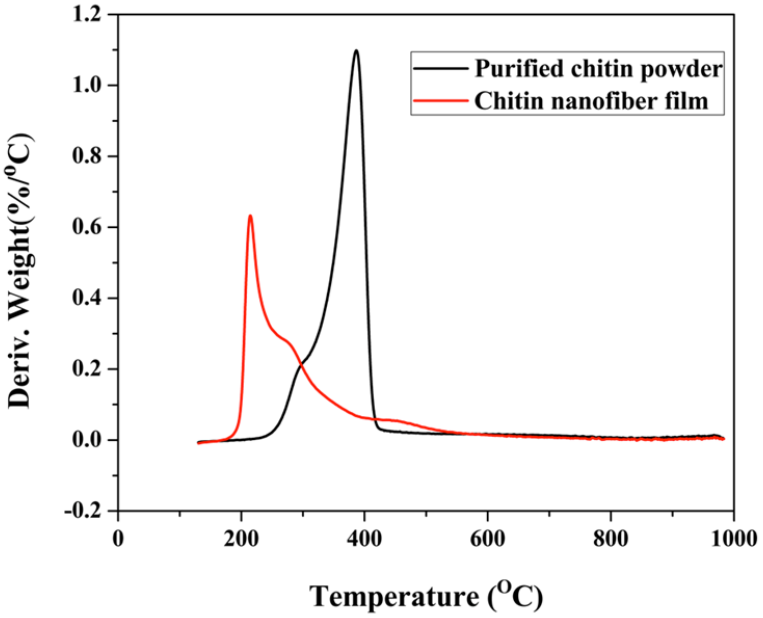

Figure 2.12 DTGA curves of purified chitin powder and CNF film.

Table 2.2 Thermal properties of the purified chitin and CNF film.

Sample	Onset temperature (˚C)	Tmax (˚C)	Residue percentage (1000 ˚C)
Chitin powder	277.4	386.6	20%
CNF film	204.1	214.4	40%

TG analysis of chitin powder and CNF film was conducted in a nitrogen atmosphere up to 1000 ˚C. According to the first two steps of their heating protocol, the amount of adsorbed water of these chitin materials was calculated to be ~3% and ~7%, respectively. Figure 2.11 shows the TGA curves normalized by removing the adsorbed water so that the residual mass was kept at 100% before 120 ˚C. Chitin powders began to degrade at 277.4 ˚C, and their maximum degradation temperature (T_{max}) is at 386.6 ˚C, as shown in Figure 2.11, 2.12 and Table 2.2. In contrast, the onset temperature of CNFs is 204.1 ˚C, and their T_{max} was observed at 214.4 ˚C. Chitin powders show higher onset degradation temperature than CNFs. These two kinds of chitin materials did not show any chemical structure differences according to ATR data in Figure 2.7, but they did have different morphologies (Figure 2.5 A, B and 2.6 B). Surprisingly, the CNFs still have a residue amount of 40% even when they were heated up to 1000 ˚C, which is twice residues of chitin powders at 1000 ˚C (Table 2.2). The thermal degradation of chitin is very complicated, which includes breaking, splitting of fragments of the main chain or side groups and release of volatile products [30, 31]. It is still unknown what caused the significantly different degradation properties between chitin powder and CNF film.

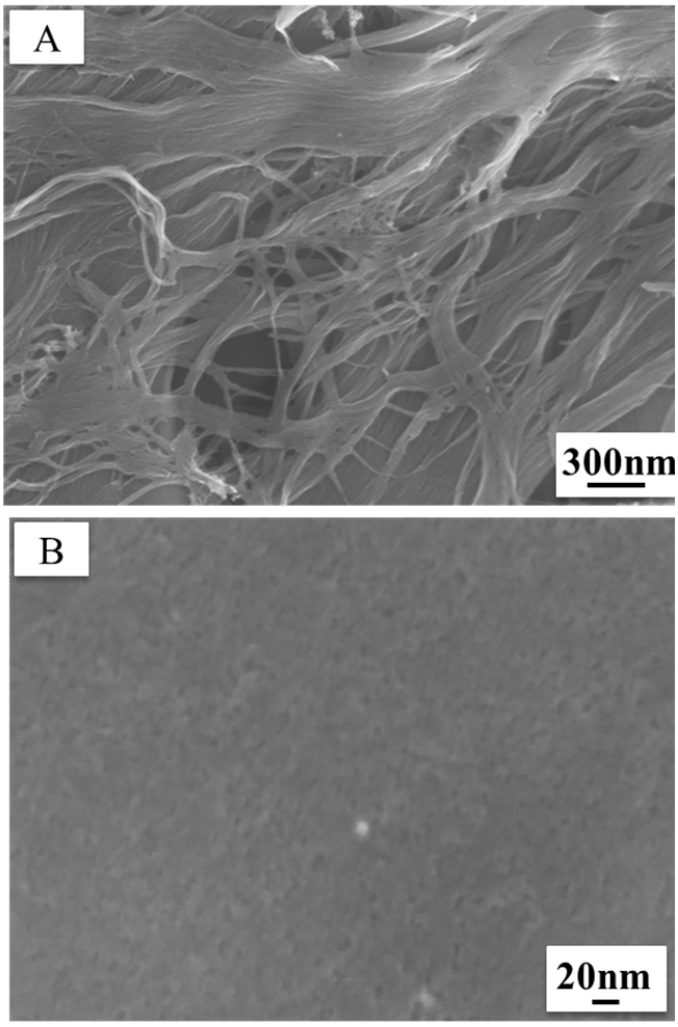

Figure 2.13 SEM images of pyrolyzed chitin powder and CNF film. These chitin materials were heated up to 600 ˚C under nitrogen atmosphere. The heating protocol is as follows: 1. heated from room temperature to 120 ˚C at a ramp rate of 10 ˚C/min; 2. held at 120 ˚C for 30 min; 3. heated from 120 ˚C to 600 ˚C at a ramp rate of 10 ˚C /min; 4. Cooled down to room temperature.

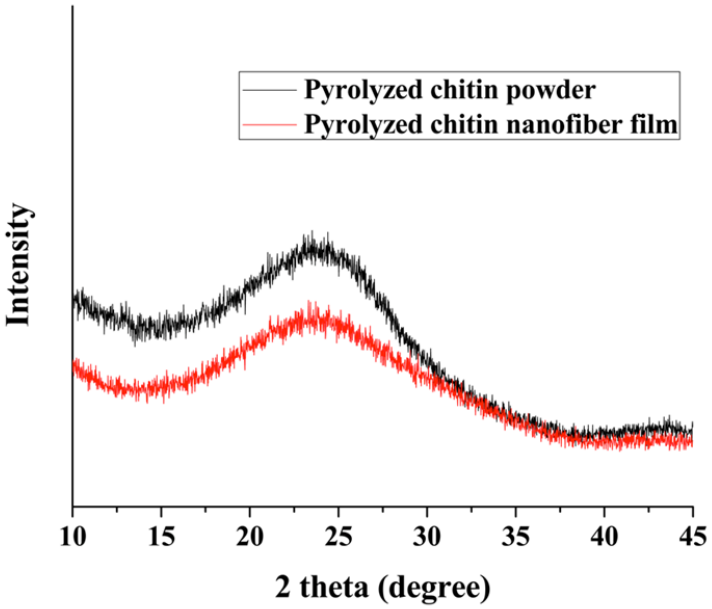

Figure 2.14 XRD patterns of 600 ˚C pyrolyzed chitin powder and CNF film.

Figure 2.13 illustrates the morphologies of pyrolyzed chitin materials. The pyrolyzed chitin powders still consist of fibers with diameters ranging from a few tens of nanometers to hundreds of nanometers, which is quite similar to the morphologies of non-pyrolyzed chitin powders. However, fibrous structures could not be observed from pyrolyzed CNF film, as opposed to nanofiber structure in pristine CNF in Figure 2.6 B. As shown in Figure 2.14, XRD patterns of pyrolyzed chitin materials have broad peaks, indicating that crystal structures of chitin were destroyed when they were heated up to 600 ˚C.

2.4.5 Barrier Properties of CNF Film

Table 2.3 Gas permeability of CNF film.

Gas	Kinetic diameter (Å) [32]	Permeability (barrer)
H_2	2.89	0.024
CO_2	3.30	0.018
O_2	3.46	0.006
N_2	3.64	0.0034
CH_4	3.80	0.0027

Note: 1 Barrer = 10^{-11} (cm^3 O_2) cm cm^{-2} s^{-1} $mmHg^{-1}$

All the gas permeability of CNF film ranged from 0.002 to 0.03 barrer, as shown in Table 2.3. Owing to its smallest kinetic diameter, H_2 had the highest gas permeability value in comparison to other gases (CO_2, O_2, N_2 and CH_4) [32]. Polyethylene terephthalate (PET), polyethylene (PE) and polypropylene (PP) are widely used commercial packaging materials, and they have oxygen permeabilities of 0.015-0.076, 0.75-3.04, and 0.75-1.52 barrer, respectively [33, 34]. Compared with these synthetic polymer films, the oxygen permeability of CNF film is much lower, only 0.006 barrer. This is attributed to high crystalline structure, abundant hydrogen bonding and stiff chain structure of the CNFs, which likely resulted in the low free volume and subsequently low oxygen permeability [35, 36].

2.5 Conclusions

In summary, CNFs were successfully extracted from crab α-chitin by a high pressure homogenization process. The resulting CNF has an average diameter of 20 nm and has a high zeta potential at pH ~ 4.1, which arises from protonated $–NH_3+$ groups that stabilizes the dispersion via electrostatic repulsion. In contrast to the formation of

strong CNF gels from mechanical grinding and high-power ultrasonication processes (aqueous solution pH is ~4) [15-17], the homogenized CNFs are well dispersed in water without forming strong network structures, and the obtained CNF dispersion has very low viscosity and storage modulus. In comparison to the pristine chitin powder, the CNFs have a lower onset degradation temperature but have a higher residue amount when heated up to1000 ˚C. The dried CNF film exhibits high optical transparency and shows great gas barrier properties. The sustainably-sourced nanofibrous materials are potentially useful for a wide range of applications, including packaging, polymer composites, catalysis, electronics (energy storage, transistors etc.), sensors, and biomedical engineering [4-7, 35-40].

2.6 References

[1]. Sheldon, R. A. Green and Sustainable Manufacture of Chemicals from Biomass: State of the Art. *Green Chemistry* **2014**, 16, 950-963.

[2]. Serrano-Ruiz, J. C.; Luque, R.; Sepúlveda-Escribano, A. Transformations of Biomass-Derived Platform Molecules: from High Added-Value Chemicals to Fuels via Aqueous-Phase Processing. *Chemical Society Reviews* **2011**, 40, 5266-5281.

[3]. Irimia-Vladu, M. "Green" Electronics: Biodegradable and Biocompatible Materials and Devices for Sustainable Future. *Chemical Society Reviews* **2014**, 43, 588-610.

[4]. Zhu. H.; Fang, Z.; Preston, C.; Li, Y.; Hu, L. Transparent Paper: Fabrications, Properties, and Device Applications. *Energy and Environmental Science* **2014**, 7, 269-287.

[5]. Korhonen, J. T.; Hiekkataipale, P.; Malm, J.; Karppinen, M.; Ikkala, O.; Ras, R. H. A. Inorganic Hollow Nanotube Aerogels by Atomic Layer Deposition onto Native Nanocellulose Templates. *ACS Nano* **2011**, 5, 1967-1974.

[6]. Ng, R.; Zang, R.; Yang, K. K.; Liu, N.; Yang, S. T. Three-dimensional Fibrous Scaffolds with Microstructures and Nanotextures for Tissue Engineering. *RSC Advances* **2012**, 2, 10110-10124.

[7]. Capadona, J. R.; Van Den Berg, O.; Capadona, L. A.; Schroeter, M.; Rowan, S. J.; Tyler, D. J.; Weder, C. A Versatile Approach for the Processing of Polymer Nanocomposites with Self-assembled Nanofibre Templates. *Nature Nanotechnology*

2007, 2, 765-769.

[8]. Rinaudo, M. Main Properties and Current Applications of Some Polysaccharides as Biomaterials. *Polymer International* **2008**, 57, 397-430.

[9]. Rinaudo, M. Chitin and Chitosan: Properties and Applications. *Progress in Polymer Science* **2006**, 31, 603-632.

[10]. Pillai, C. K. S.; Paul, W.; Sharma, C. P. Chitin and Chitosan Polymers: Chemistry, Solubility and Fiber Formation. *Progress in Polymer Science* **2009**, 34, 641-678.

[11]. Nair, K. G.; Dufresne, A. Crab Shell Chitin Whisker Reinforced Natural Rubber Nanocomposites. 1. Processing and Swelling Behavior. *Biomacromolecules* **2003**, 4, 657-665.

[12]. Raabe, D.; Sachs, C.; Romano, P. The Crustacean Exoskeleton as an Example of a Structurally and Mechanically Graded Biological Nanocomposite Material. *Acta Materials* **2005**, 53, 4281-4292.

[13]. Min, B. M.; Lee, S. W.; Lim, J. N.; You, Y.; Lee, T. S.; Kang, P. H.; Park, W. H. Chitin and Chitosan Nanofibers: Electrospinning of Chitin and Deacetylation of Chitin Nanofibers. *Polymer* **2004**, 45, 7137-7142.

[14]. Hassanzadeh, P.; Kharaziha, M.; Nikkhah, M.; Shin, S. R.; Jin, J.; He, S.; Zhong, C.; Dokmeci, M. R.; Khademhosseini, A.; Rolandi, M. Chitin Nanofiber Micropatterned Flexible Substrates for Tissue Engineering. *Journal of Materials Chemistry B*, **2013**, 1, 4217-4224.

[15]. Fan, Y.; Saito, T.; Isogai, A. Preparation of Chitin Nanofibers from Squid Pen β-Chitin by Simple Mechanical Treatment under Acid Conditions. *Biomacromolecules* **2008**, 9, 1919-1923.

[16]. Ifuku, S.; Nogi, M.; Abe, K.; Yoshioka, M.; Morimoto, M.; Saimoto, H.; Yano, H. Preparation of Chitin Nanofibers with a Uniform Width as α-Chitin from Crab Shells. *Biomacromolecules* **2009**, 10, 1584-1588.

[17]. Ifuku, S.; Nogi, M.; Yoshioka, M.; Morimoto, M.; Yano, H.; Saimoto, H. Fibrillation of Dried Chitin into 10–20 nm Nanofibers by a Simple Grinding Method under Acidic Conditions. *Carbohydrate Polymers* **2010**, 81, 134-139.

[18]. Wu, J.; Meredith, J. C. Assembly of Chitin Nanofibers into Porous Biomimetic Structures via Freeze Drying. *ACS Macro Letters* **2014**, 3, 185-190.

[19]. Duarte, M. L.; Ferreira, M. C.; Marvão, M. R.; Rocha, J. Determination of the Degree of Acetylation of Chitin Materials by 13C CP/MAS NMR Spectroscopy. *International Journal of Biological Macromolecules* **2001**, 28, 359-363.

[20]. Kasaai, M. R. Determination of the Degree of N-Acetylation for Chitin and

Chitosan by Various NMR Spectroscopy Techniques: a Review. *Carbohydrate Polymers* **2010**, 79, 801-810.

[21]. Li, J.; Revol, J.F.; Marchessault, R. H. Effect of Degree of Deacetylation of Chitin on the Properties of Chitin Crystallites. *Journal of Applied Polymer Science* **1997**, 65, 373-380.

[22]. Rungta, M. Carbon Molecular Sieve Dense Film Membranes for Ethylene/Ethane Separations, 2012.

[23]. Lu, Y.; Sun, Q.; She, X.; Xia, Y.; Liu, Y.; Li, J.; Yang, D. Fabrication and Characterisation of α-Chitin Nanofibers and Highly Transparent Chitin Films by Pulsed Ultrasonication. *Carbohydrate Polymers* **2013**, 98, 1497-1504.

[24]. Li, J.; Revol, J.F.; Marchessault, R. H. Rheological Properties of Aqueous Suspensions of Chitin Crystallites. *Journal of Colloid and Interface Science* **1996**, 183, 365-373.

[25]. Tzoumaki, M. V.; Moschakis, T.; Biliaderis, C. G. Metastability of Nematic Gels Made of Aqueous Chitin Nanocrystal Dispersions. *Biomacromolecules* **2010**, 11, 175-181.

[26]. Fan, Y.; Fukuzumi, H.; Saito, T.; Isogai, A. Comparative Characterization of Aqueous Dispersions and Cast Films of Different Chitin Nanowhiskers/Nanofibers. *International Journal of Biological Macromolecules* **2012**, 50, 69-76.

[27]. Orts, W. J.; Godbout, L.; Marchessault, R. H.; Revol, J. F. Enhanced Ordering of Liquid Crystalline Suspensions of Cellulose Microfibrils: a Small Angle Neutron Scattering Study. *Macromolecules* **1998**, 31, 5717-5725.

[28]. Lima, M. M. S.; Borsali, R. Rodlike Cellulose Microcrystals: Structure, Properties, and Applications. *Macromolecular Rapid Communication* **2004**, 25, 771-787.

[29]. Pääkkö, M.; Ankerfors, M.; Kosonen, H.; Nykänen, A.; Ahola, S.; Österberg, M.; Ruokolainen, J.; Laine, J.; Larsson, P. T.; Ikkala, O.; Lindström, T. Enzymatic Hydrolysis Combined with Mechanical Shearing and High-Pressure Homogenization for Nanoscale Cellulose Fibrils and Strong Gels. *Biomacromolecules* **2007**, 8, 1934-1941.

[30]. Tang, W.; Wang, C.; Chen, D. Kinetic Studies on the Pyrolysis of Chitin and Chitosan. *Polymer Degradation and Stability* **2005**, 389-394.

[31]. Jazaeri, E.; Tsuzuki, T. Effect of Pyrolysis Conditions on the Properties of Carbonaceous Nanofibers Obtained from Freeze-Dried Cellulose Nanofibers. *Cellulose* **2013**, 20, 707-716.

[32]. Low, B. T.; Chung, T. S.; Chen, H.; Jean, Y.; Pramoda, K. P. Tuning the Free Volume Cavities of Polyimide Membranes via the Construction of Pseudo-Interpenetrating Networks for Enhanced Gas Separation Performance. *Macromolecules* **2009**, 42, 7042-7054.

[33]. Lange, J.; Wyser, Y. Recent Innovations in Barrier Technologies for Plastic Packaging–a Review. *Packaging Technology and Science* **2003**, 16, 149-158.

[34]. Duan, B.; Chang, C.; Ding, B.; Cai, J.; Xu, M.; Feng, S.; Ren, J.; Shi, X.; Du, Y.; Zhang, L. High Strength Films with Gas-Barrier Fabricated from Chitin Solution Dissolved at Low Temperature. *Journal of Materials Chemistry A* **2013**, 1, 1867-1874.

[35]. Miller, K. S.; Krochta, J. M. Oxygen and Aroma Barrier Properties of Edible Films: a Review. *Trends in Food Science and Technology* **1997**, 8, 228-237.

[36]. Lavoine, N.; Desloges, I.; Dufresne, A.; Bras, J. Microfibrillated Cellulose – Its Barrier Properties And Applications In Cellulosic Materials: A Review. *Carbohydrate Polymers* **2012**, 90, 735-764.

[37]. La Torre, A.; Gimenez-Lopez, M. d. C.; Fay, M. W.; Rance, G. A.; Solomonsz, W. A.; Chamberlain, T. W.; Brown, P. D.; Khlobystov, A. N. Assembly, Growth, and Catalytic Activity of Gold Nanoparticles in Hollow Carbon Nanofibers. *ACS Nano* **2012**, 6, 2000-2007.

[38]. Chen, L. F.; Zhang, X. D.; Liang, H. W.; Kong, M.; Guan, Q. F.; Chen, P.; Wu, Z. Y.; Yu, S. H. Synthesis of Nitrogen-Doped Porous Carbon Nanofibers as an Efficient Electrode Material for Supercapacitors. *ACS Nano* **2012**, 6, 7092-7102.

[39]. Qie, L.; Chen, W. M.; Wang, Z. H.; Shao, Q. G.; Li, X.; Yuan, L. X.; Hu, X. L.; Zhang, W. X.; Huang, Y. H. Nitrogen-Doped Porous Carbon Nanofiber Webs as Anodes for Lithium Ion Batteries with a Superhigh Capacity and Rate Capability. *Advanced Materials* **2012**, 24, 2047-2050.

[40]. Suginta, W.; Khunkaewla, P.; Schulte, A. Electrochemical Biosensor Applications of Polysaccharides Chitin and Chitosan. *Chemical Reviews* **2013**, 113, 5458-5479.

CHAPTER 3

ASSEMBLY OF CHITIN NANOFIBERS INTO POROUS NANOFIBROUS STRUCTURES

3.1 Overview

The intricately hierarchical architectures in natural creatures are usually derived from assembly of molecular building blocks into nanoscale structures that then organize into micro- and macroscopic sizes. An example is the complex structure in arthropods (crustaceans, insects) constructed primarily by chitin. Because of chitin's inherent insolubility in common solvents, processes for mimicking the fascinating natural chitin-based nanostructures are still at an early stage of development. Here, we present a facile freeze drying approach to assemble chitin nanofibers (~20 nm diameter) into a variety of structures whose size and morphology are tunable by adjusting freezing temperature and heat transfer characteristics. We show that reducing freezing rate allows controllable formation of structures ranging from oriented sheets to three-dimensional aperiodic nanofiber networks that mimic the size and interconnectivity of the white *Cyphochilus* beetle cuticle. The formation of nanofibrous structures is not predicted by the widely-used particle encapsulation model of freeze-drying. We reason that this structure occurs due to a combination of attractive interactions of the nanofibers and a slow freezing rate that encapsulates and preserves the network structure. The method outlined here is likely applicable to creating fine nanofibrous structures with other polymers and materials classes with size ranges useful in diverse applications such as tissue engineering, filtration and energy storage.

3.2 Introduction

Natural creatures exhibit numerous intriguing properties derived from unique structures, such as the high adhesion of gecko feet, self-cleaning of lotus leaves, vivid colors of butterflies, and excellent toughness of nacre [1-4]. Inspired by these feats of nature, tremendous effort over several decades has been devoted to biomimicry. Significant progress has been achieved in fundamental understanding of natural structures and developing advanced synthetic materials based upon them, including novel high-performance adhesives, superhydrophobic coatings, displays, textiles, structural materials and biomaterials [5-10]. Biological inspiration is considered as an important route to revolutionize current methods in material design and synthesis [10]. Many of these mimicked structures offer pathways to produce materials from sustainable resources derived from plants and animals.

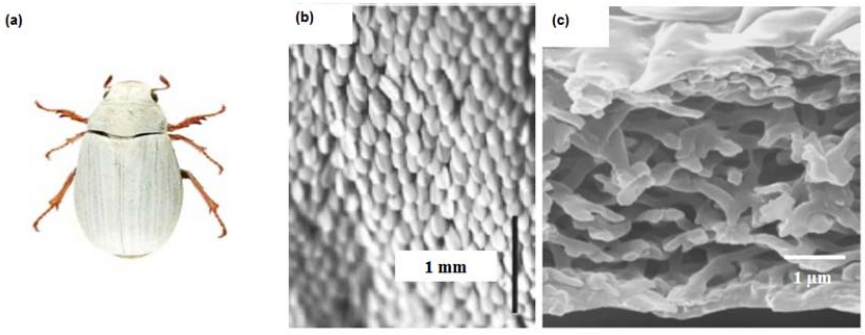

Figure 3.1 (A) Cyphochilus "White beetle"; (B) SEM image of white scales covering of Cyphochilus head, legs and body; (C) SEM image of interiors of white beetle covering [15].

Chitin is a renewable and biodegradable polymer that assembles into crystalline nanofibers that are utilized by animals (arthropods) and fungi through organization into many sophisticated hierarchical structures. Being the second-most abundant naturally produced biopolymer (second to cellulose), 10^{10} to 10^{11} tons of chitin is produced each

year in nature. However, chitin biomimicry remains a significant and unsolved challenge [11-13]. Chitin-based structures include the high-stiffness twisted plywood structure of lobster shells [14]. Another example is the *Cyphochilus* 'white' beetle, which has unique whiteness arising from the chitin-rich three-dimensional aperiodic network structure within its cuticle that is composed of fibrils around 250 nm in diameter and containing about 30% air void volume (Figure 3.1). This arrangement appears to optimize scattering efficiency by maximizing the scattering center number density while avoiding adverse optical crowding effects [15]. This kind of porous nanofibrous structure is significant to a wide range of practical applications, including white paints and coatings, tissue engineering, catalysis, sensors, filtration, absorbents, actuators, structural materials and energy storage (supercapacitors and batteries) [16-25]. Constructed primarily of chitin and some protein, the white beetle cuticle is a model for mimicry to produce such porous nanofibrous materials from a renewable resource.

However, owing to its insolubility in common solvents and strong molecular interactions, chitin is challenging to process into controlled nanostructures [11-13]. Previously, man-made processes have not been reported to use chitin directly to reproduce the intricate cuticle structure. While self-assembly and electrospinning are potential candidates, they have not been demonstrated on chitin nanofibers directly, but rather they often require structure-directing additives (self-assembly) or depolymerization and use toxic or volatile organic solvents (electrospinning). These alterations detract from the sustainable nature of chitin [26-28]. Often, chitin is deacetylated to form chitosan, which is soluble in dilute acidic solutions. The processing of chitosan into nanostructured materials has been the subject of numerous investigations [11, 12, 29, 30]. In contrast, we

seek a method to assemble extracted chitin directly into nanofibrous structures with controlled size and interconnectivity, without any other additives or pretreatments that alter the polymer structure.

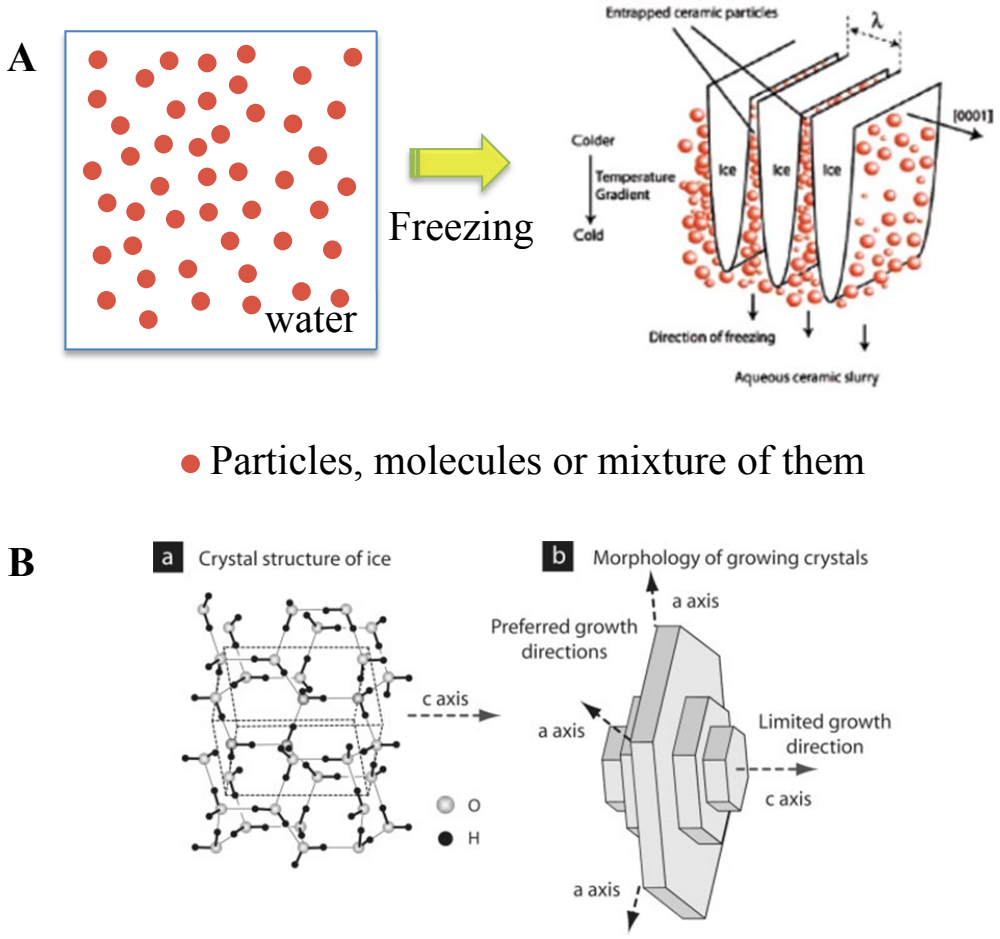

Figure 3.2 (A) Particles, molecules or mixture of them dispersed or dissolved in water (left); Ice crystals grew towards freezing direction and pushed the particles or molecules into the interstitials between them (right) [31]; (B) Crystal structure of ice and the anisotropy of crystal growth kinetics [35].

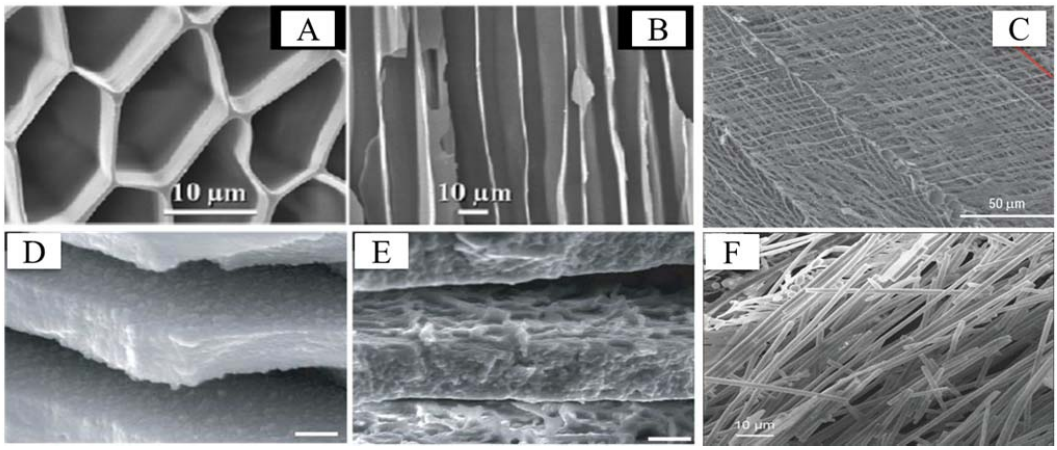

Figure 3.3 The morphologies of freeze-dried materials (A) Honeycomb; (B) Aligned sheet; (C) Double network; (D) and (E): Brick and mortar; (F) Fibrous structures [31-36].

Freeze drying has attracted intense interest as a general route to fabricate porous materials for a wide range of applications. Starting with a solution, emulsion, or dispersion, freezing causes solute or solids to be excluded by an advancing ice front into the interstitial spaces between ice crystals (Figure 3.2). Subsequent sublimation leads to porous structures. By controlling concentration and freezing direction, complex hierarchical morphologies are produced, including well-aligned channels, honeycombs, and brick-mortar-bridges [9, 31-36] (Figure 3.3). Most studies focus on directional freezing under liquid nitrogen, but non-directional, aperiodic nanofibrous structures similar to that of the white beetle have not been achieved by freeze drying.

In this chapter, we demonstrate that adjusting variables expected to control freezing rate (freezing temperature or heat transfer characteristics), allows tuning the *dimensions and connectivity* of the chitin structures formed from an aqueous chitin nanofiber (CNF) dispersion. Depending on freezing conditions, this method allows a broad variety of structures to be formed from chitin, from nanofibrous networks that

mimic the white beetle to micrometer-scale oriented and random sheets. The general principle of reducing ice growth rate to achieve finer control of porous network structures, applied here to chitin, is likely applicable to other polymer and materials classes to produce structures of relevance to many practical applications, as noted above [16-25].

3.3 Experimental Methods

3.3.1 Materials

Dried crab shell flakes were purchased from TCI America. Deionized water (18.2 MΩ cm) was prepared in a Barnstead Easypure RoDi purification system. Hydrochloric acid, sodium hydroxide, acetone and ethanol were purchased from EMD Chemical Inc.

3.3.2 Chitin Purification and Fibrillation

Dried crab shell flakes were processed to obtain purified chitin [13, 37]. Ground crab shells were refluxed in 5 wt % sodium hydroxide in DI water for 6 h to remove protein. The suspension was filtered and rinsed with DI water until the pH was 7. Next, the filtered solids were treated with 7% hydrochloric acid for 6 h at room temperature to remove minerals. After filtration and washing with DI water, the treated sample was refluxed in a 5% NaOH solution for 2 days to remove residual proteins and the other residues were eliminated by acetone and ethanol extraction. The purified chitin was dispersed in distilled water under an acidic condition and then this mixture was passed through a high-pressure homogenizer (Bee International Inc., MA USA) to generate CNFs (aqueous medium pH is around 4.1).

3.3.3 Formation of Porous Chitin Materials

The 0.5 wt % aqueous dispersions of CNFs (average diameter of 20 nm) were frozen at different conditions: -20 ˚C (freezer), -80 ˚C (freezer), -196 ˚C (liquid nitrogen) in aluminum dishes (length x width x height = 70x70x15 mm^3) and at -20 ˚C (freezer) using a stainless steel mold with overall dimensions 50x50x15 mm^3 with a 20x20x0.8 mm^3 indentation for holding the sample. After complete freezing, ice was sublimated under vacuum at -50 ˚C to produce porous chitin materials.

3.3.4 Materials Characterization

The surface charge of CNF at pH ~ 4.1 in water was measured by a Malvern Zetasizer Nano ZS 90. Field-Emission Scanning Electron Microscopy (Zeiss Ultra 60) was performed at 5 kV to characterize the morphologies of chitin-based materials. Before imaging, these samples were coated with a thin layer of gold/palladium (Hummer IV Sputtering System) to promote conductivity.

The porosities of freeze-dried chitin were determined using the following Equation 3.1 The density of porous chitin was calculated by dividing the mass by volume of samples cut into rectangular cubes with known dimensions (length x width =10x10 mm^2). The density of chitin is taken to be 1425 kg/m^3 [38].

$$\text{Porosity} = 1 - \frac{\rho_{\text{freeze–dried chitin}}}{\rho_{\text{Chitin}}} \qquad \text{Equation 3.1}$$

3.4 Results and Discussion

3.4.1 The Morphology of Room-temperature Dried CNF

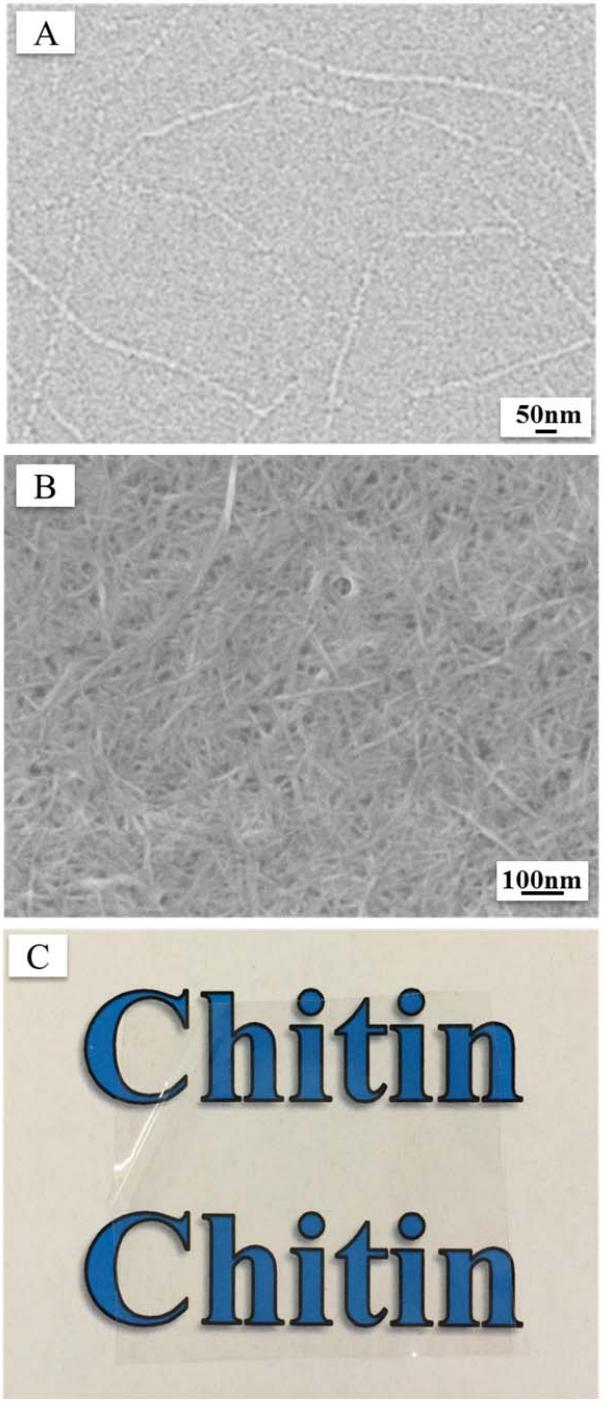

Figure 3.4 (A) SEM image of CNF fabricated via fibrillation of purified chitin by high pressure homogenization; (B) SEM image and (C) Photo of CNF film produced by drying CNF/water dispersion at room temperature.

CNFs were fabricated via fibrillation of purified chitin by high pressure homogenization, as described in the experimental section. After homogenization, the CNF dispersion exhibits high optical transparency and CNF has a zeta potential of +57.5 mv at pH ~ 4.1, which originates from protonated $–NH_3^+$ groups and stabilizes the dispersion via electrostatic repulsion. Figure 3.4A illustrates that single CNFs are present in water with an average diameter (d_{avg}) of 20 nm distributed over a range of 5 to 50 nm and lengths that vary between ~100 nm to several micrometers. When allowed to dry at room temperature, the CNF dispersion forms an optically transparent film that is composed of relatively densely packed nanofibers (Figure 3.4B and C). Dense structures like these are typically formed when fibrous materials are dried from water under ambient conditions, due to compaction and adhesion of fibers that occurs as solids concentration increases, and additionally due to pore shrinkage in late stages of drying due to the high surface tension of water.

3.4.2 The Morphologies of Freeze-dried Chitin Using Aluminum Substrate

Table 3.1 Porosity of freeze-dried chitin.

Temperature (˚C)	Mold	Porosity (%)
-20	Aluminum	98.5
-80	Aluminum	99.5
-196	Aluminum	99.5
-20	Stainless Steel	99.6

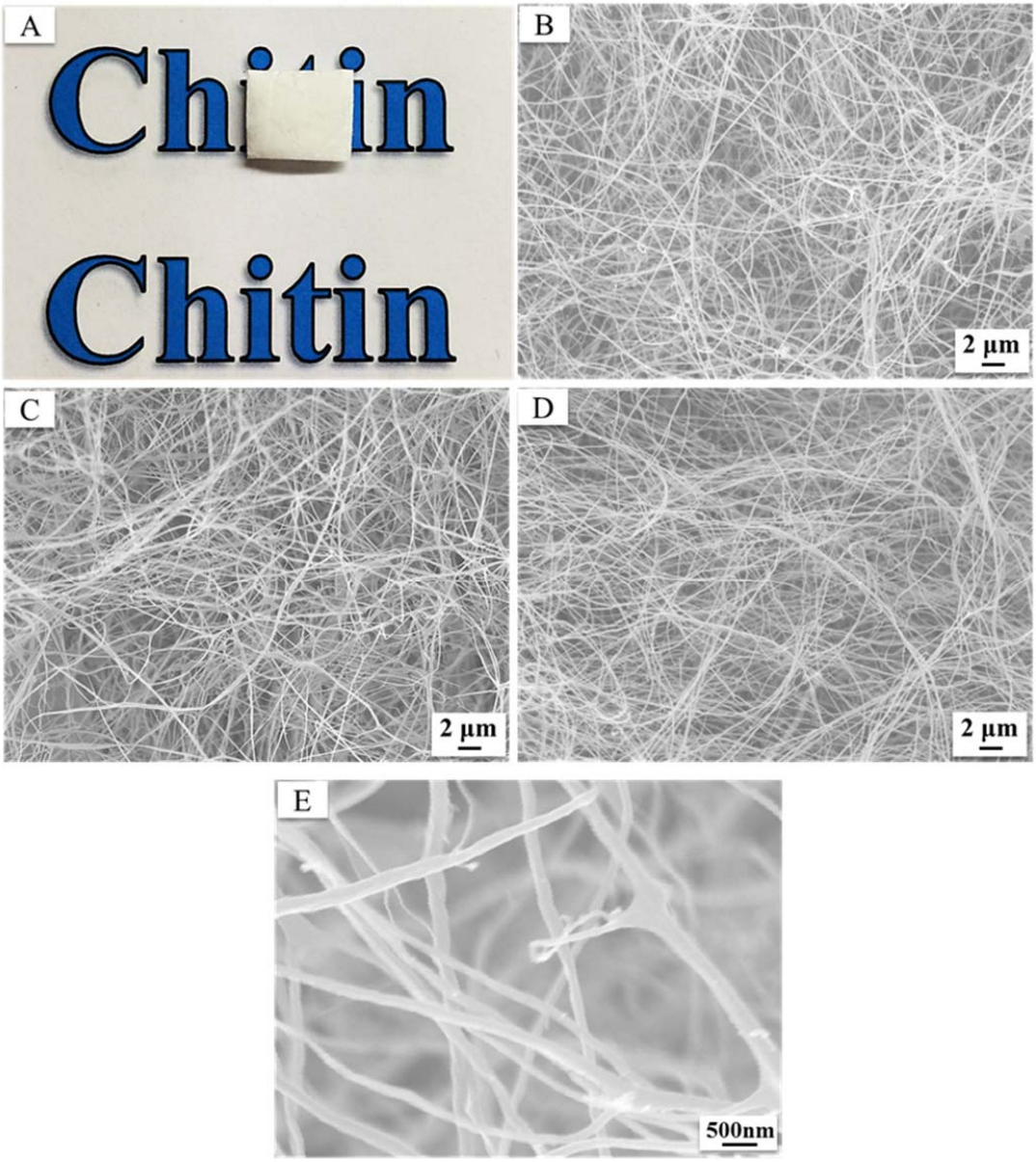

Figure 3.5 (A) Photo; (B) Top; (C) Bottom; (D) Cross section; (E) Enlarged top SEM images of freeze-dried chitin produced under -20 ˚C freezing (aluminum dish).

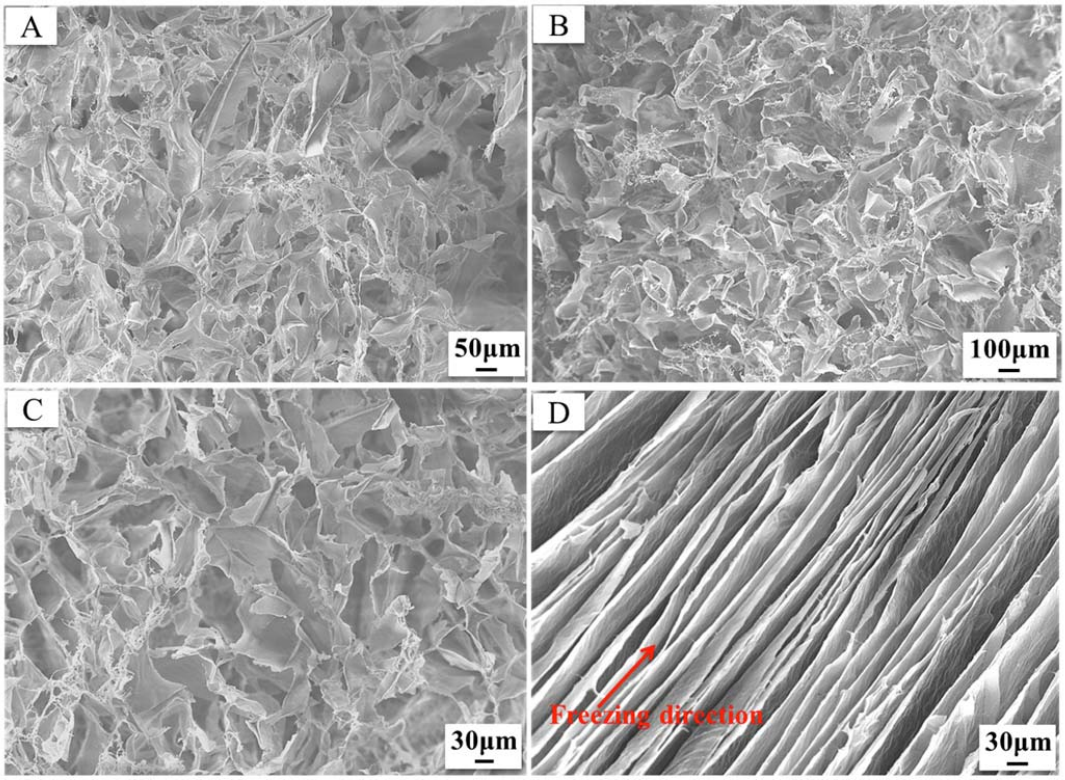

Figure 3.6 SEM images of freeze-dried chitin: (A) Top and B) Cross section of sample produced at -80 ˚C freezing; (C) Top and (D) Cross section of sample produced under liquid nitrogen freezing.

All freeze-dried structures were produced at -20 ˚C, -80 ˚C and -196 ˚C (liquid N_2), using a CNF aqueous suspension. The freeze-dried chitin prepared at -20 ˚C freezing temperature is white and opaque (Figure 3.5A), and consists of a three-dimensional aperiodic fibrous network structure with d_{avg} = 220 nm, ranging from 150 nm to 350 nm based on top, bottom and cross-sectional SEM images (Figure 3.5B-E). These results show that single CNFs assemble into larger, randomly oriented interconnected fibril bundles during freezing, very similar to the white beetle scale structure (fibrous network structure with fiber diameter of around 250 nm) [15]. While the fiber size and interconnectivity of freeze-dried chitin are similar to the white beetle structure, the

synthetic structures are much more porous (>90% in Table 3.1) than the beetle structure (~30%). CNF suspensions were also frozen at -80 ˚C and -196 ˚C (liquid nitrogen), but these conditions do not produce fibrous structures. At -80 ˚C, the frozen chitin has a random porous architecture (Figure 3.6A and B) consisting of sheet-like structures, while parallel-walled structures result from liquid nitrogen freezing (Figure 3.6D). Oriented and sheet-like porous structures, similar to those derived here at -80 ˚C and -196 ˚C, have been reported before by utilizing different starting materials and their structure formation mechanism has already been established [31-33, 39]. Reports of freeze drying chitosan (not chitin) at high temperature (-20 ˚C) have demonstrated macroporous sheet-like structures [29, 30], but not fine nanofibrous structures created herein with chitin. As discussed below, we propose that the solubility of chitosan likely leads to precipitation into large domains during freezing, whereas starting with insoluble CNFs leads to a preservation of the nanoscale features.

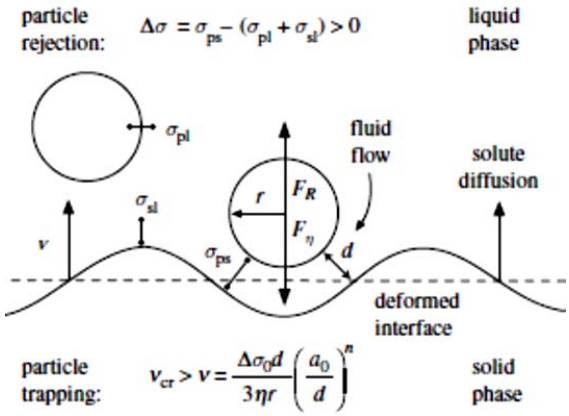

Figure 3.7 Schematic of particle-advancing ice front interactions. A liquid film with a thickness of d separates a particle with a radius of r from the advancing ice fronts [44].

Ice crystallization is well-characterized and consists of two successive processes: crystal nucleation and growth. The rate of ice nucleation is determined by the degree of supercooling whereas the ice growth rate is largely controlled by the rate of heat transfer from the crystal surface to the bulk water [40-42]. A suspended particle close to an advancing ice front is acted on by two opposing forces: a repulsive force derived from van der Waals forces (F_R) and an attractive force owing to viscous drag (F_η). A balance of these two forces yields a critical ice growth velocity (V_{cr}) at which particle encapsulation by the ice occurs (Figure 3.7). Below this velocity, particles repelled by ice should be pushed together into the interstitial spaces between ice crystals, e.g., formed structures are larger than the original particles. Above this critical velocity the structures are encapsulated as ice grows around the particles [34, 43, 44]. The formation of large porous structures at -80 ˚C and -196 ˚C (Figure 3.6), starting with 20 nm CNFs, indicates that ice front velocity was below the critical encapsulation velocity. At -196 ˚C, the CNF suspension is subject to a significant temperature gradient in the thickness direction, leading to fast ice crystallization in this direction to the orthogonal, leading to oriented porous structures (Figure 3.6C and D). Under -80 ˚C freezing, there was no preferred growth direction, likely due to the reduced temperature gradient, and CNFs were expelled by ice fronts to form large, disoriented sheet-like structures.

3.4.3 Porous Structure Formation Mechanism of Freeze-dried Materials

Ice growth rate should be slower at -20˚C than at -80 ˚C or -196 ˚C based on the reduced driving force for heat removal [41, 45]. Thus the ice growth velocity at -20 ˚C will be even further below the critical velocity for encapsulation of CNFs than at -80 ˚C. Hence, we expect that ice crystal size at -20 ˚C should be larger than that at -80 ˚C

because slower freezing rate generally results in larger ice crystals [35, 42, 46, 47]. However, the pore size of freeze-dried chitin observed from Figure 3.5B-E and Figure 3.6A and B is *smaller* at -20 ˚C than at -80 ˚C, which indicates that they are not controlled by ice crystal size. This implies that CNFs are encapsulated and are not pushed to interstitial boundaries. Hence, the observation of smaller pore size at -20 ˚C contradicts the prediction of the particle encapsulation model. We suggest that this discrepancy is due to the fact that CNFs do not behave as independent particles, but experience significant interactions. For example, chitin nanocrystals exhibit strong van der Waals attraction and electrostatic interactions and are known to form nematic gels with increasing concentration in water [48].

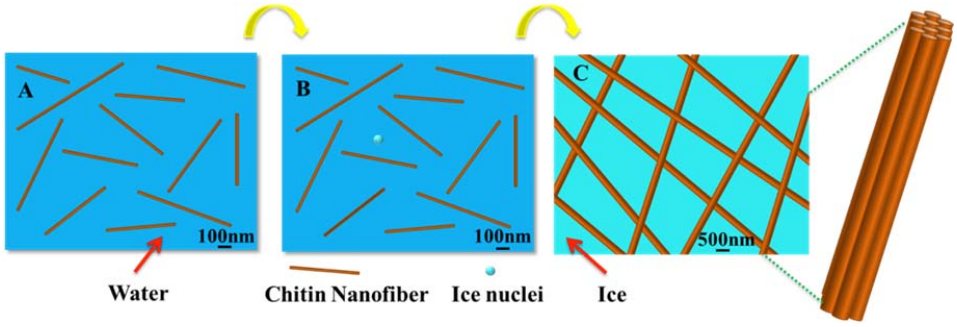

Figure 3.8 Schematic representation of assembly of CNFs under -20 ˚C freezing using aluminum dish: (A) CNF/water dispersion; (B) CNF/water dispersion with advent of ice nuclei; (C) CNF bundles encapsulated in ice.

The proposed mechanism for formation of fibrous network structures under -20 ˚C freezing is illustrated in Figure 3.8. First, CNFs are well dispersed in water at pH 4 due to strong electrostatic repulsion. When the CNF suspension is supercooled sufficiently, ice starts to nucleate and grow. Initially, isolated CNFs are pushed together by the advancing ice fronts, leading to fiber-fiber interactions such as van der Waals attraction, electrostatic repulsion, and hydrogen bonding. At this stage we propose that

individual CNFs assemble into interconnected nanofiber bundles between 150-350 nm in diameter. As ice continues to grow slowly, these bundles do not become oriented, but rather form a three-dimensional aperiodic network structure with fiber diameters averaging about 220 nm. This network structure can apparently resist being broken by the advancing ice fronts, and the growing ice crystals pass around and encapsulate this network instead. Since the ice growth rate is expected to be relatively slower at -20 ˚C than at -80 ˚C, we argue that single CNFs have more time to reorient and align into packed bundles at -20 ˚C, whereas the advancing ice front more quickly expels CNFs and then ruptures the developed network structure under -80 ˚C and -196 ˚C freezing to form sheet-like structures (faster aggregation). A previous report showed that chitosan dissolved in acetic acid formed large macroporous sheet structures under -20 ˚C freezing [30]. Because chitosan was dissolved, fibers were not initially present to form a network in the early stages of freezing. Rather, the chitosan formed phase-separated micron-sized structures as solution concentration increased in the interstitial spaces. Hence, formation of the fine network structure likely depends on the initial presence of fine insoluble chitin fibers.

3.4.4 The Morphologies of Freeze-dried Chitin Using Steel Substrate

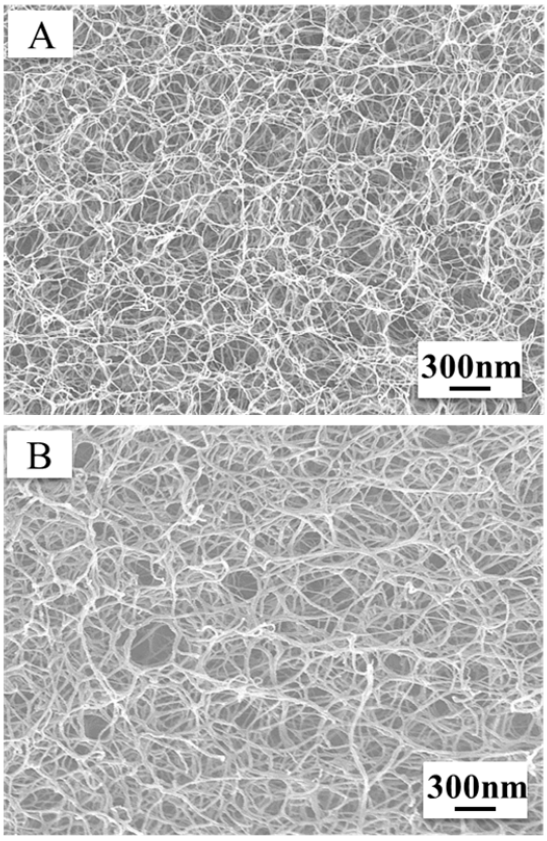

Figure 3.9 SEM images of chitin freeze-dried using indented stainless-steel mold: (A) Bottom; (B) Cross section in touch with stainless steel wall of freeze-dried chitin under -20 ˚C freezing (stainless-steel mold).

Above, we have shown that tuning freezing temperature results in adjustable pore structure and have argued that this is the result of adjustments in the ice crystallization rate. Hence, tailoring the geometry and material of the freezing substrate to achieve finer control of cooling rate may allow further opportunities to tune the freeze-dried structure. To investigate this, the CNF/water suspension was frozen at -20 ˚C using an indented stainless-steel mold that is considerably thicker than the aluminum dishes used above. In Figure 3.9A and 3.9B, we observe that the resulting freeze-dried chitin is comprised of a fibrous network structure and filament diameter near 40 nm, much smaller than the

dimensions of chitin frozen in the aluminum dish at -20 ˚C. The porosity of the structures produced at -20 °C in the stainless-steel mold was 99.6%, compared to 98.5 % for the aluminum dish, which is consistent with the finer structures observed in the stainless-steel system. Supercritical drying and organic solvent-based freeze drying have been shown to produce such finely porous materials previously [23, 49], but it is very rare that this fine structure can be achieved directly by water-based freeze drying, because ice fronts usually advance so quickly that solute or dispersed solids are expelled to form large aggregates. Compared with -20 ˚C freezing in the aluminum pans, we expect a slowing in ice growth rate in the steel mold due to lower heat transfer rate. The conductive resistance of the steel substrate wall is about 1000 times larger than that of the aluminum substrate ($R_{alum}= \Delta x/k_{alum}$=0.2 mm/229 W·(m·K)$^{-1}$=8.7x10^{-7} (m^2·K)/W versus $R_{steel}= \Delta x/k_{steel}$=14.2 mm/16 W·(m·K)$^{-1}$=8.9 x10^{-4} (m^2·K)/W, where Δx=thickness and k=thermal conductivity) [50]. The further decrease in the fiber size and pore size is consistent with the model proposed above, since the slower moving ice front (steel substrate) exerts less shearing force on the CNF network structure (compared to aluminum substrate), allowing preservation of finer structures that form early in the CNF aggregation process.

3.5 Conclusions

In summary, we have produced the first porous nanofibrous materials derived solely from chitin nanofibers by using a facile freeze drying method. These structures mimic the size and interconnectivity of the white *Cyphochilus* beetle cuticle, but with improved porosity well-beyond that of the natural structure (30% to >95%). The formation of such fine nanofibrous structures is not predicted by the widely-used particle

encapsulation model, and has not been demonstrated previously using freeze-drying. We reason that the nanofibrous network structure is made possible because chitin nanofibers are insoluble and they experience significant attractive interactions, and combined with a slow freezing rate, the network structure remains intact during freezing. We have shown that versatile porous structures can be achieved by simply adjusting freezing temperature or system geometry. Previously, supercritical drying and organic solvent-based freeze drying have been used to generate delicately porous fibrous materials because water-based freeze drying usually results in significant aggregations of original building blocks. In contrast, our findings show how to achieve such fine structures by more facile water-based freeze drying. The innovative, sustainably-sourced chitin materials are of ideal size range to be useful in a wide variety of applications, including as components of thermal insulation, reflective energy-efficient exterior coatings, reinforcing phase for polymer composites and as a basic template for sensors, tissue scaffolds, catalyst supports, filtration, absorbents and energy storage materials [16-25, 51]. The freeze drying method outlined here should be applicable to tunable assembly of nanofibrous structures from other network-forming water-dispersible polymers and other materials.

3.6 References

[1]. Autumn, K.; Liang, Y. A.; Hsieh, S. T.; Zesch, W.; Chan, W. P.; Kenny, T. W.; Fearing, R.; Full, R. J. Adhesive Force of A Single Gecko Foot-hair. *Nature* **2000**, 405, 681-685.

[2]. Feng, L.; Li, S. H.; Li, Y. S.; Li, H. J.; Zhang, L. J.; Zhai, J.; Song, Y. L.; Liu, B. Q.; Jiang, L.; Zhu, D. B. Super-hydrophobic Surfaces: From Natural to Artificial. *Advanced Materials* **2002**, 14, 1857-1860.

[3]. Srinivasarao, M. Nano-optics in the Biological World: Beetles, Butterflies, Birds, and Moths. *Chemical Reviews* **1999**, 99, 1935-1961.

[4]. Meyers, M. A.; Chen, P. Y.; Lin, A. Y. M.; Seki, Y. Biological Materials: Structure and Mechanical Properties. *Progress in Materials Science* **2008**, 53, 1-206.

[5]. Boesel, L. F.; Greiner, C.; Arzt, E.; del Campo, A. Gecko-Inspired Surfaces: A Path to Strong and Reversible Dry Adhesives. *Advanced Materials* **2010**, 22, 2125-2137.

[6]. Jiang, L.; Zhao, Y.; Zhai, J. A Lotus-leaf-like Superhydrophobic Surface: A Porous Microsphere/Nanofiber Composite Film Prepared by Electrohydrodynamics. *Angewandte Chemie International Edition* **2004**, 43, 4338-4341.

[7]. Walish, J. J.; Kang, Y.; Mickiewicz, R. A.; Thomas, E. L. Bioinspired Electrochemically Tunable Block Copolymer Full Color Pixels. *Advanced Materials* **2009**, 21, 3078-3081.

[8]. Rawlings, A. E.; Bramble, J. P.; Staniland, S. S. Innovation through Imitation: Biomimetic, Bioinspired and Biokleptic Research. *Soft Matter* **2012**, 8, 6675-6679.

[9]. Munch, E.; Launey, M. E.; Alsem, D. H.; Saiz, E.; Tomsia, A. P.; Ritchie, R. O. Tough, Bio-Inspired Hybrid Materials. *Science* **2008**, 322, 1516-1520.

[10]. Huebsch, N.; Mooney, D. J. Inspiration and Application in the Evolution of Biomaterials. *Nature* **2009**, 462, 426-432.

[11]. Rinaudo, M. Chitin and Chitosan: Properties and Applications. *Progress in Polymer Science* **2006**, 31, 603-632.

[12]. Pillai, C. K. S.; Paul, W.; Sharma, C. P. Chitin and Chitosan Polymers: Chemistry, Solubility and Fiber Formation. *Progress in Polymer Science* **2009**, 34, 641-678.

[13]. Nair, K. G.; Dufresne, A. Crab Shell Chitin Whisker Reinforced Natural Rubber Nanocomposites. 1. Processing and Swelling Behavior. *Biomacromolecules* **2003**, 4, 657-665.

[14]. Raabe, D.; Sachs, C.; Romano, P. The Crustacean Exoskeleton as An Example of A Structurally and Mechanically Graded Biological Nanocomposite Material. *Acta Materials* **2005**, 53, 4281-4292.

[15]. Vukusic, P.; Hallam, B.; Noyes, J. Brilliant Whiteness in Ultrathin Beetle Scales. *Science* **2007**, 315, 348-348.

[16]. Ye, C.; Li, M.; Hu, J.; Cheng, Q.; Jiang, L.; Song, Y. Highly Reflective Superhydrophobic White Coating Inspired by Poplar Leaf Hairs Toward An Effective "Cool Roof". *Energy Environmental and Science* **2011**, 4, 3364-3367.

[17]. Ng, R.; Zang, R.; Yang, K. K.; Liu, N.; Yang, S. T. Three-dimensional Fibrous Scaffolds with Microstructures and Nanotextures for Tissue Engineering. *RSC Advances* **2012**, 2, 10110-10124.

[18]. La Torre, A.; Gimenez-Lopez, M. d. C.; Fay, M. W.; Rance, G. A.; Solomonsz, W. A.; Chamberlain, T. W.; Brown, P. D.; Khlobystov, A. N. Assembly, Growth, and Catalytic Activity of Gold Nanoparticles in Hollow Carbon Nanofibers. *ACS Nano* **2012**,

6, 2000-2007.

[19]. Korhonen, J. T.; Hiekkataipale, P.; Malm, J.; Karppinen, M.; Ikkala, O.; Ras, R. H. A. Inorganic Hollow Nanotube Aerogels by Atomic Layer Deposition onto Native Nanocellulose Templates. *ACS Nano* **2011**, 5, 1967-1974.

[20]. Liang, H. W.; Wang, L.; Chen, P. Y.; Lin, H. T.; Chen, L. F.; He, D.; Yu, S. H. Carbonaceous Nanofiber Membranes for Selective Filtration and Separation of Nanoparticles. *Advanced Materials* **2010**, 22, 4691-4695.

[21].Yuan, J.; Liu, X.; Akbulut, O.; Hu, J.; Suib, S. L.; Kong, J.; Stellacci, F. Superwetting Nanowire Membranes for Selective Absorption. *Nature Nanotechnology* **2008**, 3, 332-336.

[22]. Gu, G.; Schmid, M.; Chiu, P. W.; Minett, A.; Fraysse, J.; Kim, G. T.; Roth, S.; Kozlov, M.; Munoz, E.; Baughman, R. H. V2O5 Nanofibre Sheet Actuators. *Nature Materials* **2003**, 2, 316-319.

[23]. Capadona, J. R.; Van Den Berg, O.; Capadona, L. A.; Schroeter, M.; Rowan, S. J.; Tyler, D. J.; Weder, C. A Versatile Approach for The Processing of Polymer Nanocomposites with Self-assembled Nanofibre Templates. *Nature Nanotechnology* **2007**, 2, 765-769.

[24]. Chen, L. F.; Zhang, X. D.; Liang, H. W.; Kong, M.; Guan, Q. F.; Chen, P.; Wu, Z. Y.; Yu, S. H. Synthesis of Nitrogen-Doped Porous Carbon Nanofibers as an Efficient Electrode Material for Supercapacitors. *ACS Nano* **2012**, 6, 7092-7102.

[25]. Qie, L.; Chen, W. M.; Wang, Z. H.; Shao, Q. G.; Li, X.; Yuan, L. X.; Hu, X. L.; Zhang, W. X.; Huang, Y. H. Nitrogen-Doped Porous Carbon Nanofiber Webs as Anodes for Lithium Ion Batteries with a Superhigh Capacity and Rate Capability. *Advanced Materials* **2012**, 24, 2047-2050.

[26]. Hartgerink, J. D.; Beniash, E.; Stupp, S. I. Self-assembly and Mineralization of Peptide-Amphiphile Nanofibers. *Science* **2001**, 294, 1684-1688.

[27]. Aida, T.; Meijer, E. W.; Stupp, S. I. Functional Supramolecular Polymers. *Science* **2012**, 335, 813-817.

[28]. Min, B. M.; Lee, S. W.; Lim, J. N.; You, Y.; Lee, T. S.; Kang, P. H.; Park, W. H. Chitin and Chitosan Nanofibers: Electrospinning of Chitin and Deacetylation of Chitin Nanofibers. *Polymer* **2004**, 45, 7137-7142.

[29]. Madihally, S. V.; Matthew, H. W. T. Porous Chitosan Scaffolds for Tissue Engineering. *Biomaterials* **1999**, 20, 1133-1142.

[30]. Qian, L.; Zhang, H. Green Synthesis of Chitosan-based Nanofibers and Their Applications. *Green Chemistry* **2010**, 12, 1207-1214.

[31]. Gutierrez, M. C.; Ferrer, M. L.; del Monte, F. Ice-templated Materials: Sophisticated Structures Exhibiting Enhanced Functionalities Obtained After Unidirectional Freezing and Ice-segregation-induced self-assembly. *Chemistry of Materials* **2008**, 20, 634-648.

[32]. Deville, S.; Saiz, E.; Nalla, R. K.; Tomsia, A. P. Freezing as A Path to Build Complex Composites. *Science* **2006**, 311, 515-518.

[33]. Zhang, H. F.; Hussain, I.; Brust, M.; Butler, M. F.; Rannard, S. P.; Cooper, A. I. Aligned Two- and Three-dimensional Structures by Directional Freezing of Polymers and Nanoparticles. *Nature Materials* **2005**, 4, 787-793.

[34]. Xu, Z.; Zhang, Y.; Li, P. G.; Gao, C. Strong, Conductive, Lightweight, Neat Graphene Aerogel Fibers with Aligned Pores. *ACS Nano* **2012**, 6, 7103-7113.

[35]. Deville, S. Freeze-casting of Porous Ceramics: A Review of Current Achievements and Issues. *Advanced Engineering Materials* **2008**, 10, 155-169.

[36]. Yan, J.; Chen, Z.; Jiang, J.; Tan, L.; Zeng, X. C. Free-Standing All-Nanoparticle Thin Fibers: A Novel Nanostructure Bridging Zero- and One-Dimensional Nanoscale Features. *Advanced Materials* **2009**, 21, 314-319.

[37]. Ifuku, S.; Nogi, M.; Abe, K.; Yoshioka, M.; Morimoto, M.; Saimoto, H.; Yano, H. Preparation of Chitin Nanofibers with A Uniform Width as Alpha-chitin from Crab Shells. *Biomacromolecules* **2009**, 10, 1584-1588.

[38]. Li, J.; Revol, J. F.; Naranjo, E.; Marchessault, R. H. Effect of Electrostatic Interaction on Phase Separation Behaviour of Chitin Crystallite Suspensions. *International Journal of Biological Macromolecules* **1996**, 18, 177-187.

[39]. Koehnke, T.; Lin, A.; Elder, T.; Theliander, H.; Ragauskas, A. J. Nanoreinforced Xylan-cellulose Composite Foams by Freeze-casting. *Green Chemistry* **2012**, 14, 1864-1869.

[40]. Petzold, G.; Aguilera, J. M. Ice Morphology: Fundamentals and Technological Applications in Foods. *Food Biophysics* **2009**, 4, 378-396.

[41]. Kiani, H.; Sun, D. W. Water Crystallization and its Importance to Freezing of Foods: A review. *Trends in Food Science and Technology* **2011**, 22, 407-426.

[42]. Hobbs, P. V. Ice Physics, Clarendon Press, Oxford, **1974**.

[43]. Korber, C.; Rau, G.; Cosman, M. D.; Cravalho, E. G. Interaction of Particles and A Moving Ice-Liquid Interface. *Journal of Crystal Growth* **1985**, 72, 649-662.

[44]. Wegst, U. G. K.; Schecter, M.; Donius, A. E.; Hunger, P. M. Biomaterials by Freeze Casting. *Phil. Trans. of the R. Soc. A* **2010**, 368, 2099-2121.

[45]. Rodrigues, M. A.; Miller, M. A.; Glass, M. A.; Singh, S. K.; Johnston, K. P. Effect of Freezing Rate and Dendritic Ice Formation on Concentration Profiles of Proteins Frozen in Cylindrical Vessels. *Journal of Pharmaceutical Sciences* **2011**, 100, 1316-1329.

[46]. Gutierrez, M. C.; Garcia-Carvajal, Z. Y.; Jobbagy, M.; Rubio, T.; Yuste, L.; Rojo, F.; Ferrer, M. L.; del Monte, F. Poly(vinyl alcohol) Scaffolds with Tailored Morphologies for Drug Delivery and Controlled Release. *Advanced Functional Materials* **2007**, 17, 3505-3513.

[47]. Svagan, A. J.; Jensen, P.; Dvinskikh, S. V.; Furo, I.; Berglund, L. A. Towards Tailored Hierarchical Structures in Cellulose Nanocomposite Biofoams Prepared by Freezing/Freeze-drying. *Journal of Materials Chemistry* **2010**, 20, 6646-6654.

[48]. Tzoumaki, M. V.; Moschakis, T.; Biliaderis, C. G. Metastability of Nematic Gels Made of Aqueous Chitin Nanocrystal Dispersions. *Biomacromolecules* **2010**, 11, 175-181.

[49]. Nogi, M.; Kurosaki, F.; Yano, H.; Takano, M. Preparation of Nanofibrillar Carbon from Chitin Nanofibers. *Carbohydrate Polymers* **2010**, 81, 919-924.

[50]. Welty, J. R.; Wicks, C. E.; Wilson, R. E.; Rorrer, G. Fundamentals of Momentum, Heat, and Mass Transfer (4th edition), Wiley, Oregon, USA **2001**.

[51]. Clyne, T. W.; Golosnoy, I. O.; Tan, J. C.; Markaki, A. E. Porous Materials for Thermal Management under Extreme Conditions. *Philosophical Transactions of the Royal Society A* **2006**, 364, 125-146.

CHAPTER 4

CHITIN NANOFIBER REINFORCED POLYMER COMPOSITES

4.1 Overview

In this chapter, chitin nanofibers (CNFs) extracted from crab shells were used to reinforce polyethylene oxide (PEO). The dispersion of CNFs in polymer matrix, and the interactions between fiber and matrix were studied by utilizing two relatively new methods for polymer composite community: solvent-leaching of polymer matrix and AFM colloidal probe adhesion. The thermal and mechanical properties of the produced nanocomposites were characterized using differential scanning calorimetry (DSC) and a high-throughput mechanical characterization (HTMECH) apparatus. The results showed that the CNFs were dispersed well and formed network structures in PEO matrix, and they have strong adhesion with PEO, resulting from the hydrogen bonding and van der Waals forces between them. Furthermore, the CNFs greatly enhanced the mechanical properties of PEO. With excellent reinforcing performance and many remarkable inherent properties, CNFs are attractive resources for polymer composite application.

4.2 Introduction

The development of nanofiller-reinforced polymer composites has attracted intense attention from researchers over the past two decades, and various materials have been utilized to enhance the mechanical properties of polymer matrices, such as single-walled/multi-walled carbon nanotubes, layered silicate and nanocellulose [1-15]. Chitin, the second most abundant naturally occurring polymer, forms a highly ordered crystalline

structure in living organisms [16-18]. Nanosized crystalline chitin (chitin nanocrystal or chitin nanowhisker) can be produced by strong acid hydrolysis, and shows excellent mechanical properties, such as longitudinal modulus 150 GPa and transverse modulus 15 GPa [19]. Due to its renewability, high mechanical performance, nanosized dimension, high surface area, low density and other intrinsic properties, chitin nanowhisker has attracted many interests from polymer composite community and has been used to reinforce various polymer matrices, such as poly(styrene-co-butyl acrylate), natural rubber, poly(caprolactone), polyvinyl alcohol and waterborne polyurethane [19-26]. In chapter 2, we report that the CNFs with diameters of ~20 nm were extracted from crab shells by a high pressure homogenization process, and the produced CNFs are well dispersed in water without forming strong network structures. These features make CNFs ideal reinforcing materials for polymer matrices. The aspect ratio of fillers has great impact on their reinforcement, and fillers with large aspect ratio usually reinforce polymers better than the fillers with small aspect ratio [7, 10, 27]. Therefore, we expect that high-aspect-ratio CNFs should have stronger reinforcing effect in polymers compared to chitin nanowhiskers. PEO is a water-soluble and biocompatible semicrystalline polymer that has found applications in various fields, such as electrolyte and biomedical engineering [2, 28, 29]. In the present study, PEO is chosen as a model polymer to investigate the reinforcing effect of CNFs in polymer matrices. The morphological, interfacial, thermal and mechanical properties of the produced CNF/PEO nanocomposites were characterized using SEM, ATR, AFM, DSC, DMA and HTMECH.

4.3 Experimental Methods

4.3.1 Materials

Dried crab shell flakes were purchased from TCI America. Deionized water (18.2 MΩ cm) was prepared in a Barnstead Easypure RoDi purification system. Hydrochloric acid, sodium hydroxide, acetone and ethanol were purchased from EMD Chemical Inc. Polyethylene oxide (PEO, viscosity average molecular weight (*Mv*): 1,000,000 g/mol, Sigma-Aldrich), polyethylene (PE, *Mw*= 40,000 g/mol, Sigma-Aldrich), polystyrene (PS, *Mw* = 230,000, Sigma-Aldrich), poly(vinyl acetate) (PVAc, *Mw* = 50,000, Alfa Aesar), and poly(vinyl alcohol) (PVA, *Mw* = 89,000-98,000, Sigma-Aldrich) were used as received without further purification. 1, 2, 3-trichlorobenzene (TCB, Sigma-Aldrich), hexafluoroisopropanol (HFIP, TCI America), and toluene (Sigma-Aldrich), glycerol (Alfa Aesar, purity> 99%) and diiodomethane (Alfa Aesar, purity>99%) were used as received. Polystyrene (PS) particle with diameters of ~10 μm was purchased from Alfa Aesar Inc.

4.3.2 Chitin Purification and Fibrillation

Dried crab shell flakes were processed to obtain purified chitin [30, 31]. Ground crab shells were refluxed in 5 wt % sodium hydroxide in DI water for 6 h to remove protein. The suspension was filtered and rinsed with DI water until the pH was 7. Next, the filtered solids were treated with 7% hydrochloric acid for 6 h at room temperature to remove minerals. After filtration and washing with DI water, the treated sample was refluxed in a 5% NaOH solution for 2 days to remove residual proteins and the other residues were eliminated by acetone and ethanol extraction. The purified chitin was dispersed in distilled water under an acidic condition and then this mixture was passed

through a high-pressure homogenizer (Bee International Inc., MA USA) to generate CNFs (aqueous medium pH is ~ 4.1).

4.3.3 Preparation of CNF/PEO Nanocomposite Films

The PEO was firstly dissolved 2% by mass in DI water at room temperature under a magnetic stirring. To prepare 5, 10, 15 and 20 wt.% CNF/PEO composite films, the proper amount of CNF/water dispersions were added to the PEO solution. These mixtures were magnetically stirred for two days, and were subsequently casted into a PS Petri dish, followed by drying under vacuum at 40 ˚C for two days. The free standing dried CNF/PEO nanocomposite films were obtained by carefully peeling films from PS substrate. A neat PEO film was prepared using the same processing conditions for comparison. Both neat PEO and composite films had a thickness of ~50 μm.

4.3.4 Fabrication of CNF/PS Composites and Polymer Film Preparation

The produced CNF/water dispersion was added to PS particle suspension (10 μm, 2.5 wt% in water), followed by agitation using a rotational shaker for 12 h. The mixture was then centrifuged in a micro-centrifuge (VWR Micro 1207). The CNF coated PS particles were settled at the bottom of the container.

The CNFs/water dispersion was blade-casted on Piranha solution cleaned silicon wafer. The casted film was firstly dried in fume hood at room temperature and further dried at 50 ˚C in convection oven. The PE solution was dissolved 5% by mass in hot 1, 2, 3-trichlorobenzene (TCB, Sigma-Aldrich) at ~100 ˚C. The PS solution was prepared by dissolving 10% by mass in toluene. 5 wt. % PVOH and PVAc solutions were prepared in hexafluoroisopropanol (HFIP, TCI America). The PEO solution was prepared by dissolving 1% by mass in DI water. Polymer films were prepared on Piranha-etched

(30/70 vol% H_2O_2/concentrated H_2SO_4 at 80 ˚C for 2 h) silicon substrates, by using a knife-edge coating method described in detail elsewhere [32]. The casted polymer films were firstly dried at room temperature for 24 h and then dried under vacuum for at least 12 h (PVAc at 20 ˚C for 48 h and other polymers at 60 ˚C for 12 h) to remove the residual solvent. After drying, they were transferred to a desiccator and stored prior to measurements. Film thickness was approximately 10-20 μm using an interferometer.

4.3.5 Materials Characterization

The morphologies of the prepared materials in this chapter were characterized using Field-Emission Scanning Electron Microscopy (Zeiss Ultra 60, Carl Zeiss SMT, Ltd., Thornwood, NY USA). Before imaging, these samples were coated with a thin layer of gold/palladium (Hummer IV Sputtering System) to prevent sample charging. The surface charge of CNFs at pH ~ 4.1 in water was measured by a Malvern Zetasizer Nano ZS 90.

The attenuated total reflectance (ATR) spectra of CNF film, neat PEO film and nanocomposites were recorded using a Bruker Vertex 80v FTIR spectrometer coupled to a Hyperion 2000 IR microscope under a 20x magnification ATR objective (Bruker Optics, Inc., Billerica, MA). Measurements were collected from 4000 to 400 cm^{-1} with a resolution of 4 cm^{-1}, and were averaged over 64 scans.

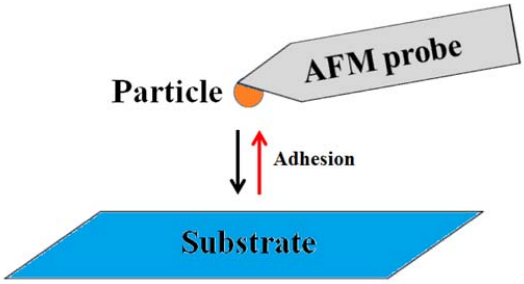

Figure 4.1 Schematic of adhesion measurements using an AFM colloidal probe method.

Adhesion measurements were carried out using atomic force microscopy (AFM) (Veeco Dimension 3100) (Figure 4.1). Tipless rectangular cantilevers with nominal spring constants of 0.6−3.7 N/m (Applied NanoStructures, Inc., Santa Clara, CA) were used. Single CNF-coated or bare PS particles were glued to the tipless cantilevers with a small amount of epoxy resin (Epoxy Marine, Loctite, Westlake, OH USA) using a procedure described in detail elsewhere [33]. The actual spring constants for the cantilevers with the attached CNF-coated or bare PS particles (0.7−1.1 N/m) were determined directly by the methods of Burnham and Hutter et al. [34]. A series of 20 force-distance curves were measured for each combination of PS/CNF or bare PS tip-polymer surface, taken on three separate substrate surfaces within three randomly chosen 10 μm × 10 μm areas on each substrate under normal air condition (20 ˚C, humidity 25-30%). Three separate CNF-coated or bare PS particle tips were used for each species. The applied load during force measurements was 2.5 nN.

The mean (R_a) and root-mean-square (*rms*) surface roughness of each polymer film for adhesion measurements were obtained from topography scans of three

randomly-chosen 10 μm×10 μm areas on each polymer surface by using atomic force microscopy (AFM, Veeco Dimension 3100).

Contact angles were measured at 20 ˚C on the different polymer surfaces using a video contact angle system (AST products 2500XE, Billerica, MA). Three standard testing liquids were chosen, two polar liquids (DI water and glycerol) and one nonpolar (diiodomethane), to calculate the surface tension components of each polymer surfaces. Nine 1 μL drops of each liquid were used for the contact angle measurement of each polymer surface. Surface tension components corresponding to van der Waals (VDW), Lewis acid, and Lewis basic interactions were calculated from measured contact angle data by using van Oss and Good's van der Waals acid-base theory [35]. According to this theory, the surface energy is accessed from equation 4.1.

$$\gamma_S = \gamma_S^{vW} + 2(\gamma_S^+ \gamma_S^-)^{1/2} \qquad \text{Equation 4.1}$$

Where γ_S is the total surface tension, γ_S^{vW} is the van der Waals component, γ_S^+ is the acid (electron acceptor) component, and γ_S^- is the base (electron donor) component. The relation between surface energy components and contact angle (θ) is given as:

$$\gamma_L(1 + \cos\theta) = 2(\gamma_S^{vW}\gamma_L^{vW})^{1/2} + 2(\gamma_S^+\gamma_L^-)^{1/2} + 2(\gamma_L^+\gamma_S^-)^{1/2} \quad \text{Equation 4.2}$$

Where γ_L represents the surface energy of the testing liquids. Owing to the known components of γ_L for three liquids, the γ_S components can be determined by regression. The surface tensions of the testing liquids are as follows: water, $\gamma^+ = \gamma^- = 25.5$, $\gamma^{yW} = 21.8$, $\gamma = 72.8$ mJ/m^2; glycerol, $\gamma^+ = 3.92$, $\gamma^- = 57.4$, $\gamma^{yW} = 34.0$, $\gamma = 64.0$ mJ/m^2; diiodomethane, $\gamma^+ = \gamma^- = 0$, $\gamma^{yW} = 50.8$, $\gamma = 50.8$ mJ/m^2 [36, 37].

Differential scanning calorimetry (DSC) (Q200, TA Instruments, USA) was used to obtain the melting temperature and crystallinity of neat PEO and PEO nanocomposites. Approximately 5-10 mg of sample was loaded into aluminum pan. The PEO samples were heated and cooled at a rate of 10 ˚C/min under a nitrogen flow of 50 ml/min. The samples were firstly cooled from room temperature to -80 ˚C, held at -80 ˚C for 5 min, and were heated to 120 ˚C, followed by maintaining at this temperature for 5 min and cooling to room temperature.

The glass transition temperatures of the materials were measured using dynamic mechanical analysis (DMA, Q800, TA Instruments, DE USA). The samples were cut into rectangular strips about ~3 cm long and ~3 mm wide and were tested in a tension mode while being heated from -90 ˚C to 40 ˚C with a heating rate of 2 ˚C/min. The testing frequency is 1 Hz, and all measurements were performed in the linear viscoelastic region.

Mechanical characterization of neat PEO and PEO nanocomposites was conducted using a high-throughput mechanical characterization (HTMECH) apparatus under ambient conditions, described in detail elsewhere [38, 39]. Briefly, the polymer films were mounted in between two stainless steel plates and indented by a steel pin with a diameter of 1.5 mm at a constant strain rate (0.5 mm/s), resulting in equi-biaxial deformation. For each sample, a minimum of 9 stress-strain tests were performed to obtain films' mechanical properties, such as elastic modulus and tensile strength.

4.4 Results and Discussion

4.4.1 CNF Dispersion in PEO Matrix

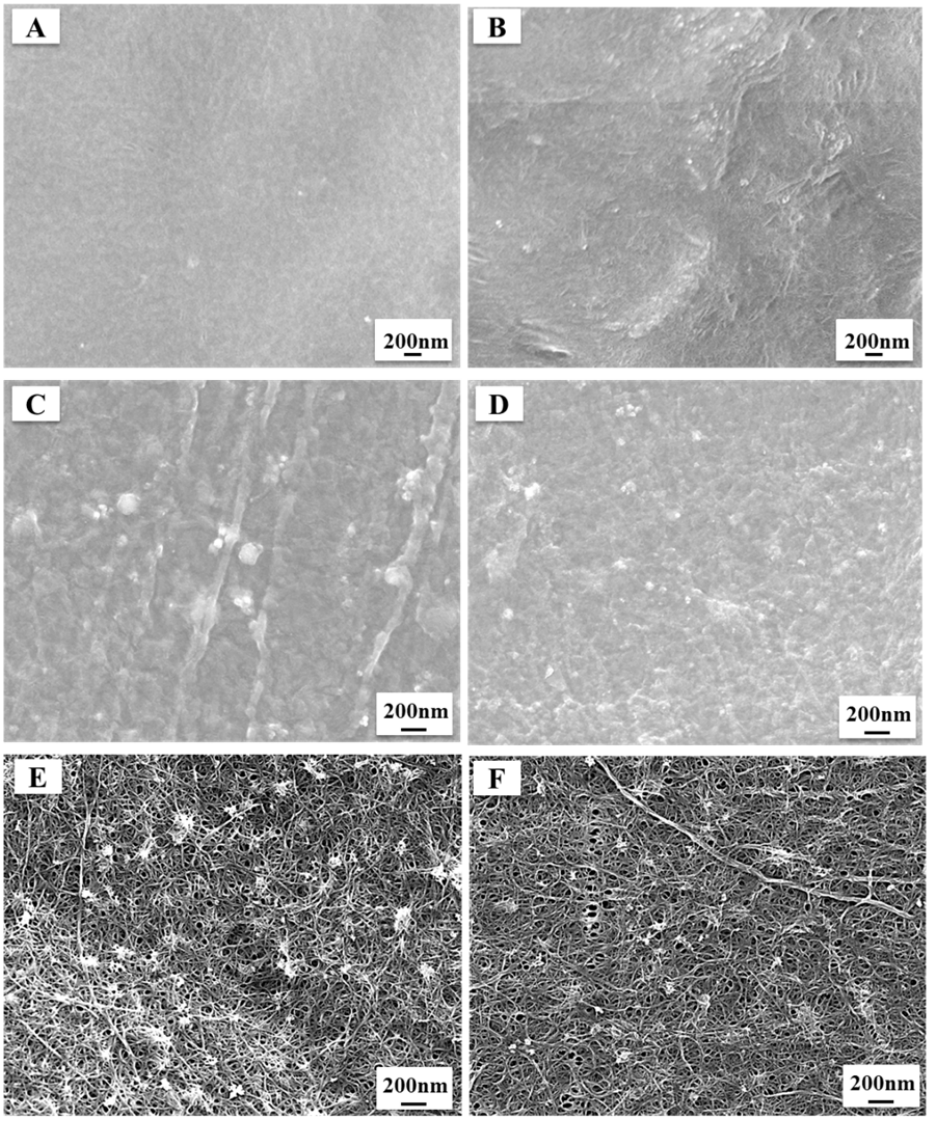

Figure 4.2 (A) and (C) are the fractured cross section and top SEM images of 10% CNF/PEO composites, respectively; (B) and (D) are the fractured cross section and top SEM images of 20% CNF/PEO composites, respectively; (E) and (F) are the top SEM images of dried solvent-washed 10% and 20% CNF/PEO composites, respectively.

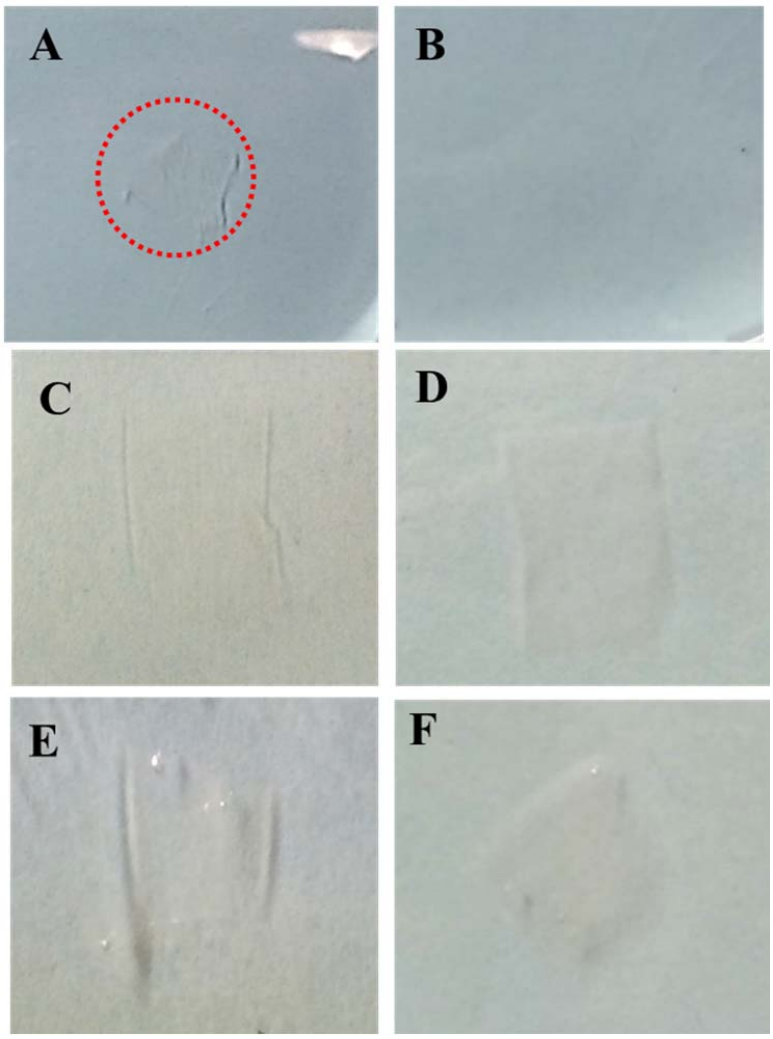

Figure 4.3 (A), (C) and (E) are the digital photos of neat PEO, 5% CNF/PEO and 20% CNF/PEO films that were immersed in water, respectively. The photos were taken ~30 s after placing these films in water; (B) is the digital photo of neat PEO film after ~3 hours of water immersion; (D) and (F) are the digital photos of 5% CNF/PEO and 20% CNF/PEO films that were immersed in ethanol, respectively. The films were firstly immersed in water for 10 days and then immersed in ethanol for 3 days.

Dispersion of fillers in polymer matrix has a great effect on the mechanical properties of the resulting polymer composites [7, 10, 27]. SEM was firstly used to characterize the dispersion of CNFs in PEO matrix, Figure 4.2 A-D showed that two

composites have void-free surfaces, and CNFs could not be observed, suggesting that CNFs were fully imbedded in PEO matrix and had good adhesion with PEO. TEM was subsequently utilized to analyze the CNFs' dispersion in matrix, but their dispersion still could not be successfully characterized because of the similar contrast between CNF and PEO (data is not shown here). Since PEO is water soluble, the produced composite films were immersed in water to remove PEO domains in composites. After repeating water washing and subsequent water exchange with ethanol, these films were dried at ambient condition. As shown in Figure 4.3, neat PEO film was totally destructed within 3 hours of water immersion, whereas CNF/PEO composites can still maintain the film shape within 10 days of water immersion and 3 days of ethanol immersion before drying. Figure 4.2 E and F show the top surface morphologies of the dried solvent-washed composite films. Porous fibrous network structures are observed from both samples, and most fibers in Figure 4.2 E have diameters ranging from 5 to 50 nm. Despite more fiber aggregates were shown for 20% CNF/PEO, there are still many fibers with diameters of below 50 nm (Figure 4.2 F). Figure 4.2 and 4.3 clearly show that the CNFs were dispersed well and formed network structures in PEO matrix. We reason that the great dispersion of CNFs in matrix is ascribed to the excellent dispersion of CNFs in water before their mixing with PEO, electrostatic repulsion between CNFs in PEO solution (pH of CNF/PEO solution is below 6), and strong adhesion between CNF and PEO. The adhesion study is shown below.

4.4.2 Investigation of CNF Interaction with PEO Matrix Using ATR

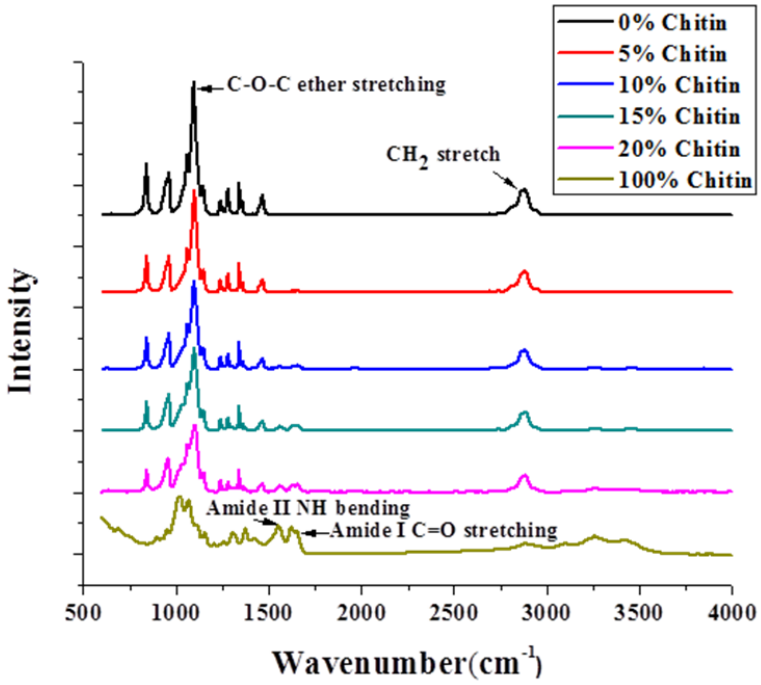

Figure 4.4 ATR spectra of neat PEO, CNF and PEO/CNF composite films.

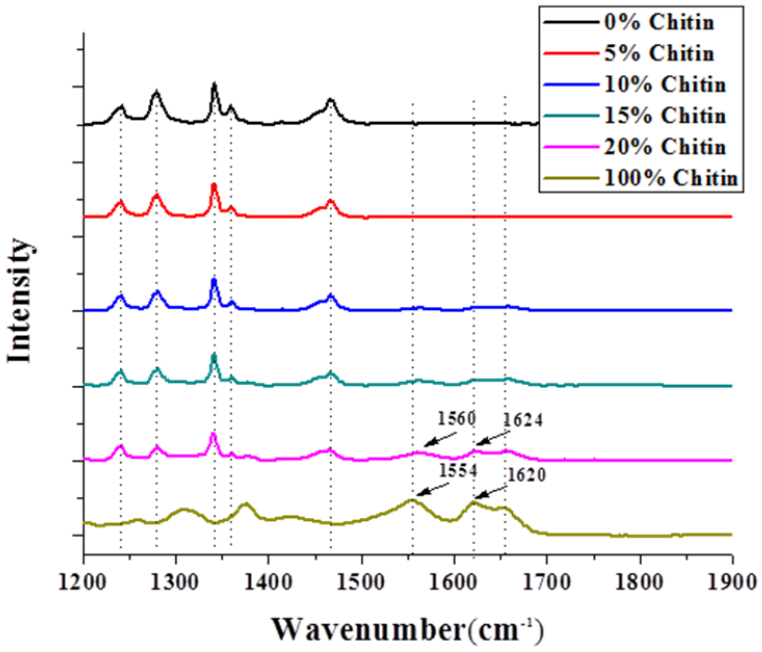

Figure 4.5 Enlarged ATR spectra of neat PEO, CNF and PEO/CNF composite films.

In terms of chemical structures of chitin and PEO, it is expected that hydrogen bonds forms between them since -O- in PEO is a hydrogen bond acceptor and there are many hydrogen bond donors in chitin. Infrared spectroscopy is a highly effective method for investigating hydrogen bonding interactions in blend composites [40]. As shown in Figure 4.4, the characteristic absorption bands for PEO are detected at 1095 and 2878 cm^{-1}, which are attributed to C-O-C stretching and CH_2 stretching, respectively [4, 27]. The characteristic peaks of chitin such as amide band I at 1654 and 1620 cm-1, amide band II at 1554 cm^{-1} are observed [16-18]. All these characteristic peaks from chitin and PEO can be detected from all the composites. With decreasing CNF loading from 100% to 20%, the amide I and amide II shift to higher frequencies from 1620 to 1624 and from 1554 to 1560, respectively (Figure 4.5). This may result from the fact that the part of strong hydrogen bonds between CNFs has been disrupted with addition of PEO. It is possible that CNF and PEO formed hydrogen bonds and the red shifts of amide I and II occurred because the hydrogen bonds between CNFs are stronger than those between CNF and PEO.

4.4.3 Investigation of CNF Interaction with PEO Matrix Using an AFM Colloidal Probe Method

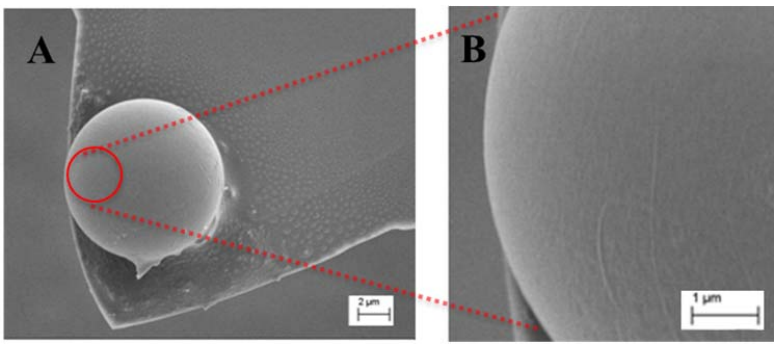

Figure 4.6 (A) SEM image of CNF-coated PS particles; (B) Enlarged SEM image of CNF-coated PS particle.

Table 4.1 Surface roughness of the various polymer surfaces.

Surface	PE	PS	PVAc	PVOH	PEO
Ra(nm)	4.2 ± 0.8	2.4 ± 0.4	1.5 ± 0.3	1.6 ± 0.4	8.3 ± 2.2
rms (nm)	4.3 ± 0.8	2.8 ± 0.4	1.7 ± 0.3	1.9 ± 0.4	8.7 ± 2.4

Table 4.2 Contact angles (°) of polymer surfaces with three testing liquids.

Substrate	water	glycerol	diiodomethane
PE	105.2 ± 4.0	87.3 ± 2.1	52.8 ± 2.0
PS	101.1 ± 3.0	84.2 ± 2.0	33.6 ± 2.0
PVAc	60.7 ± 2.9	70.7 ± 3.0	37.8 ± 3.0
PVOH	46.2 ± 1.4	44.0 ± 1.3	40.4 ± 1.4
PEO	19.0 ± 4.0	46.8 ± 2.0	33.8 ± 2.5
Chitin	56.7 ± 1.4	46.7 ± 1.4	37.4 ± 2.0

Table 4.3 Surface tension components (mJ/m^2) of various polymer surfaces.

Surface	γ^{vW}	γ^{+}	γ^{-}	γ
PE	33	0	0	33.0
PS	43	0.2	0.4	43.2
PVAc	41	0.6	16.7	46.8
PVOH	39	1.1	28.8	50.4
PEO	43	0	64.0	43.0
Chitin	41	1.3	17.1	50.4

ATR data cannot prove if there is hydrogen bonding formation between CNF and PEO. To further study the interactions between CNF and PEO, the adhesion

measurements were conducted using an AFM colloidal probe method. Figure 4.6 shows the morphologies of the CNF-coated PS particles. The adsorption of CNFs on the PS surface was driven by their electrostatic attraction, where PS particle has negative charge due to surface sulfate groups and CNF has positive charge because of protonated $-NH_3^+$ groups. Five kinds of polymer substrates (PEO, PE, PS, PVAc and PVOH) were chosen to examine the effect of surface chemistry on the adhesion forces of CNFs. The surface roughness, contact angles and calculated surface tension components of these polymers were listed in Table 4.1-4.3. As shown in Table 4.3, PE and PS is essentially apolar, while PEO, PVAc and PVOH have a large Lewis basic component, where lone electron pairs are provided by ether, carbonyl and hydroxyl in PEO, PVAc and PVOH, respectively. These surface tension results are consistent with their molecular structures.

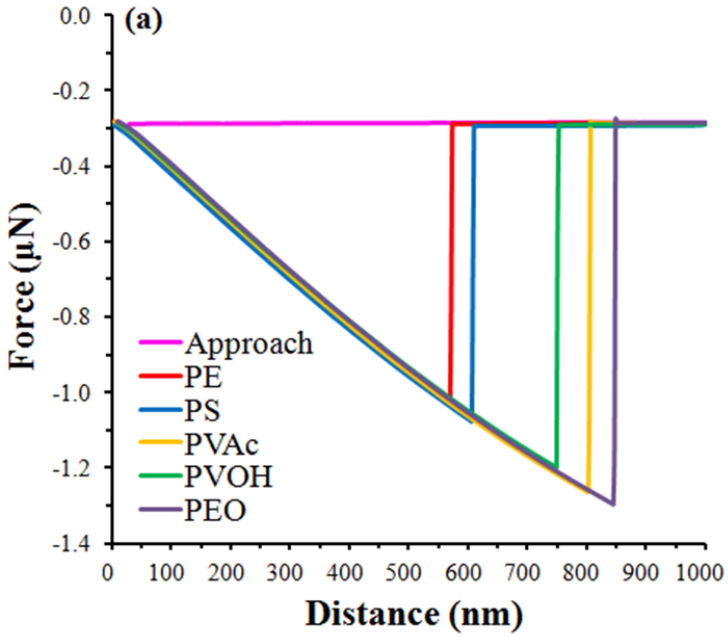

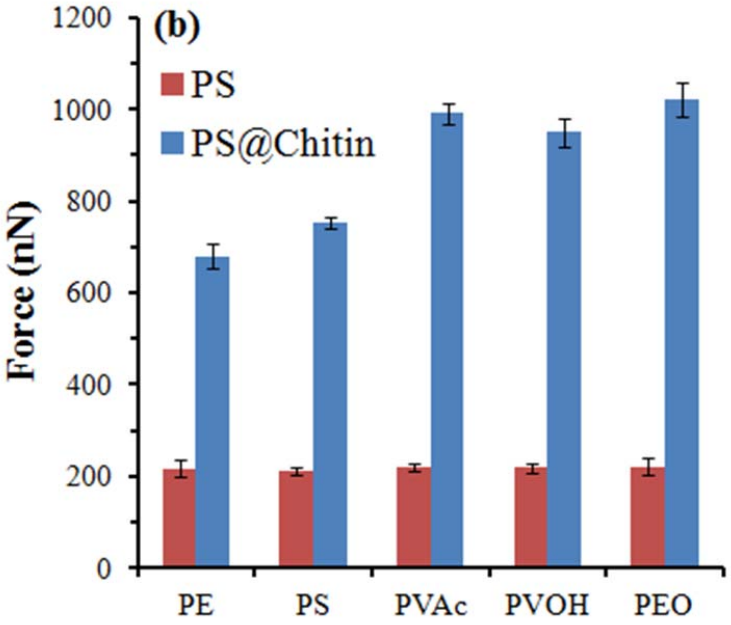

Figure 4.7 (A) Force-distance curves for CNF-coated PS particle on various polymer surfaces; (B) Total adhesion forces for CNF-coated or bare PS particle on various polymer surfaces. PS@Chitin represents the CNF-coated PS particle.

Figure 4.7 A shows typical force-distance curves for CNF-coated PS particles on varied polymer surfaces, which indicated that their interactions are in a short-range (<5 nm). As shown in Figure 4.7 B, the adhesion forces for bare PS were independent on the polymer surface types. This is consistent with the expected results since the adhesion between PS and polymer surfaces is governed by VDW forces [41]. Furthermore, according to the Hamaker model, VDW adhesion between particle and flat surface depends on the Hamaker constant and its contact radii. Since the values of the Hamaker constant for these five polymers are very close (~8-9×10^{-20} J), the VDW forces are determined by the contact radius. Therefore, the similar VDW adhesion forces between bare PS and these polymer surfaces suggest that the small variation in surface roughness of these polymers (Table 4.1) didn't affect their contact radii.

In contrast, the adhesion forces for CNF varied with different polymer surfaces (Figure 4.7 B). PE, the most apolar in the series, shows the lowest adhesion force value, while PVAc, PVOH, and PEO with high Lewis basic components possess higher adhesion forces. Typically, the short-range interaction (<5 nm) includes dispresion (nonpolar, VDW force) and non-dispersion force (polar, acid-base interaction). Since the γ^{yW} of these polymer surfaces are not significatly different (Table 4.3), the VDW forces for CNF are almost indepepdent on polymer surface types. Therefore, the differences in adhesion forces suggest that Lewis acidic and basic components of the polymer surfaces play an important role in adhesion with CNF.

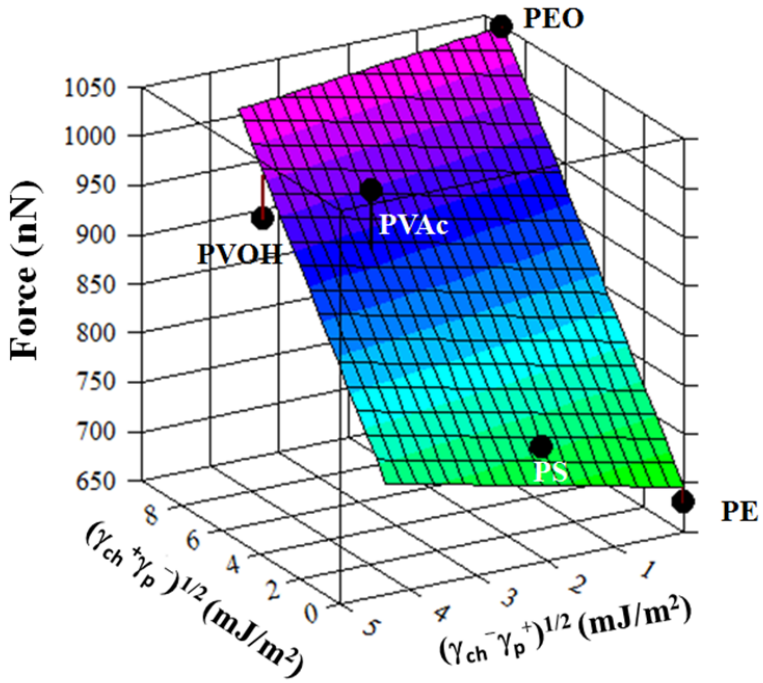

Figure 4.8 Fitting of a planar model of equation 4.4 to adhesion force data.

Assuming Van Oss and Good's Lifshitz-van der Waals acid-base theory for solid (chitin surface, Ch)-solid (polymer surface, P) interface, the relationship of the adhesion

force with the surface energy and molecular structures of the polymers can be expressed as:

$$F_{ad} \propto a\sqrt{\gamma_{Ch}^{vw}\gamma_{P}^{vw}} + b\sqrt{\gamma_{Ch}^{+}\gamma_{P}^{-}} + c\sqrt{\gamma_{Ch}^{-}\gamma_{P}^{+}} \quad \text{Equation 4.3}$$

Where F_{ad} is the experimentally determined adhesion force, and *a, b* and *c* are coefficients scaling the VDW and acidic-basic contributions, respectively. Since the VDW components of polymer (γ_P^{vW}) are similar, the equation 4.3 can be simplified as:

$$F_{ad} \propto A + b\sqrt{\gamma_{Ch}^{+}\gamma_{P}^{-}} + c\sqrt{\gamma_{Ch}^{-}\gamma_{P}^{+}} \quad \text{Equation 4.4}$$

Where A is a constant. We fitted to the equation 4.4, which is a plane fit plotted along with the adhesion forces in Figure 4.8. Fitting all five polymers led to a correlation coefficient r^2 ~0.88 and the plane is in a good fit, suggesting that the differences in total adhesion forces on varied surfaces should result from the acidity-basicity of the polymer surfaces. Therefore, the adhesion force data indicates that CNFs have acid-base interaction with PEO. Since PEO is primarily composed of electron donors (hydrogen bond acceptor), and chitin has many electron acceptors (hydrogen bond donor), such as –OH, -NH- and $–NH_2$, the acid–base interaction between PEO and chitin should be closely equivalent to hydrogen bonding here.

4.4.4 Thermal Properties of CNF/PEO Nanocomposites

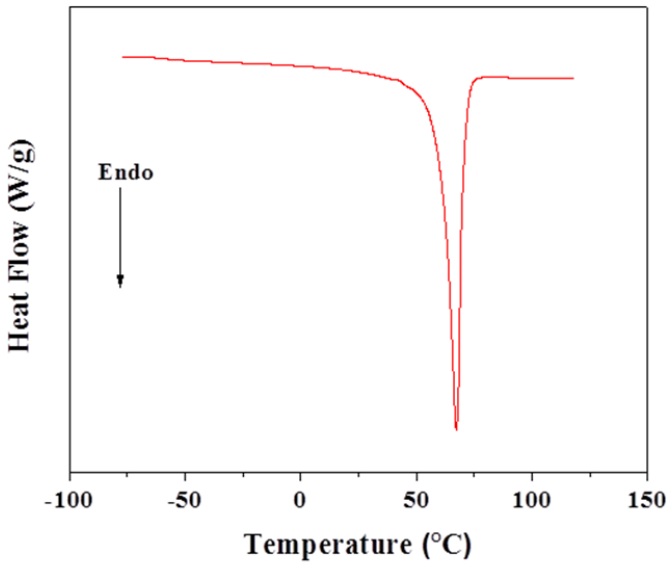

Figure 4.9 DSC curve of neat PEO film.

Table 4.4 Melting temperature and crystallinities of neat PEO and PEO/CNF composite films.

Sample	T_m (˚C)	ΔH (J/g)	X_c (%)
Neat PEO	67.3	177.0	86.3
5% Chitin/PEO	65.8	165.5	85.0
10% Chitin/PEO	64.0	152.3	82.6
15% Chitin/PEO	62.7	137.4	78.9
20% Chitin/PEO	62.0	122.3	74.6

The melting temperature (T_m), enthalpy of fusion and crystallinity (X_c) of neat PEO and CNF/PEO composite films were measured using DSC. The degrees of crystallinity of these samples were calculated using equation 4.5 [11]:

$$Xc = \frac{\Delta H_i}{f_i \Delta H_i^m} \times 100 \qquad \text{Equation 4.5}$$

Where ΔH_i is the enthalpy of fusion of the prepared PEO samples, obtained from DSC measurements, f_i is the mass fraction of PEO in composites, and ΔH_i^m is the enthalpy of fusion of 100% crystalline PEO, which is 205 J/g [11]. The neat PEO has melting temperature of 67.3 ˚C and crystallinity of 86.3% (Figure 4.9 and Table 4.4), and the crystallinity and melting temperature of PEO decreased with increasing CNF loading. We reason that the dispersion of CNF in PEO matrix and strong interactions between CNF and PEO hindered the chain diffusion and folding during PEO crystallization, resulting in the low crystallinity for composite samples.

Since DSC curves could not clearly show the glass transition temperatures (T_g) of the prepared PEO samples, DMA was used to determine their T_g. The neat PEO has a T_g of -56.2 ˚C while the T_g of 5%, 10% and 15% CNF/PEO composites are -49.2, -48.7 and 48.4 ˚C, respectively. The increases of glass transition temperatures for the composites resulted from the strong adhesion between CNF and PEO that restricted PEO chain mobility.

4.4.5 Mechanical Properties of CNF/PEO Nanocomposites

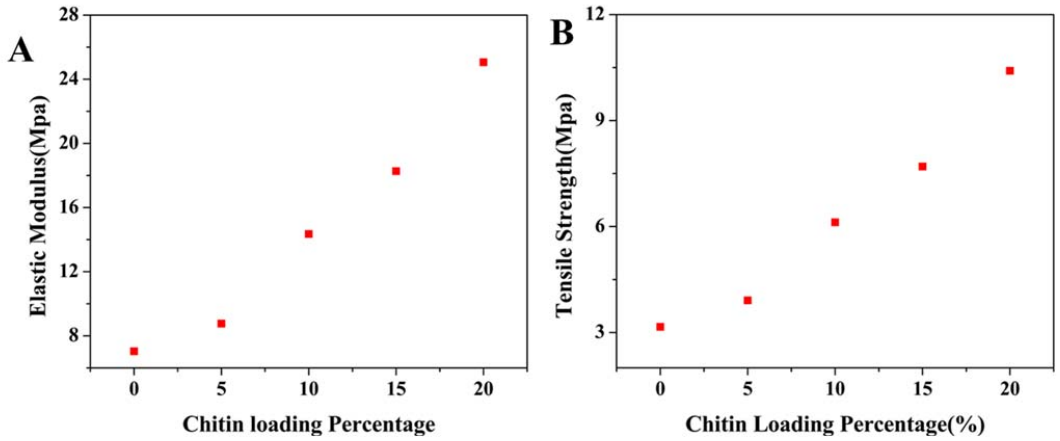

Figure 4.10 (A) Elastic modulus; (B) Tensile strength of neat PEO and PEO/CNF composite films.

The mechanical properties of neat PEO and PEO/CNF composite films are listed in Figure 4.10. The elastic modulus and tensile strength of the prepared PEO samples increased with increasing CNF loading. The elastic modulus and tensile strength of 20% CNF/PEO composites are ~3 times greater than those of neat PEO. The increases in tensile strength and modulus result from CNFs' high mechanical properties, their strong interactions with PEO, and CNF network structure formation in matrix, as demonstrated in AFM force measurements and dispersion study, where the strong adhesion between CNF and PEO, and CNF networks lead to efficient stress transfer from matrix to CNF and from CNF to CNF. In addition, it is worth noting that not all the fillers showed the same reinforcement trend as CNF illustrated above. For example, Xu et al. studied the reinforcing effects of cellulose nanocrystals and cellulose nanofibrils in PEO matrices. The tensile strength and modulus of the prepared composites initially increased when loading fillers up to 7% and then decreased as cellulose content further increased. The

authors reasoned that the decreases in mechanical properties at higher filler loading resulted from filler agglomerations [27].

4.5 Conclusions

In this study, the defect-free CNF/PEO nanocomposite films were successfully fabricated by a solution casting method and the structure-property relationships of the nanocomposites were established. The solvent-leaching of CNF/PEO nanocomposites showed that the CNFs were dispersed well and formed network structures in PEO matrix. The AFM colloidal probe adhesion measurements demonstrated that CNF has strong adhesion with PEO, resulting from the hydrogen bonding and van der Waals forces between them. The researchers in the field of polymer composites usually utilize IR to qualitatively determine if there is hydrogen bonding formation between the components in composites, but this technique cannot perform well for some systems, such as single components originally having hydrogen bonding [40]. Here, we prove that AFM colloidal probe adhesion method can be an alternative to quantitatively characterize the hydrogen bonding formation in composites.

The crystallinities of PEO in composites are lower than that of neat PEO, which may be attributed to the fact that the dispersion of CNF in PEO matrix and strong interactions between CNF and PEO restricted the chain mobility during PEO crystallization. Compared to neat PEO, the tensile strength and elastic modulus of the nanocomposites greatly increased with higher CNF loading. In addition to CNFs' great mechanical properties, the strong interactions between CNF and PEO, and CNF network structure formation in matrix played important roles in improving the mechanical properties of the composites because these two effects allowed the efficient stress transfer

from matrix to fiber and from fiber to fiber. With the great reinforcing effect in polymer, light weight and many other inherent properties such as excellent mechanical properties and renewability, the CNFs are promising fillers in polymer composites for a wide range of applications.

4.6 References

[1]. Yano, H.; Sugiyama, J.; Nakagaito, A. N.; Nogi, M.; Matsuura, T.; Hikita, M.; Handa, K. Optically Transparent Composites Reinforced with Networks of Bacterial Nanofibers. *Advanced Materials* **2005**, 17, 153-155.

[2]. Chatterjee, T.; Yurekli, K.; Hadjiev, V. G.; Krishnamoorti, R. Single-Walled Carbon Nanotube Dispersions in Poly(ethylene oxide). *Advanced Functional Materials* 2005, 15, 1832-1838.

[3]. Capadona, J. R.; Berg, O.; Capadona, L. A.; Schroeter, M.; Rowan, S. J.; Tyler, D. J.; Weder, C. A versatile approach for the processing of polymer nanocomposites with self-assembled nanofibre templates. *Nature nanotechnology* **2007**, 2, 765-769.

[4]. Brown, E. E.; Laborie, M. G. Bioengineering Bacterial Cellulose/Poly(ethylene oxide) Nanocomposites. *Biomacromolecules* **2007**, 8, 3074-3081.

[5]. Goettle, L. A.; Lee, K. Y.; Thakkar, H. Layered Silicate Reinforced Polymer Nanocomposites: Development and Applications. *Polymer Reviews* **2007**, 47, 291-317.

[6]. Chatterjee, T.; Mitchell, C. A.; Hadjiev, V. G.; Krishnamoorti, R. Hierarchical Polymer–Nanotube Composites. *Advanced Materials* **2007**, 19, 3850-3853.

[7]. Fu, S.; Feng, X.; Lauke, B.; Mai, Y. Effects of Particle Size, Particle/Matrix Interface Adhesion and Particle Loading on Mechanical Properties of Particulate–Polymer Composites. *Composites: Part B* **2008**, 39, 933-961.

[8]. Chen, B.; Evans, J. R. G.; Greenwell, H. C.; Boulet, P.; Coveney, P. V.; Bowden, A. A.; Whiting, A. A Critical Appraisal of Polymer-Clay Nanocomposites. *Chemical Society Reviews* **2008**, 37, 568-594.

[9]. Bredeau, S.; Peeterbroeck, S.; Bonduel, D.; Alexandre, M. Mini-review from Carbon Nanotube Coatings to High-Performance Polymer Nanocomposites. *Polymer International* **2008**, 57, 547-553.

[10]. Klemm, D.; Kramer, F.; Moritz, S.; Lindström, T.; Ankerfors, M.; Gray, D.; Dorris, A. Nanocelluloses: A New Family of Nature-Based Materials. *Angewandte Chemie International Edition* **2011**, 50, 5438-5466.

[11]. Kim, I. T.; Lee, J. H.; Shofner, M. L.; Jacob, S. K.; Tannenbaum, R. Crystallization Kinetics and Anisotropic Properties of Polyethylene Oxide/Magnetic Carbon Nanotubes Composite Films. *Polymer* **2012**, 53, 2402-2411.

[12]. Abdul Khalil, H. P. S.; Bhat, A. H.; Ireana Yusra, A. F. Green Composites from Sustainable Cellulose Nanofibrils: a Review. *Carbohydrate Polymers* **2012**, 87, 963-979.

[13]. Lee, J.; Shofner, M. L. Dispersion of Polymer-Decorated Hydroxyapatite Nanoparticles in Poly(ethylene oxide) at Low Grafting Densities. *Polymer* **2012**, 53, 5146-5154.

[14]. Yang, J.; Han, C.; Duan, J.; Xu, F.; Sun, R. Mechanical and Viscoelastic Properties of Cellulose Nanocrystals Reinforced Poly(ethylene glycol) Nanocomposite Hydrogels. *ACS Applied Materials and Interfaces* **2013**, 5, 3199-3207.

[15]. Miao, C.; Hamad, W. Y. Cellulose Reinforced Polymer Composites and Nanocomposites: A Critical Review. *Cellulose* **2013**, 20, 2221-2262.

[16]. Rinaudo, M. Main Properties and Current Applications of Some Polysaccharides as Biomaterials. *Polymer International* **2008**, 57, 397-430.

[17]. Rinaudo, M. Chitin and Chitosan: Properties and Applications. *Progress in Polymer Science* **2006**, 31, 603-632.

[18]. Pillai, C. K. S.; Paul, W.; Sharma, C. P. Chitin and Chitosan Polymers: Chemistry, Solubility and Fiber Formation. *Progress in Polymer Science* **2009**, 34, 641-678.

[19]. Zeng, J.; He, Y.; Li, S.; Wang, Y. Chitin Whiskers: an Overview. *Biomacromolecules* **2012**, 13, 1-11.

[20]. Paillet, M.; Dufresne, A. Chitin Whisker Reinforced Thermoplastic Nanocomposites. *Macromolecules* **2001**, 34, 6527-6530.

[21] Morin, A.; Dufresne, A. Nanocomposites of Chitin Whiskers from Riftia Tubes and Poly(caprolactone). *Macromolecules* **2002**, 35, 2190-2199.

[22]. Nair, K. G.; Dufresne, A. Crab Shell Chitin Whisker Reinforced Natural Rubber Nanocomposites. 1. Processing and Swelling Behavior. *Biomacromolecules* **2003**, 4, 657-665.

[23]. Sriupayo, J.; Supaphol, P.; Blackwell, J.; Rujiravanit, R. Preparation and Characterization of α-chitin Whisker-reinforced Poly(vinyl alcohol) Nanocomposite Films with or without Heat Treatment. *Polymer* **2005**, 46, 5637-5644.

[24]. Junkasem, J.; Rujiravanit, R.; Supaphol, P. Fabrication of α-chitin Whisker-Reinforced Poly(vinyl alcohol) Nanocomposite Nanofibres by Electrospinning. *Nanotechnology* **2006**, 17, 4519-4528.

[25]. Hariraksapitak, P.; Supaphol, P. Preparation and Properties of α-Chitin-Whisker-Reinforced Hyaluronan–Gelatin Nanocomposite Scaffolds. *Journal of Applied Polymer Science* **2010**, 117, 3406-3418.

[26]. Zeng, M.; Gao, H.; Wu, Y.; Fan, L.; Li, A. Preparation and Characterization of Nanocomposite Films from Chitin Whisker and Waterborne Poly(ester-urethane) With or Without Ultra-Sonification Treatment. *Journal of Macromolecular Science, Part A: Pure and Applied Chemistry* **2010**, 47, 867-876.

[27]. Xu, X.; Liu, F.; Jiang, L.; Zhu, J. Y.; Haagenson, D.; Wiesenborn, D. P. Cellulose Nanocrystals vs. Cellulose Nanofibrils: A Comparative Study on Their Microstructures and Effects as Polymer Reinforcing Agents. *ACS Applied Materials and Interfaces* **2013**, 5, 2999-3009.

[28]. Trollsås, M.; Hedrick, J. L. Dendrimer-like Star Polymers. *Journal of American Chemical Society* **1998,** 120*,* 4644-4651.

[29]. Albertsson, A.; K.Varma, I. Recent Developments in Ring Opening Polymerization of Lactones for Biomedical Applications. *Biomacromolecules* **2003**, 4, 1466-1486.

[30]. Nair, K. G.; Dufresne, A. Crab Shell Chitin Whisker Reinforced Natural Rubber Nanocomposites. 1. Processing and Swelling Behavior. *Biomacromolecules* **2003**, 4, 657-665.

[31]. Ifuku, S.; Nogi, M.; Abe, K.; Yoshioka, M.; Morimoto, M.; Saimoto, H.; Yano, H. Preparation of Chitin Nanofibers with a Uniform Width as α-Chitin from Crab Shells. *Biomacromolecules* **2009**, 10, 1584-1588.

[32]. Meredith, J. C.; Karim, A.; Amis, E. J. High-throughput Measurement of Polymer Blend Phase Behavior. *Macromolecules* **2000**, 33, 5760-5762.

[33]. Thio, B. J. R.; Lee, J.; Meredith, J. C. Characterization of Ragweed Pollen Adhesion to Polyamides and Polystyrene Using Atomic Force Microscopy. *Environmental Science and Technology* **2009**, 43, 4308-4313.

[34]. Burnham, N. A.; Chen, X.; Hodges, C. S.; Matei, G. A.; Thoreson, E. J.; Roberts, C. J.; Davies, M. C.; Tendler, S. J. B. Comparison of Calibration Methods for Atomic-force microscopy Cantilevers. *Nanotechnology* **2003**, 14, 1-6.

[35]. Good, R. J.; Van Oss, C. J. Modern Approach of Wettability: Theory and Applications. New York, Plenum Press, **1991**.

[36]. Busscher, H. J.; Arends, J. Determination of the Surface Forces Gamma-S-D and Gamma-S-P from Contact-Angle Measurements on Polymers and Dental Enamel. *Journal of Colloid and Interface Science* **1981**, 81, 75-79.

[37]. Ma, K. X.; Chung, T. S.; Good, R. J. Surface Energy of Thermotropic Liquid Crystalline Polyesters and Polyesteramide. *Journal of Polymer Science Part B-Polymer*

Physics, **1998**, 36, 2327-2337.

[38]. Sormana, J.; Meredith, J. C. High-Throughput Discovery of Structure-Mechanical Property Relationships for Segmented Poly(urethane-urea)s. *Macromolecules* **2004,** *37,* 2186-2195.

[39]. Sormana, J.; Chattopadhyay, S.; Meredith, J. C. High-throughput Mechanical Characterization of Free-Standing Polymer Films. *Review of Scientific Instruments* **2005**, 76, 062214.

[40]. Jin, J.; Hassanzadeh, P.; Perotto, G.; Sun, W.; Brenckle, M. A.; Kaplan, D.; Omenetto, F. G.; Rolandi, M. A Biomimetic Composite from Solution Self-Assembly of Chitin Nanofibers in a Silk Fibroin Matrix. *Advanced Materials* **2013**, 25, 4482-4487.

[41]. Lin, H.; Gomez, I.; Meredith, J. C. Pollenkitt Wetting Mechanism Enables Species-Specific Tunable Pollen Adhesion. *Langmuir* **2013**, 29, 3012-3023.

[42]. Ozkoc, G.; Kemaloglu, S. Morphology, Biodegradability, Mechanical, and Thermal Properties of Nanocomposite Films Based on PLA and Plasticized PLA. *Journal of Applied Polymer Science* **2009**, 114, 2481-2487.

[43]. Jiang, L.; Zhang, J.; Wolcott, M. P. Comparison of Polylactide/Nano-sized Calcium Carbonate and Polylactide/Montmorillonite Composites: Reinforcing Effects and Toughening Mechanisms. *Polymer* **2007**, 48, 7632-7644.

CHAPTER 5

ENGINEERING PATRICLE STABLIZED AQUEOUS FOAMS FROM REWNEWABLE RESOURCES

5.1 Overview

The foam stabilization by particles has recently attracted intense interests from soft and porous materials communities due to its vast opportunities for a wide range of applications. However, most particles employed in these fields are derived from non-renewable resources and possess low aspect ratio, such as spherical shape. Here, we report a new kind of aqueous foam stabilized by renewable high-aspect-ratio chitin nanofibers (CNFs) and the produced liquid foam exhibited strong hindrance on drainage, coalescence and disproportionation. The results showed that CNFs themselves were not effective stabilizers of air-water interface but short-chain amphiphile treated CNFs displayed excellent foaming ability. The effects of CNF and valeric acid concentration on surface tension, foaming ability and stability of the aqueous phase were elucidated. Quartz Crystal Microbalance (QCM) data illustrated that there is a strong affinity between CNF and amphiphile (valeric acid). Interestingly, the surface tension of aqueous dispersion was largely decreased with the combinational addition of CNF and valeric acid in water. SEM images confirmed that CNFs were absorbed, intertwined and formed particle layers at the air-water interface, which played significant roles in stabilizing air bubbles. Due to chitin's unique inherent properties, such as renewability, abundance, biodegradability and high stiffness, we expect that the study of CNF-based aqueous foams should be useful for many research and applications.

5.2 Introduction

Foams are useful as intermediates and end-products for a variety of fields, such as food, cosmetics, oil-recovery, flotation, insulation, transportation and biomedical engineering [1-13]. However, aqueous foams are not thermodynamically stable because of their large air-water interfacial free energy so that they show quite short lifetime. Surfactants and biomolecules are able to lower interfacial free energy but they still cannot strongly hinder film drainage, coalescence or disproportionation of liquid foams [14-20]. Recently**,** the foam stabilization by particles (Pickering foams) has attracted much attention from researchers because of the remarkable stability of the resultant foams. The detachment energy of particles ($\Delta G_{particle}$) from air-water interface is several orders of

$$\boldsymbol{\Delta G_{particle} = \pi R^2 \gamma_{\alpha\beta}(1 - |\cos\theta|)^2} \qquad \text{Equation 5.1}$$

magnitude larger than thermal energy (kT, k is the Boltzmann's constant and T is the temperature) in marked contrast to few kT of interfacial desorption energy for surfactants and the formed particle layer at the interface behaves as an interfacial armor to effectively resist bubble coalescence or disproportionation. In equation 5.1, R is the radius of particle, $\gamma_{\alpha\beta}$ is the interfacial tension and θ is the wetting angle of particle at the interface [21-31]. Currently, there are tremendous needs for renewable materials in society to mitigate energy depletion of fossil fuel, and this drives much research on developing advanced materials from renewable resources. Despite a variety of particles have already been demonstrated as effective stabilizers of air-water interface over the last decade, including metal oxide(silica, alumina etc.), metal (titanium, gold etc.) and polymers (PVDF, PTFE, and PS etc.), the Pickering foams produced from renewable materials are seldom reported [32-46].

Chitin is the second most abundant macromolecule in nature, existing in the exoskeleton of arthropods or the cell walls of fungi and yeast. Chitin is poly (β-(1-4)-N-acetyl-D-glucosamine) having amino, amide and hydroxyl functional groups in polymer chains. Chitin exhibits many excellent properties, such as renewability, biodegradability, and biocompatibility, strong affinity to proteins and high stiffness. However, even though having these inherent benefits, the applications of chitin-based materials are still quite limited mainly due to its strong molecular interactions [47-50]. Up to now, the stabilization properties of chitin at air-water interface have not been reported in the literature before. Recently, our group successfully extracted chitin nanofibers (CNFs) with diameters of ~20 nm from crab shells without employing chitin dissolution. In this chapter, we aim to investigate the interfacial and foaming properties of CNFs in an aqueous phase. Meanwhile, we aim to develop aqueous foams stabilized by renewable CNFs. Particles with low aspect ratio such as spheres are often used as foam stabilizers. Previous research indicated that particles with high aspect ratio were more efficient to prevent foam destabilization than spheres [22, 34, 51]. Thus, it is potential to produce highly stable CNF-based foams because of its relatively high aspect ratio.

5.3 Experimental Method

5.3.1 Materials

Dried crab shell flakes were purchased from TCI America. Deionized water (18.2 MΩ cm) was prepared in a Barnstead Easypure RoDi purification system. Hydrochloric acid, sodium hydroxide, acetone and ethanol were purchased from EMD Chemical Inc. Propionic acid, valeric acid, enanthic acid, caprylic acid and 16-hexadecanoic acid (Sigma-Aldrich, CO., St. Louis, MO USA) were used as received without further

purification. Sulfuric acid (97 wt %, BDH Chemicals Ltd.) and hydrogen peroxide (30 wt.%, BDH Chemicals Ltd) were used for treating silicon wafer.

5.3.2 Chitin Purification and Fibrillation

Dried crab shell flakes were processed to obtain purified chitin [49, 52]. Ground crab shells were refluxed in 5 wt % sodium hydroxide in DI water for 6 h to remove protein. The suspension was filtered and rinsed with DI water until the pH was 7. Next, the filtered solids were treated with 7% hydrochloric acid for 6 h at room temperature to remove minerals. After filtration and washing with DI water, the treated sample was refluxed in a 5% NaOH solution for 2 days to remove residual proteins and the other residues were eliminated by acetone and ethanol extraction. The purified chitin was dispersed in distilled water under an acidic condition and then this mixture was passed through a high-pressure homogenizer (Bee International Inc., MA USA) to generate CNFs (aqueous medium pH is ~ 4.1). A shorter homogenizing duration was used for preparing CNFs in this chapter in comparison to CNFs produced in Chapter 2.

5.3.3 Aqueous Foam Preparation and Characterization

CNFs/water dispersion was obtained from the high pressure homogenization process, and its pH value was adjusted from ~4 to ~7 using a diluted sodium hydroxide solution. The CNF dispersion at each pH was frothed using a rotor-stator homogenizer (IKA UltraTurrax T10) at 20000 rpm for 15 minutes. For CNFs/carboxylic acids/water foaming, small amount of carboxylic acids (propionic acid, valeric acid, enanthic acid or caprylic acid) were added to CNFs/water dispersion. The resulting mixture was agitated using the rotor-stator homogenizer at 8000 rpm for 20 minutes, and subsequently frothed at 20000 rpm for 15 minutes.

After frothing, digital images of chitin samples were immediately taken. A small amount of CNF liquid foam was placed on the top of a microscope glass slide, and observed using the transmission mode of an optical microscope (Olympus BX51 microscope, Olympus America, Inc., Center Valley, PA USA) equipped with a digital camera system. A small amount of CNF liquid foam was dropped on Piranha solution cleaned silicon wafer (Piranha solution: 75% H_2SO_4+25% H_2O_2, treated at 80 ˚C for 1 hour). The droplet was immediately dried with a dry nitrogen jet, and then was coated with a thin layer of gold/palladium (Hummer IV Sputtering System). SEM images were taken using a Zeiss Ultra60 field emission scanning electron microscope (accelerating voltage: 5kV). The zeta potential of CNF/water dispersion was measured by Zetasizer Nano S90. Three measurements (each measurement was averaged over 20 runs) was taken and averaged. The surface tension of CNF dispersion with or without carboxylic acids were measured by a surface tensiometer (Rame-Hart Model 250 Goniometer) based on pendent drop method, and was determined using drop shape analysis of liquid droplet. CNFs/water dispersion was blade-casted on Piranha solution cleaned silicon wafer. The casted film was firstly dried in fume hood at room temperature and further dried at 50 ˚C in convection oven. The contact angle of CNF film was measured by using a video contact angle system (AST products 2500XE, Billerica, MA). The foaming ability of CNF dispersion was accessed by measuring the ratio of foam volume immediately after frothing to the initial liquid volume. The foam stability was evaluated by monitoring this ratio over time at room temperature.

5.3.4 Quartz Crystal Microbalance (QCM) Measurement

The QCM-D has been widely used to evaluate surface properties including adsorption rate, adsorbed mass and viscoelasticity of adsorbed layers for many years. Changes in the resonant frequency of coated QCM sensors can be measured by switching on and off an applied voltage. The shift in the resonant frequency due to bulk adsorption is employed to calculate the areal adsorption by means of the Sauerbrey equation,

$$\Delta m = -c\frac{\Delta f}{n} \qquad \text{Equation 5.2}$$

Where Δm is the mass change per area on the crystal surface, Δf is the resonant frequency change, n is the overtone number (n=1, 3, 5, 7, etc.) and c is a characteristic constant related to the sensitivity of the resonator to changes in mass [53, 54]. In this chapter, QCM-D was used to characterize the adsorption behavior of carboxylic acid on the surface of CNFs at ambient temperature.

Quartz sensors coated with gold were used in QCM-D experiments. These sensors were firstly functionalized with a self-assembled monolayer of 16-hexadecanoic acid. Briefly, gold sensors were first cleaned by UV ozone (UV/Ozone ProCleaner, Bioforce Nanosciences, Inc., IA, USA) for 10 minutes, followed by a 5 min incubation in 5:1:1 H_2O:NH_3:H_2O_2 at 75˚C. The sensors were then rinsed with DI water, and dried with N_2. Sensors were then immersed in a 1 mM ethanolic solution of 16-hexadecanoic acid, adjusted to pH~2 with concentrated HCl. After 48 hours, the self-assembly was terminated by rinsing the substrate in 200 proof ethanol, 10 min sonication in fresh solvent, and then drying under N_2. Following COOH-SAM formation, the CNFs were spin-coated onto the acid treated sensor (Aqueous CNF dispersion: pH~4.9, 5000 rpm). These nanochitin-sensors were used for all QCM-D measurements (Q-Sense E1 system,

Biolin Scientific, Inc., Västra Frölunda, Sweden). QCM-D was used to measure the in-situ interaction with a solution flow rate of 0.1 ml/min at 22 °C. A single measurement consisted of four steps: (1) baseline the sensor in dry air; (2) baseline sensor in DI water at pH ~ 4.9, allowing chitin film to fully hydrate; (3) exposure to carboxylic acid solution; (4) exposure to DI water with medium pH~ 4.9. For each step, flow continued until the resonance frequency change plateaued, which indicated that the sensor surface had effectively reached equilibrium with the solution. The 1st, 3rd, 5th, 7th, 9th, 11th, and 13th harmonics were measured simultaneously during all QCM-D experiments. Of these harmonics, the 5th harmonic was selected for analyses.

5.4 Results and Discussion

5.4.1 Foaming Ability of CNF Dispersion

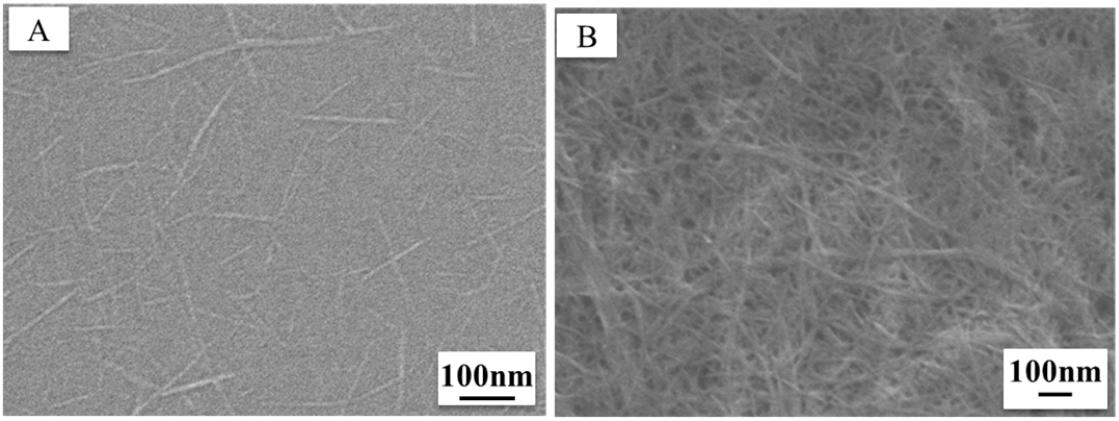

Figure 5.1 SEM images of (A) fibrillated CNFs from the purified chitin and (B) CNF dense film.

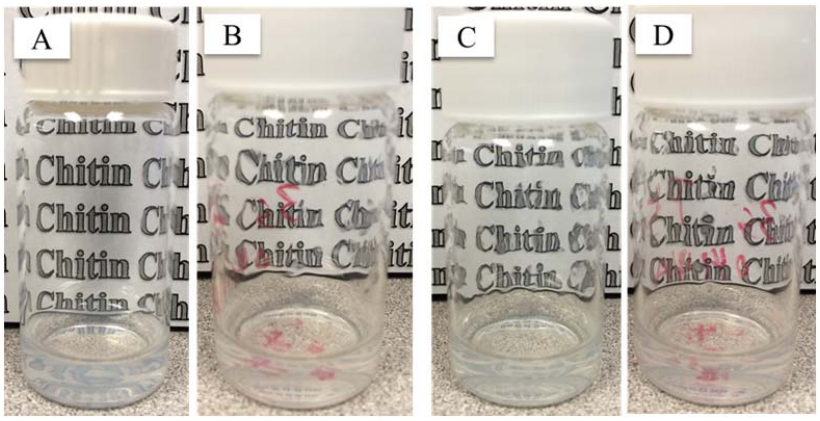

Figure 5.2 (A) and (C) photos represent 1% CNF at pH 4.1 before and after frothing by a rotor-stator homogenizer, respectively; (B) and (D) photos represent 1% CNF at pH 5.8 before and after frothing respectively. (C) and (D) photos were immediately taken after frothing.

Figure 5.1 A shows the morphology of the fibrillated CNFs produced from the purified chitin by a high pressure homogenization process, and the resulting CNFs have diameters of around 20 nm, and lengths ranging from hundreds of nanometers to several micrometers. The CNF dispersion with medium pH of ~ 4.1exhibits high optical transparency and CNF has a zeta potential of more than +50 mv that resulted from the protonated $–NH_3+$ groups. When the dispersion was frothed by a rotor-stator homogenizer, no stable foam was generated (Figure 5.2). Previous study showed that electrostatic repulsion between highly charged particles can induce an adsorption barrier for their attachment at the air/water interface, and when their surface charges were lowered, these particles were able to absorb at the interface and stabilize air bubbles [31, 43]. The surface charge of CNF decreased when increasing medium pH from ~ 4 to ~ 7 and its pKa is around 6.5 [47, 48]. When pH was increased from 4.1 to 5.0 to 5.8 until 7, the CNF dispersion still could not achieve stable foams even using vigorous mechanical frothing (Figure 5.2 C and D). Wetting properties of particles significantly influence their

foaming ability and particles with a contact angle of 90˚ have highest detachment energy from air/water interface according to equation 5.1[18, 27, 28]. The contact angle of CNF is ~57˚, so its detachment energy from the air-water interface should be much greater than thermal energy. However, no stable foams could be produced using solely CNF particles. Since CNF has much higher aspect ratio than that of spherical particle, the equation 5.1 does not fit CNF well and also CNF may show different contact angle at air-water interface in dispersion in comparison to bulk contact angle measurement. The hydrophobicity of CNF at the interface is possibly still not high enough to stabilize air bubbles. Therefore, the foaming ability of CNFs is possibly improved by increasing their hydrophobicity.

5.4.2 Foaming Ability and Foam Stability of CNF/Valeric Acid Dispersion

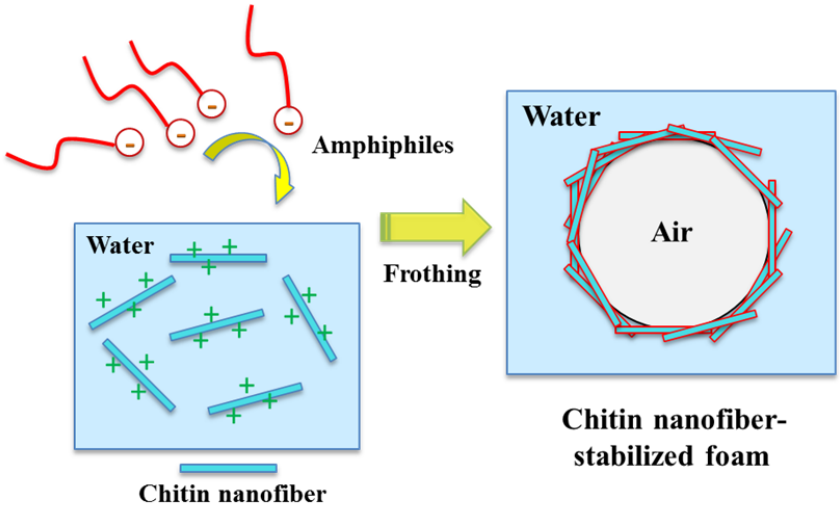

Figure 5.3 Schematic of the formation of CNF stabilized foams.

One approach to hydrophobize CNF is to utilize in-situ physical adsorption of amphiphile on its surface [32-34]. One end of amphiphile has a hydrophobic hydrocarbon tail, and the other end has negative charge under acidic condition, which can interact with

the protonated $-NH_3+$ groups of CNF via electrostatic attraction. Consequently, the hydrophobic tail would be exposed to surrounding aqueous environment, as shown in Figure 5.3. On the basis of this principle, valeric acid should be a great candidate for CNF hydrophobization because it is a short-chain amphiphile that shows negative charge at certain acid condition (pKa: 4.84) and has high critical micelle concentration in water [32, 33].

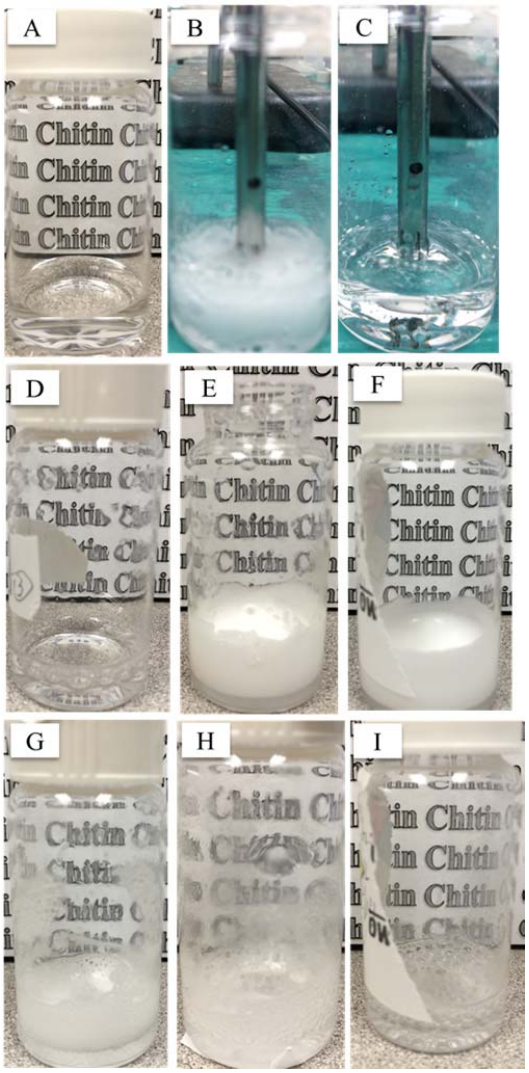

Figure 5.4 (A), (B) and (C) are digital photos of the 50 mmol/l valeric acid in water before, during and after frothing by a rotor-stator homogenizer, respectively; (D),

(E) and (F) are digital photos of the frothed 1 mmol/l, 5 mmol/l and 25 mmol/l valeric acid in 0.1% CNF/water dispersion, respectively (photos were taken 2 mins after frothing); (G) and (H) photos represent 30 mins and 24 hours after the aeration of 5 mmol/l valeric acid/0.1% CNF/water dispersion, respectively; (I) photo was taken 24 hours after the aeration of 25 mmol/l valeric acid/0.1% CNF/water dispersion.

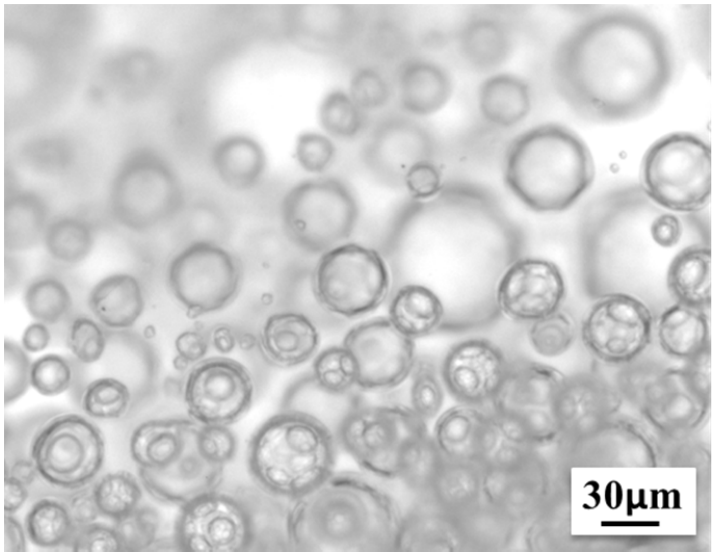

Figure 5.5 Optical microscope image of 5 mmol/l valeric acid/0.1% CNF in water dispersion.

Different amounts of valeric acids were added to the 0.1% CNF dispersion to evaluate the effect of acid concentration on CNF foaming. 1 mmol/l valeric acid addition still could not make bubble stable (Figure 5.4 D). However, stable foams were obtained when the amount of added valeric acids were 5 mmol/l and 25 mmol/l (Figure 5.4 E and F). When aerating different concentrated valeric acid aqueous solutions (1 mmol/l, 5 mmol/l, 25 mmol/l and 50 mmol/l), a plenty of bubbles were generated during frothing, but once frothing was terminated, all the bubbles were gone in a very short time (Figure 5.4 A-C). The stabilized bubble size mainly ranged from 10 µm to 100 µm, as illustrated

in Figure 5.5. SEM images of one droplet of CNF/valeric acid foam showed that there were bubble clusters and single dispersed bubbles in the substrate, as shown in Figure 5.6 A and B.

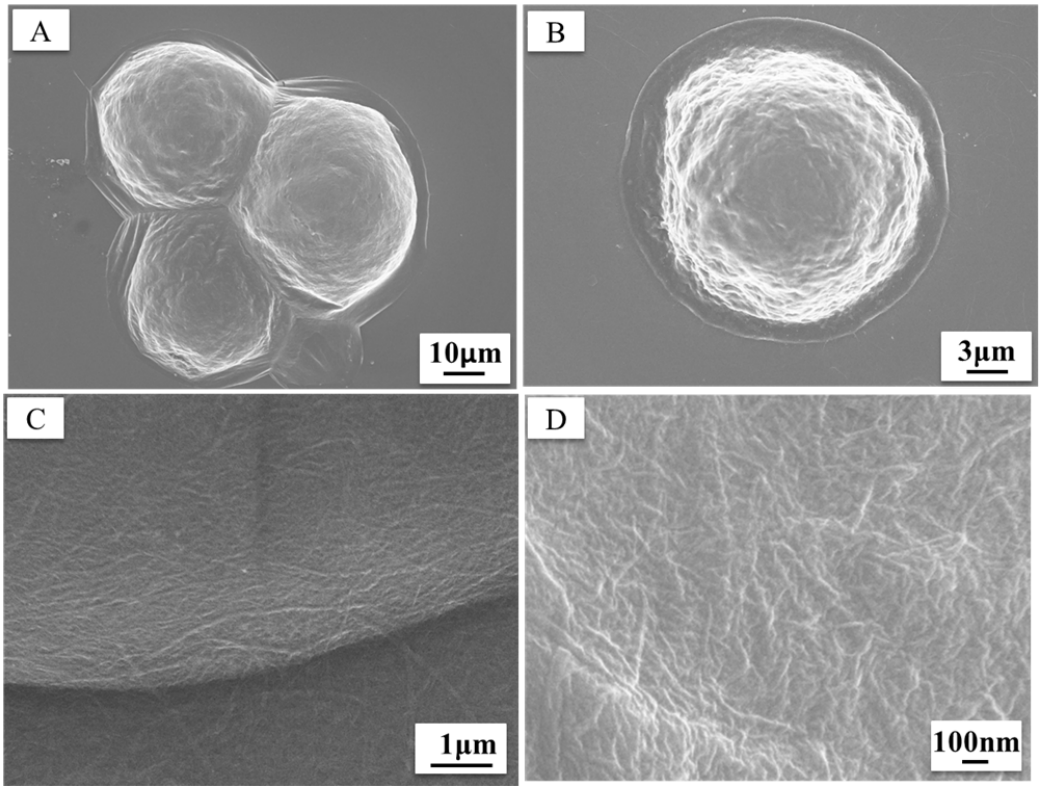

Figure 5.6 SEM images of 0.1% CNF/5 mmol/l valeric acid foams. (A) Top of the bubble cluster; (B) Top of the single dispersed bubble; (C) and (D) are enlarged top SEM images of the bubble edge and bubble center respectively.

When enlarging bubble edge and center regions, Figure 5.6 C and D clearly showed that these bubbles were covered with the intertwined CNF network layers, which indicated that the CNFs were absorbed to the air-water interface. Figure 5.4 G, H and I showed the evolution of these two foams over time at room temperature. Film drainage occurred within 2 minutes after frothing. The bubble size increased markedly 24 hours after frothing.

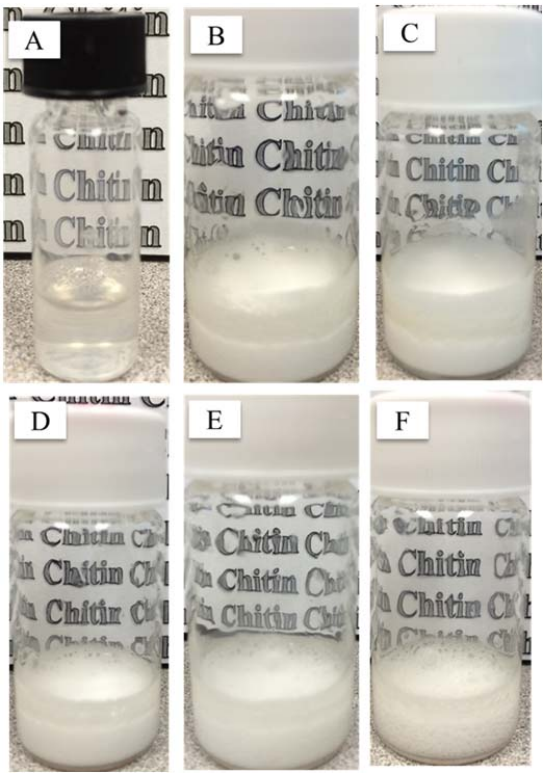

Figure 5.7 (A), (B) and (C) are digital photos of the frothed 1 mmol/l, 5 mmol/l and 25 mmol/l valeric acid in 1% CNF/water dispersion, respectively (photos were taken 2 mins after frothing); (D), (E) and (F) photos represent 1, 3 and 24 hours after the aeration of 5 mmol/l valeric acid/1% CNF/water dispersion, respectively.

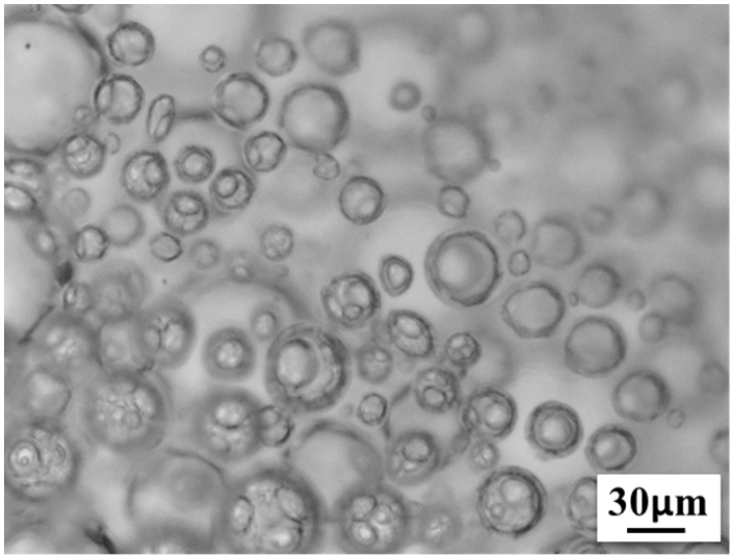

Figure 5.8 Optical microscope image of 5mmol/l valeric acid/1% CNF in water dispersion.

The different amounts of valeric acids were also added to 1% CNF dispersion. The results showed that only acid concentrations of above 5 mmol/l can produce stable aqueous foams, which is similar to 0.1% CNF (Figure 5.7 A-C). However, the foams produced from 1% CNF exhibited much higher foam stability compared with the 0.1% CNF dispersion. As shown in Figure 5.7 D, E and F, no drainage was observed 24 hours after frothing. The rate of bubble size increment was dramatically decreased. Foam stability was quantitatively evaluated by measuring the ratio of frothed foam volume to initial dispersion volume as a function of time. Around 40% air was initially incorporated in the dispersion and the aerated foams then remained a constant volume over 24 hours. Figure 5.8 shows that bubble size mainly ranged from 10µm to 100µm. Bubble clusters and single bubbles were also observed for 1% CNF (Figure 5.9 A-C).

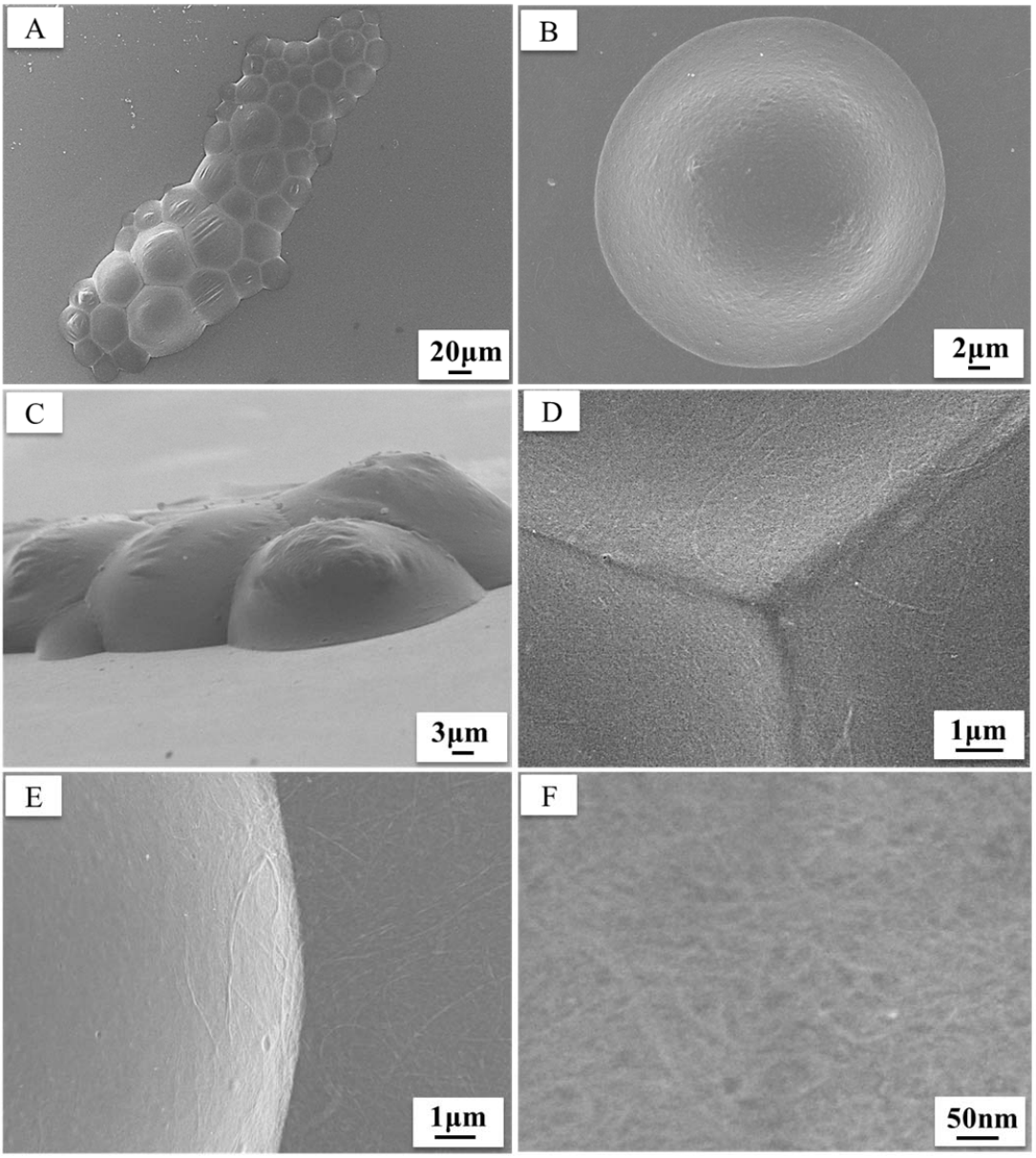

Figure 5.9 SEM images of 1% CNF/5 mmol/l valeric acid foams. (A) Top of bubble cluster; (B) Top of single dispersed bubble; (C) Cross section of bubble cluster; (D), (E) and (F) are the enlarged top SEM images of intersections of three bubbles, bubble edge and bubble center, respectively.

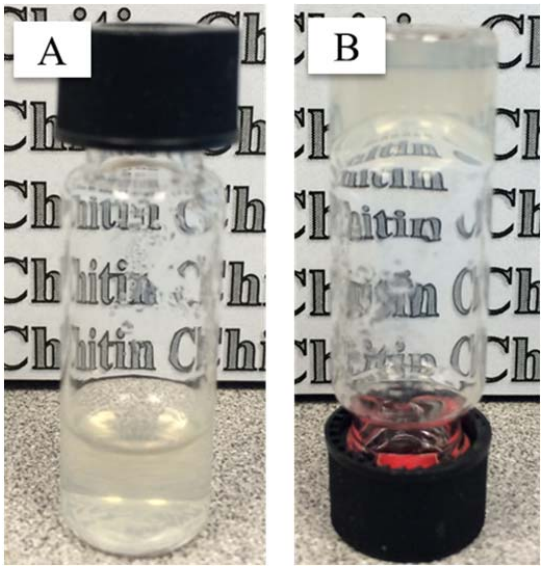

Figure 5.10 (A) and (B) represent the 1% CNF/water dispersion with top-down and upside-down placement, respectively.

SEM images revealed that the CNFs were absorbed at the air-water interface in terms of the layers of CNF formation on the bubble surface (Figure 5.9 D-F). Previously, researchers showed that chitin nanocrystals were easy to form network structures and the gel strength increased with increased particle concentration [55]. The 0.1% CNF dispersion can flow easily under gravity but the 1% CNF showed very strong gelling behavior (Figure 5.10). The high foam stability of 1% CNF dispersion may result from two reasons. One is that the relatively strong CNF networks among bubbles in foam markedly halted or slowed down the film drainage and bubble coalescence, and led to reduced gas diffusion between small and large bubbles, resulting in slow disproportionation [28, 56]. The other possible reason is that the formed CNF layers at the air-water interface for 1% CNF may be much thicker than those of 0.1% CNF so that the resulting foams was more effective to prevent bubble coalescence and disproportionation.

5.4.3 Investigation of the Role of Valeric Acid in CNF Dispersion

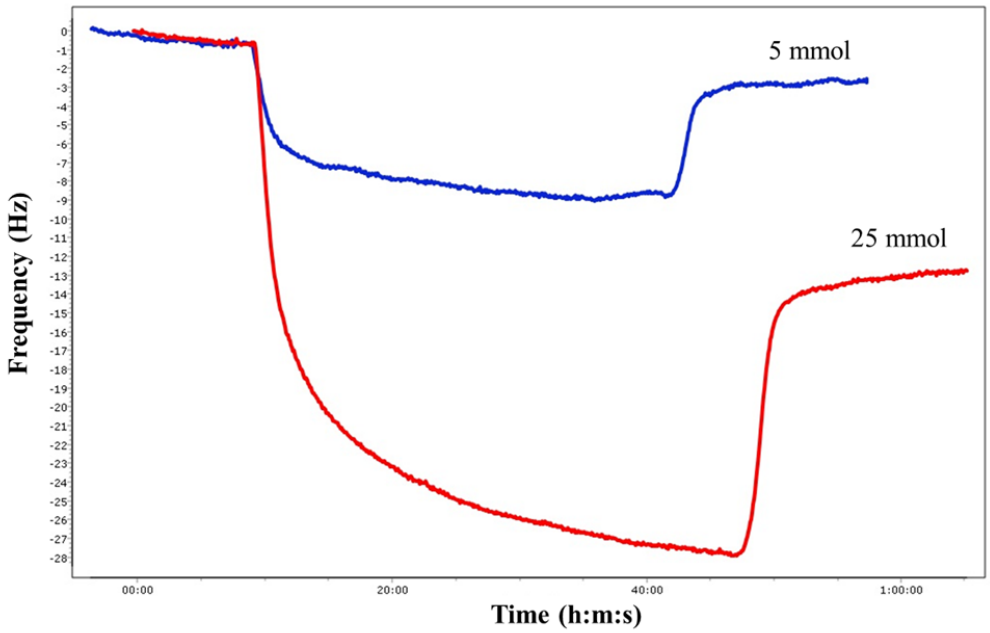

Figure 5.11 Representative curves of fifth overtone QCM shifts in frequency (Hz) as a function of time for valeric acid adsorption on the CNF surface.

We hypothesize that the role of valeric acids in CNF dispersion is to hydrophobize CNF by absorbing on the surface of CNFs via electrostatic attraction and subsequently exposing their hydrophobic tails to water. The adsorption of valeric acids on CNF surface was investigated using QCM-D. Figure 5.11 showed the frequency change of the CNF coated gold sensor as a function of time. After introducing 5 mmol/l valeric acid solution (pH 4.9) into QCM chamber, the frequency was abruptly shifted. The frequency change is an indication of fast mass uptake by the resonators due to the valeric acid absorption. When the frequency reached near-plateau region, water was flowed to remove any excess of loosely bound valeric acids. After rinsing, there were still absorbed valeric acids on the sensor. When injecting 25 mmol/l valeric acids, QCM frequency shift followed the same trend with the lower concentrated one, but more

valeric acids remained on the chitin surface. QCM data demonstrated the adsorption of valeric acids on the CNF surface.

Table 5.1 Surface tensions of valeric acid, CNF and CNF/valeric acid aqueous dispersions.

Sample	Surface Tension (mN/m)	Stable Foam (Yes or No)
DI Water	72.38	No
0.1% CNF/water	72.44	No
0.5% CNF/water	68.41	No
1% CNF/water	68.14	No
1 mmol/l valeric acid	71.7	No
5 mmol/l valeric acid	70.35	No
25 mmol/l valeric acid	63.59	No
50 mmol/l valeric acid	57.18	No
0.1% CNF/0.5 mmol/l valeric acid	71.5	No
0.1% CNF/1 mmol/l valeric acid	71.14	No
0.1% CNF/5 mmol/l valeric acid	70.6	Yes
0.1% CNF/25 mmol/l valeric acid	61.37	Yes
1% CNF/1 mmol/l valeric acid	67.79	No
1% CNF/5 mmol/l valeric acid	56.82	Yes
1% CNF/25 mmol/l valeric acid	55.44	Yes

In addition to SEM images that proved the attachment of CNFs at the air-water interface, the surface tensions of different concentrated valeric acid, CNF and CNF/valeric acid dispersions were also measured to illustrate the adsorption of modified CNFs to the interface. As shown in Table 5.1, valeric acid is able to lower the surface tension, especially for higher concentrated acids (63.59 mN/m for 25 mmol/l and 57.18 mN/m for 50 mmol/l). The higher concentrated CNF (0.5 and 1 wt.%) can slightly reduce

the surface tensions of aqueous dispersion. Interestingly, the surface tension of 1% CNF dispersion was decreased from 68.14 to 56.82 mN/m with addition of relatively small amount of valeric acids (5 mmol/l). It is worth mentioning that a fraction of the added valeric acids would not absorb on the CNF surface, and preferred absorbing at the air-water interface, which contributed to the part of the surface tension reduction. The amount of reduction resulted from free valeric acids and CNFs were not estimated here, but the 5 mmol/l valeric acid or 1% CNF can only slightly decrease the surface tension (70.35 mN/m for 5 mmol/l valeric acid and 68.14 mN/m for 1% CNF). Therefore, the relatively abrupt decrease of the surface tension was mainly attributed to the attachment of the valeric acid treated CNFs to the air-water interface.

5.4.4 Foaming Ability of CNF Dispersion with Addition of Other Carboxylic Acids

Table 5.2 Chemical structures and pKa values of carboxylic acids [35]

Acid	Chemical formula	pKa
Propionic acid	CH_3CH_2COOH	4.86
Valeric acid	$CH_3(CH_2)_3COOH$	4.84
Enanthic acid	$CH_3(CH_2)_5COOH$	4.89
Caprylic acid	$CH_3(CH_2)_6COOH$	4.89

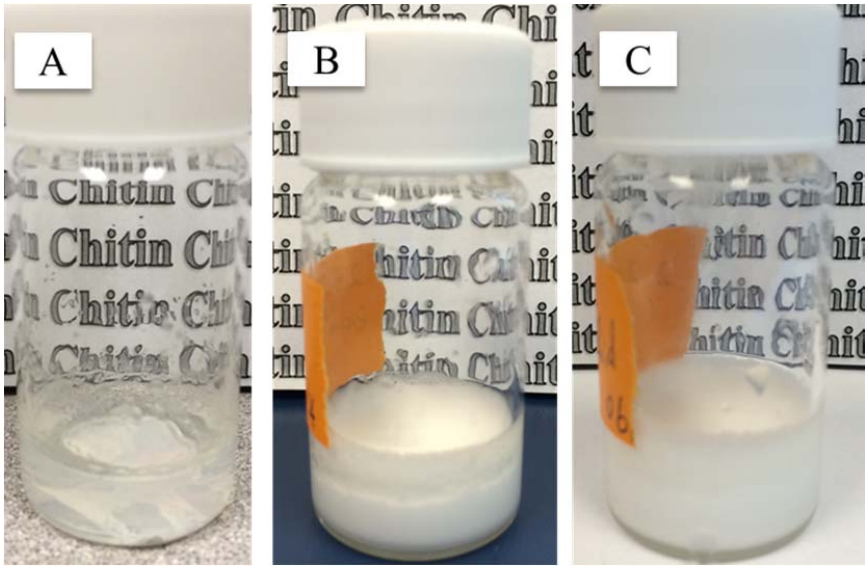

Figure 5.12 (A), (B) and (C) represent the frothed 1% CNF dispersions with addition of propionic acids (25 mmol/l), enanthic acids (0.5 mmol/l) and caprylic acids (0.5 mmol/l), respectively.

In addition to valeric acid, propionic acid, enanthic acid and caprylic acid are also short-chain amphiphiles and possess similar pKa value (Table 2), but have different lengths of hydrocarbon tails. The effect of these three acids on the foaming ability of the CNF dispersion was also investigated. Different amount of propionic acids ranging from 1 mmol/l to 25 mmol/l were added to the CNF dispersion and then the corresponding mixtures were vigorously aerated by a rotor-stator homogenizer, but no stable foams were produced for each condition (Figure 5.12 A). In contrast, the addition of only 0.5 mmol/l enanthic acids or caprylic acids were able to stabilize air bubbles (Figure 5.12 B and C). Previous studies indicated that the carboxylic acids with shorter hydrocarbon tails had higher critical concentration for particle foaming [32, 33, 36]. The propionic acid has very short tail so that its critical concentration for foaming is higher compared to valeric acid, suggesting that over 25 mmol/l propionic acid may enable CNFs to stabilize air

bubbles, whereas enanthic acid and caprylic acid have relatively long hydrocarbon tails and can hydrophobize CNF to the desired value by using small amounts of acids.

5.5 Conclusions

We designed and developed the first aqueous foams stabilized by renewable high-aspect-ratio CNFs. The produced wet foams exhibited excellent stabilization against film drainage, coalescence and disproportionation, which were attributed to the formation of CNF layers at the air-water interface and network structures in the aqueous phase. The fibrillated CNFs did not show foaming ability even though the medium pH was tuned from ~4 to ~7. However, the highly stable aqueous foams can be achieved when CNFs were modified via the physical adsorption of valeric acids on their surface. We found that there was critical concentration of valeric acids for CNF foaming and the concentration of CNF had a great impact on the lifetime of the prepared liquid foams, low concentrated CNF showing poor stability. The valeric acids had strong affinity on the CNF surface and the modified CNFs were able to absorb at the air-water interface and reduce the surface tension of aqueous dispersion. In terms of the excellent inherent properties of chitin, such as renewability, abundance, biodegradable, antibacterial activity and high stiffness, the resulting chitin-based aqueous foams should be attractive for many applications, such as packaging, insulation and biomedical engineering.

Acknowledgement: We are grateful to Dr. Behrens for his generous support in providing access to his equipment for measuring zeta potentials, surface tensions and contact angles. We are thankful to Dr. Sandhage and Ben Deglee for their help with QCM-D measurements.

5.6 References

[1]. Murray, B. S.; Ettelaie, R. Foam Stability: Proteins and Nanoparticles. *Current Opinion in Colloid and Interface Science* **2004**, 9, 314-320.

[2]. Dickinson, E. Food Emulsions and Foams: Stabilization by Particles. *Current Opinion in Colloid and Interface Science* **2010**, 15, 40-49.

[3]. Pei, Z. J; Schmidt, K. A. Ice Cream: Foam Formation and Stabilization-A Review. *Food Reviews International* **2010**, 26, 122-137.

[4]. Binks, B. P.; Murakami, R. Phase Inversion of Particle-stabilized Materials from Foams to Dry Water. *Nature Materials* **2006**, 5, 865-869.

[5]. Farajzadeh, R.; Andrianov, A.; Krastev, R.; Hirasaki, G. J.; Rossen, W. R. Foam–oil Interaction in Porous Media: Implications for Foam assisted Enhanced Oil Recovery. *Advanced in Colloid and Interface Science* **2012**, 183, 1-13.

[6]. Lee, J.; Nikolov, A.; Wasan, D. Stability of Aqueous Foams in the Presence of Oil: On the Importance of Dispersed vs Solubilized Oil. *Industrial and Engineering Chemistry Research* **2013**, 52, 66-72.

[7]. Shibata, J.; Fuerstenau, D. W. Flocculation and Flotation Characteristics of Fine Hematite with Sodium Oleate. *International Journal of Mineral Processing* **2003**, 72, 25-32.

[8]. Clyne, T. W.; Golosnoy, I. O.; Tan, J. C.; Markaki, A. E. Porous Materials for Thermal Management under Extreme Conditions. *Philosophical Transactions of the Royal Society A* **2006**, 364, 125-146.

[9]. Banhart, J. Metal Foams: Production and Stability. *Advanced Engineering Materials* **2006**, 8, 781-794.

[10]. Studart, A.; Nelson, A.; Iwanovsky, B.; Kotyrba, M.; Kündig, A. A.; Dalla Torre, F. H.; Gonzenbach, U. T.; Gauckler, L. J.; Löffler, J. F. Metallic Foams from Nanoparticle-stabilized Wet Foams and Emulsions. *Journal of Materials Chemistry* **2012**, 22, 820-823.

[11]. Dinsmore. A. D.; Hsu, M. F.; Nikolaides, M. G.; Marquez, M.; Bausch. A. R.; Weitz, D. A. Colloidosomes: Selectively Permeable Capsules Composed of Colloidal Particles. *Science* **2002**, 298, 1006-1009.

[12]. Lindner, J. R. Microbubbles in Medical Imaging: Current Applications and Future Directions. *Nature* **2004**, 3, 527-532.

[13]. Mohamedi, G.; Azmin, M.; Pastoriza-Santos, I.; Huang, V.; Pérez-Juste, J.; Liz-Marzán, L.; Edirisinghe, M.; Stride, E. Effects of Gold Nanoparticles on the Stability of Microbubbles. *Langmuir* **2012**, 28, 13808-13815.

[14]. Pugh, R. J. Foaming, Foam Films, Antifoaming and Defoaming. *Advances in Colloid and Interface Science* **1996**, 64, 67-142.

[15]. Binks, B. P. Particles as Surfactants-Similarities and Differences. *Current Opinion in Colloid and Interface Science* **2002**, 7, 21-41.

[16]. Kaptay, G. Interfacial Criteria for Stabilization of Liquid Foams by Solid Particles. *Colloids and Surfaces A: Physicochemical and Engineering Aspects* **2004**, 230, 67-80.

[17]. Saint-Jalmes, A. Physical Chemistry in Foam Drainage and Coarsening. *Soft Matter* **2006**, 2, 836-849.

[18]. Studart, A. R.; Gonzenbach, U. T.; Tervoort, E.; Gauckler, L. J. Processing Routes to Macroporous Ceramics: A Review. *Journal of American Ceramic Society* **2006**, 89, 1771-1789.

[19]. Fameau, A; Saint-Jalmes, A.; Cousin, F.; Houssou, B. H.; Novales, B.; Navailles, L.; Nallet, F.; Gaillard, C.; Boué, F.; Douliez, J. Smart Foams: Switching Reversibly between Ultrastable and Unstable Foams. *Angewandte Chemie International Edition* **2011**, 123, 8414-8419.

[20]. Carl, A.; Klitzing, R. Smart Foams: New Perspectives towards Responsive Composite Materials. *Angewandte Chemie International Edition* **2011**, 50, 11290-11292.

[21]. Du, Z.; Bilbao-Montoya, M. P.; Binks, B. P.; Dickinson, E.; Ettelaie, R.; Murray, B. S. Outstanding Stability of Particle-Stabilized Bubbles. *Langmuir* **2003,** 19, 3106-3108.

[22]. Alargova, R. G.; Warhadpande, D. S.; Paunov, V. N.; Velev, O. D. Foam Superstabilization by Polymer Microrods. *Langmuir* **2004**, 20, 10371-10374.

[23]. Dickinson, E.; Ettelaie, R.; Kostakis, T.; Murray, B. S. Factors Controlling the Formation and Stability of Air Bubbles Stabilized by Partially Hydrophobic Silica Nanoparticles. *Langmuir* **2004**, 20, 8517-8525.

[24]. Binks, B. P.; Horozov, T. S. Aqueous Foams Stabilized Solely by Silica Nanoparticles. *Angewandte Chemie International Edition* **2005**, 44, 3722-3725.

[25]. Subramaniam, A. B.; Abkarian, M.; Mahadevan, L.; Stone, H. A. Mechanics of Interfacial Composite Materials. *Langmuir* **2006**, 22, 10204-10208.

[26]. Abkarian, M.; Subramaniam, A. B.; Kim, S.; Larsen, R. J.; Yang, S; Stone, H. A. Dissolution Arrest and Stability of Particle-Covered Bubbles. *Physical Review Letters* **2007**, 99, 188301.

[27]. Hunter, T. N.; Pugh, R. J.; Franks, G. V.; Jameson, G. J. The Role of Particles in Stabilising Foams and Emulsions. *Advances in Colloid and Interface Science* **2008**, 137, 57–81.

[28]. Horozov, T. S. Foams and Foam Films Stabilised by Solid Particles. *Current Opinion in Colloid and Interface Science* **2008**, 13, 134–140.

[29]. Martinez, A. C.; Rio, E.; Delon, G.; Saint-Jalmes, A.; Langevin, D.; Binks, B. P. On the Origin of the Remarkable Stability of Aqueous Foams Stabilised by Nanoparticles: Link with Microscopic Surface Properties. *Soft Matter* **2008**, 4, 1531-1535.

[30]. Stocco, A.; Drenckhan, W.; Rio, E.; Langevin, D.; Binks, B. P. Particle-stabilised Foams: An Interfacial Study. *Soft Matter* **2009**, 5, 2215-2222.

[31]. Stocco, A.; Rio, E.; Binks, B. P.; Langevin, D. Aqueous Foams Stabilized Solely by Particles. *Soft Matter* **2011**, 7, 1260-1267.

[32]. Gonzenbach, U. T.; Studart, A. R.; Tervoort, E.; Gauckler, L. J. Ultrastable Particle-Stabilized Foams. *Angewandte Chemie International Edition* **2006**, 45, 3526-3530.

[33]. Gonzenbach, U. T.; Studart, A. R.; Tervoort, E.; Gauckler, L. J. Stabilization of Foams with Inorganic Colloidal Particles. *Langmuir* **2006**, *22,* 10983-10988.

[34]. Studart, A. R.; Gonzenbach, U. T.; Akartuna, I.; Tervoort, E.; Gauckler, L. J. Materials from Foams and Emulsions Stabilized by Colloidal Particles. *Journal of Materials Chemistry* **2007**, 17, 3283-3289.

[35]. Gonzenbach, U. T.; Studart, A. R.; Steinlin, D.; Tervoort, E.; Gauckler, L. J. Processing of Particle-Stabilized Wet Foams into Porous Ceramics. *Journal of American Ceramic Society* **2007**, 90, 3407-3414.

[36]. Gonzenbach, U. T.; Studart, A. R.; Tervoort, E.; Gauckler, L. J. Tailoring the Microstructure of Particle-Stabilized Wet Foams. *Langmuir* **2007**, 23, 1025-1032.

[37]. Gonzenbach, U. T.; Studart, A. R.; Tervoort, E.; Gauckler, L. J. Macroporous Ceramics from Particle-stabilized Wet Foams. *Journal of American Ceramic Society* **2007**, 90, 16-22.

[38]. Wong, J. C. H.; Tervoort, E.; Busato, S.; Gonzenbach, U. T.; Studart, A. R.; Ermanni, P.; Gauckler, L. J. Macroporous Polymers from Particle-stabilized Foams. *Journal of Materials Chemistry* **2009**, 19, 5129-5133.

[39]. Zhou, W.; Cao, J.; Liu, W.; Stoyanov, S. How Rigid Rods Self-assemble at Curved Surfaces. *Journal of American Ceramic Society* **2009**, 48, 378-381.

[40]. Wong, J. C. H.; Tervoort, E.; Busato, S.; Gonzenbach, U. T.; Studart, A. R.; Ermanni, P.; Gauckler, L. J. Designing Macroporous Polymers from Particle-stabilized Foams. *Journal of Materials Chemistry* **2010**, 20, 5628-5640.

[41]. Fujii, S.; Mochizuki, M.; Aono, K.; Hamasaki, S.; Murakami, R.; Nakamura, Y. pH-Responsive Aqueous Foams Stabilized by Hairy Latex Particles. *Langmuir* **2011**, 27, 12902-12909.

[42]. Arriaga, L. R.; Drenckhan, W.; Salonen, A.; Rodrigues, J.; Íñiguez-Palomares, R.; Rio, E.; Langevin, D. On the Long-term Stability of Foams Stabilised by Mixtures of Nano-particles and Oppositely Charged Short Chain Surfactants. *Soft Matter* **2012**, 8, 11085-11097.

[43]. Jin, H.; Zhou, W.; Cao, J.; Stoyanov, S. D.; Blijdenstein, T. B. J.; Groot, P. W. N.; Arnaudov, L. N.; Pelan, E. G. Super Stable Foams Stabilized by Colloidal Ethyl Cellulose Particles. *Soft Matter* **2012**, 8, 2194-2205.

[44]. Wong, J. C. H.; Tervoort, E.; Busato, S.; Ermanni, P.; Gauckler, L. J. Engineering Macroporous Composite Materials Using Competitive Adsorption in Particle-stabilized Foams. *Journal of Colloid and Interface Science* **2012**, 383, 1-12.

[45]. Guevara, J. S.; Mejia, A. F.; Shuai, M.; Chang, Y.; Mannan, M. S.; Cheng, Z. Stabilization of Pickering Foams by High-aspect-ratio Nano-sheets. *Soft Matter* **2013**, 9, 1327-1336.

[46]. Fameau, A.; Lam, S.; Velev, O. D. Multi-stimuli Responsive Foams Combining Particles and Self-assembling Fatty Acids. *Chemical Science* **2013**, 4, 3874-3881.

[47]. Rinaudo, M. Chitin and Chitosan: Properties and Applications. *Progress in Polymer Science* **2006**, 31, 603-632.

[48]. Pillai, C. K. S.; Paul, W.; Sharma, C. P. Chitin and Chitosan Polymers: Chemistry, Solubility and Fiber Formation. *Progress in Polymer Science* **2009**, 34, 641-678.

[49]. Nair, K. G.; Dufresne, A. Crab Shell Chitin Whisker Reinforced Natural Rubber Nanocomposites. 1. Processing and Swelling Behavior. *Biomacromolecules* **2003**, 4, 657-665.

[50]. Raabe, D.; Sachs, C.; Romano, P. The Crustacean Exoskeleton as An Example of A Structurally and Mechanically Graded Biological Nanocomposite Material. *Acta Materials* **2005**, 53, 4281-4292.

[51]. Karakashev, S. I.; Ozdemir, O.; Hampton, M. A.; Nguyen, A.V. Formation and Stability of Foams Stabilized by Fine Particles with Similar Size, Contact Angle and Different Shapes. *Colloids and Surfaces A: Physicochemical and Engineering Aspects* **2011**, 382, 132-138.

[52]. Ifuku, S.; Nogi, M.; Abe, K.; Yoshioka, M.; Morimoto, M.; Saimoto, H.; Yano, H. Preparation of Chitin Nanofibers with A Uniform Width as Alpha-chitin from Crab Shells. *Biomacromolecules* **2009**, 10, 1584-1588.

[53]. Liu, X.; Wu, D.; Turgman-Cohen, S.; Genzer, J.; Theyson, T. W.; Rojas, O. J. Adsorption of a Nonionic Symmetric Triblock Copolymer on Surfaces with Different Hydrophobicity. *Langmuir* **2010**, 26, 9565-9574.

[54]. Liu. X.; Vesterinen, A.; Genzer, J.; Seppala, J. V.; Rojas, O. J. Adsorption of PEO-

PPO-PEO Triblock Copolymers with End-Capped Cationic Chains of Poly(2-dimethylaminoethyl methacrylate). *Langmuir* **2011**, 27, 9769-9780.

[55]. Tzoumaki, M. V.; Moschakis, T.; Biliaderis, C. G. Metastability of Nematic Gels Made of Aqueous Chitin Nanocrystal Dispersions. *Biomacromolecules* **2010**, 11, 175-181.

[56]. Martin, A. H.; Grolle, K.; Bos, M. A.; Stuart, M. A. C.; Vliet, T. Network Forming Properties of Various Proteins Adsorbed at the Air/Water Interface in Relation to Foam Stability. *Journal of Colloid and Interface Science* **2002**, 254, 175-183.

CHAPTER 6

CONCLUSIONS AND RECOMMENDATIONS

6.1 Summary and Conclusions

This work achieves the goals set in chapter 1 and makes a significant step forward in the fabrication, characterization, utilization of chitin, and opens up many new research opportunities for its future exploration. The key findings for each specific objective are summarized as follows:

6.1.1 Produce the CNFs without forming strong network structures from crab α-chitin using a physical-mechanical method

We successfully fabricated renewable and biodegradable nanofibers derived from crab α-chitin using a high pressure homogenization technique. This method did not utilize organic solvents. It was determined that the resulting nanofibers have diameters of ~20 nm and were dispersed well in water without forming strong network structures due to their electrostatic repulsions. Compared with the pristine chitin powders, the produced CNFs have a higher residue amount (40% vs. 20%) when heated up to 1000 ˚C The dried nanofiber film exhibits high optical transparency as well as great gas barrier properties. The sustainably-sourced nanofibrous materials can be potentially applied to a variety of fields, including packaging, structural materials, catalysis, electronics and biomedical engineering.

6.1.2 Develop a route to create porous nanofibrous materials utilizing CNFs

We succeeded in producing the porous nanofibrous materials derived solely from CNFs by using a freeze drying method. We showed that versatile porous structures including oriented sheets and three-dimensional aperiodic nanofiber networks can be

achieved by simply tuning freezing rate, where one of the structures mimics the size and interconnectivity of the white *Cyphochilus* beetle cuticle. The formation of such fine nanofibrous structures is not predicted by the widely-used particle encapsulation model in the field of freeze drying. We argue that the formation of the nanofibrous network is attributed to the attractive interactions of the nanofibers and a slow freezing rate. Previously, supercritical drying and organic solvent-based freeze drying have been widely employed to fabricate porous nanofibrous materials. Here, our findings showed that it is possible to obtain such fine structures by more facile water-based freeze drying. The innovative and renewable chitin materials should be useful for a wide range of applications, including reinforcing phase for polymer composites and as a basic template for sensors, tissue scaffolds, catalyst supports, filtration, absorbents and energy storage materials. In addition, the freeze drying method outlined in chapter 3 is likely applicable to other polymer and material classes for producing porous materials with diverse functionalities.

6.1.3 Investigate the reinforcing effect of CNFs in polymer matrices

We demonstrated the reinforcing effects of CNFs in PEO matrix and established the structure-property relationships of the CNF/PEO nanocomposites. We showed that the CNFs formed network structure in matrix and have strong adhesion with PEO, which were characterized by utilizing two relatively new methods for polymer composite field: solvent-leaching of polymer matrix and AFM colloidal probe adhesion. We reason that the strong interactions between CNF and PEO, and CNF network structure formation in matrix can greatly aid the loading stress transfer from matrix to fiber and from fiber to fiber, combined with the CNFs' excellent mechanical properties, eventually resulting in

enhanced mechanical properties of the composites, such as tensile strength and elastic modulus.

6.1.4 Study the interfacial properties of CNFs and create particle-stabilized aqueous foams from renewable high-aspect-ratio CNFs

We successfully developed the first aqueous foams stabilized by renewable high-aspect-ratio CNFs. The created foams exhibited strong hindrance on film drainage, coalescence and disproportionation, which resulted from the formation of CNF layers at the air-water interface as well as network structures in the aqueous phase. The fibrillated CNFs alone were not able to stabilize air bubbles, but highly stable aqueous foams can be achieved when CNFs were modified via the adsorption of valeric acid on their surface. We found that the concentrations of valeric acid and CNFs had a great impact on the formation and lifetime of the wet foams. The results showed that the valeric acid has strong affinity on the CNF surface and the modified CNFs were able to absorb at the air-water interface and reduce the surface tension of aqueous dispersion.

6.2 Recommendations for Future Work

While encouraging works have been done in the development of chitin-based materials, it is worth conducting the following research in the near future to answer many key questions that this thesis has raised but not elucidated.

6.2.1 Investigate the thermal degradation mechanism of chitin-based materials

Interestingly, the produced CNF film has lower onset degradation temperature (204.1 vs. 277.4) and a higher residue amount (40% vs. 20%) compared with the pristine chitin powders when they were pyrolyzed up to 1000 ˚C. The thermal degradation of chitin is quite complicated and includes breaking, splitting of fragments of the main chain or side groups, and release of volatile products [1, 2]. Therefore, the present information

is not enough to fully elaborate the obtained TGA data. To have better understanding of thermal degradation of chitin-based materials, a series of experiments are recommended to perform, such as gas chromatography/mass spectrometry, comprehensive thermal analysis, XPS and NMR characterization.

Furthermore, it is anticipated that the produced chitin-based materials in this thesis are useful precursors in fabricating carbon materials with versatile structures. In terms of chitin's many excellent properties, it is worth exploring the potential applications of the pyrolyzed chitin, such as energy storage and catalysis [3-5].

6.2.2 Verify the proposed porous structure formation mechanism

The formation of finely porous nanofibrous structures is not predicted by the widely-used particle encapsulation model. We proposed that the nanofibrous network structures were created because chitin nanofibers are insoluble and they experience significant attractive interactions, and combined with a slow freezing rate, the network structure remains intact during freezing. Recently, a three-dimensional non-destructive technique, that is, high resolution X-ray absorption radiography and tomography has been demonstrated to be able to in-situ image solidification of the particle/water suspension and the corresponding particle redistribution [6]. Briefly, X-ray radiography enabled visualizing the nucleation and growth of the suspension, and tomography combined information from a large number of X-ray radiographs to generate a three-dimensional map of the solidified suspension. More details can be found from reference 6. This method can be possibly extended to in-situ monitor the freezing process of CNF dispersion, which can help us verify our proposed porous structure formation hypothesis and elucidate the structure evolution of CNFs during dispersion solidification. Meanwhile,

the information can provide us new insights into further tailoring the dimensions of porous chitin and producing porous materials with diverse structures from other material classes based on freeze drying technique.

6.2.3 Investigate the reinforcing effect of CNFs in other polymer matrices

To investigate the reinforcing effect of CNFs in polymer matrices, PEO was chosen as a model polymer in chapter 4. We demonstrated that CNFs are excellent reinforcing fillers for PEO. The tensile strength and elastic modulus of 20% CNF/PEO composites increased ~ 3 times compared to neat polymer. Meanwhile, CNFs formed network structures in matrix and have strong adhesion with PEO. Since PEO is not widely used as structural material, it is recommended to study the reinforcing effect of CNFs in more widely used polymers such as polyurethane and epoxy [7, 8]. The methodology for investigating the role of CNFs in PEO can be extended to these polymers.

6.3 References

[1]. Jazaeri, E.; Tsuzuki, T. Effect of Pyrolysis Conditions on the Properties of Carbonaceous Nanofibers Obtained from Freeze-Dried Cellulose Nanofibers. *Cellulose* **2013**, 20, 707–716.

[2]. Tang, W.; Wang, C.; Chen, D. Kinetic Studies on the Pyrolysis of Chitin and Chitosan. *Polymer Degradation and Stability* **2005**, 389-394.

[3]. La Torre, A.; Gimenez-Lopez, M. d. C.; Fay, M. W.; Rance, G. A.; Solomonsz, W. A.; Chamberlain, T. W.; Brown, P. D.; Khlobystov, A. N. Assembly, Growth, and Catalytic Activity of Gold Nanoparticles in Hollow Carbon Nanofibers. *ACS Nano* **2012**, 6, 2000-2007.

[4]. Chen, L. F.; Zhang, X. D.; Liang, H. W.; Kong, M.; Guan, Q. F.; Chen, P.; Wu, Z. Y.; Yu, S. H. Synthesis of Nitrogen-Doped Porous Carbon Nanofibers as an Efficient Electrode Material for Supercapacitors. *ACS Nano* **2012**, 6, 7092-7102.

[5]. Qie, L.; Chen, W. M.; Wang, Z. H.; Shao, Q. G.; Li, X.; Yuan, L. X.; Hu, X. L.; Zhang, W. X.; Huang, Y. H. Nitrogen-Doped Porous Carbon Nanofiber Webs as Anodes

for Lithium Ion Batteries with a Superhigh Capacity and Rate Capability. *Advanced Materials* **2012**, 24, 2047-2050.

[6] Deville, S.; Maire, E.; Bernard-Granger, G.; Lasalle, A.; Bogner, A.; Gauthier, C.; Leloup, J.; Guizard, C. Metastable and Unstable Cellular Solidification of Colloidal Suspensions. *Nature Materials* **2009**, 8, 966-972.

[7] Khudyakov, I. V.; Zopf, R. D.; Turro, N. J. Polyurethane Nanocomposites. *Designed Monomers and Polymers* **2009**, 12, 279-290.

[8] Xu, S.; Girouard, N.; Schueneman, G.; Shofner, M. L.; Meredith, J. C. Mechanical and Thermal Properties of Waterborne Epoxy Composites Containing Cellulose Nanocrystals. *Polymer* **2013**, 54, 6589-6598.